

Search for gauge-mediated supersymmetry in events with photons and a Z boson decaying to charged leptons at CMS

von

Sebastian Wuchterl

Masterarbeit in Physik

vorgelegt der

Fakultät für Mathematik, Informatik und Naturwissenschaften der
RWTH Aachen

im

November 2018

angefertigt im

I. Physikalischen Institut B

bei

Gutachter: Prof. Dr. Lutz Feld

Zweitgutachter: Prof. Dr. Thomas Hebbeker

1. Introduction	5
1.1. System of units	5
1.2. The standard model of particle physics	5
1.2.1. Indications for physics beyond the standard model	8
1.3. Supersymmetry	9
1.3.1. General Gauge Mediation	12
1.3.2. Signal scenarios	12
1.3.3. Status of SUSY searches at the Large Hadron Collider	15
2. The Experiment	19
2.1. The Large Hadron Collider	19
2.2. The Compact Muon Solenoid	21
2.2.1. Tracker system	23
2.2.2. Electromagnetic calorimeter	23
2.2.3. Hadronic calorimeter	25
2.2.4. The solenoid	25
2.2.5. Muon system	25
2.2.6. Trigger system	26
3. Simulation, data processing, and event reconstruction	29
3.1. Data sets	30
3.2. Simulation	30
3.3. Event and particle reconstruction and identification	34
3.3.1. Particle flow	34
3.3.2. Primary vertex	35
3.3.3. Muons	35

3.3.4. Electrons	36
3.3.5. Photons	37
3.3.6. Jets	38
3.3.7. Missing transverse momentum	39
3.4. Definition of observables	39
3.5. Lepton pair selection and quality requirements	40
3.6. Used triggers and trigger efficiency measurement	41
3.6.1. Trigger efficiency measurement	41
4. Analysis strategy and background estimation	45
4.1. Event Selection	46
4.1.1. Preselection	46
4.1.2. Signal region	46
4.1.3. Control regions	47
4.2. Background estimation	50
4.2.1. Top pair production in association with a photon	53
4.2.2. Drell-Yan and $Z\gamma$ diboson production	55
4.2.3. WZ diboson production	57
4.2.4. ZZ diboson production	60
4.2.5. Other standard model backgrounds	62
4.2.6. Validation of the background estimation	65
4.2.7. Signal contamination	65
4.3. Study of systematic uncertainties	67
4.3.1. Background uncertainties	67
4.3.2. Signal uncertainties	69
5. Results and interpretation	71
5.1. Results	71
5.1.1. Event yields	73
5.2. Statistical interpretation	73
5.2.1. Limit calculation	73
5.2.2. Exclusion limits	75
6. Conclusion	79
Bibliography	81
A. Used simulated data sets	93
B. Used trigger paths	97

Contents		
1.1.	System of units	5
1.2.	The standard model of particle physics	5
1.3.	Supersymmetry	9

Hier kommt ein Intro hin.

1.1. System of units

For simplicity, the unit system commonly used in particle physics is the natural unit system [1]. In natural units, the reduced Planck constant \hbar and the speed of light c are set to unity:

$$\hbar = c = 1 \tag{1.1}$$

The observables used most frequently in particle physics are the energy, momentum, and mass. They are given in magnitudes of eV in the natural unit system. For other variables, such as length and time, the metric unit system is used. Cross sections are given in barn ($1\text{ b} = 10^{-28}\text{ m}^2$). Integrated luminosities are therefore given in b^{-1} . Electric charges are given in dependence of the elementary charge e .

1.2. The standard model of particle physics

The standard model of particle physics (SM) is a gauge theory describing three of the four fundamental forces, namely the electromagnetic, weak, and strong interactions [2]. The gravitational force is described by general relativity [3], which is not described in a quantum field theory as the other three forces.

All fundamental particles can be divided into two sub classes: Particles of integer spin, called bosons, and particles of half-integer spin, called fermions.

The matter content is given by the fermions. Fermions are divided into two subgroups, called quarks and leptons. Leptons take part only in electroweak interactions, while quarks carry also a color charge and therefore interact via the strong force. There are three generations of fermions, which include each two leptons and two quark flavors. The quark flavors are namely the down, up, strange, charm, bottom, and top quarks, while the lepton flavors are made up of three electrically charged particles, the electron (e), the muon (μ), and the tau lepton (τ), as well as three electrically neutral leptons, called neutrinos (ν_e, ν_μ, ν_τ). The latter are assigned the names of the charged leptons of the same generation. Of the quarks, there are up-type quarks carrying an electric charge of $+\frac{2}{3}e$, and down-type quarks carrying an electric charge of $-\frac{1}{3}e$.

The SM is based on the symmetry group $SU(3) \otimes SU(2) \otimes U(1)$. Interactions are described via the exchange of spin-1 gauge bosons. In case of the strong force these are 8 massless gluons, which couple to the color charge. The mediator of the electromagnetic interaction is the massless photon, coupling to the electric charge of particles. For the weak interaction the responsible mediator particles are the three massive bosons W^\pm and Z , which couple to the weak isospin.

An illustration of the complete SM particle content with its properties is shown in Figure 1.1. For each particle, a corresponding antiparticle exists with same mass and inversed quantum numbers. Throughout this thesis particles and antiparticles are treated the same way, and both will be labeled with the name of the particle.

The strong interaction between color charged particles is described by the quantum field theory of quantum chromodynamics (QCD). The corresponding mediators of the non-abelian gauge group $SU(3)_C$ are the eight gluons, which each carry the color-charge C of an anti-color and a color, giving rise to the self coupling of gluons. Due to the confinement of quarks [5], quark-antiquark pairs will be produced out of the vacuum, if particles with color charge are being separated, since the potential energy density of the strong force includes constant terms, and the potential energy rises with increasing distance. This principle is responsible for the existence of only color-neutral bound states of two (mesons), three (baryons) quarks, or five (pentaquarks [6]), called hadrons.

Based on the same principle, color charged particles are not observed as single particles. In the hadronization process, gluons and quarks, which are not allowed to exist freely, lead to the generation of large aggregations of color charged particles while transversing the detector material. These clusters are called jets.

The electromagnetic and weak forces can be unified in the electroweak theory to obtain the electroweak interaction [7–10], represented by the gauge group $SU(2)_L \otimes U(1)_Y$. The indices L and Y indicate, that the weak isospin T couples only to left-handed $SU(2)_L$ doublets of fermions, while the right-handed $SU(2)_L$ singlets carry no isospin, and Y is the hypercharge. The three mediators of the $SU(2)_L$ group are the W^1, W^2 , and W^3 bosons, and the gauge boson of the $U(1)_Y$ group is the B^0 boson. These four bosons mix to the observed W^\pm and Z bosons and

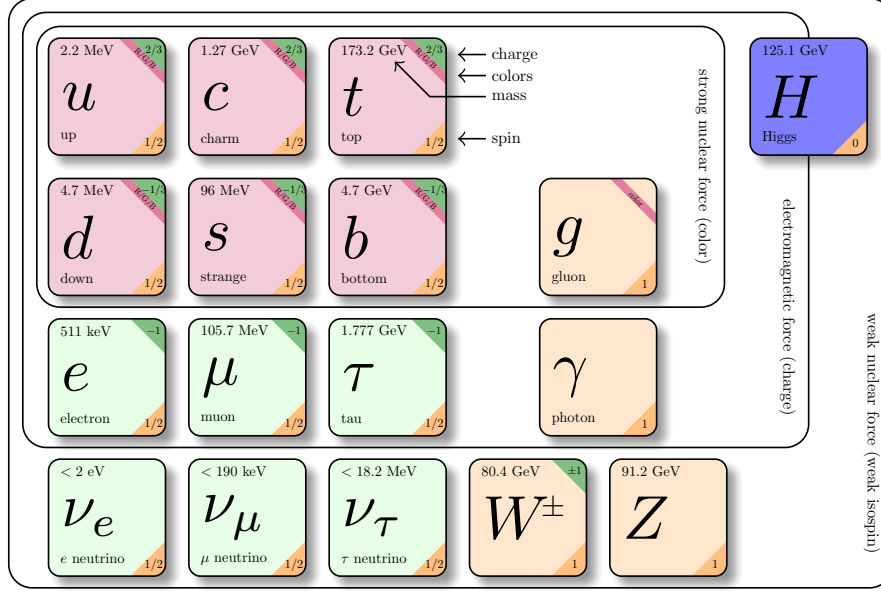


Figure 1.1.: Complete particle content of the standard model. For each particle important properties such as mass, spin, and charges are given. The values are taken from [4].

the photon γ :

$$\begin{pmatrix} \gamma \\ Z \end{pmatrix} = \begin{pmatrix} \cos(\theta_W) & \sin(\theta_W) \\ -\sin(\theta_W) & \cos(\theta_W) \end{pmatrix} \cdot \begin{pmatrix} B \\ W^3 \end{pmatrix}, \quad (1.2)$$

$$W^\pm = \frac{1}{\sqrt{2}} (W^1 \mp iW^2), \quad (1.3)$$

where $\theta_W = \theta_{\text{Weinberg}} \approx 0.231$ [4] is the weak-mixing angle. The resulting weak interaction is maximal parity violating [11, 12]. The W^\pm bosons only couple to left-handed fermions, while the neutral Z boson couples to both left-handed and right-handed particles, but with different strength.

In this theory the gauge bosons are not allowed to have dirac mass terms in the Lagrangian since it would break local gauge symmetries. However, since the Z boson mass is measured to be 91.2 GeV [4] and the W boson mass to be 80.4 GeV [4], the Higgs mechanism is introduced [13–15]. In its simplest representation, it predicts a complex scalar Higgs doublet with a potential, that is symmetric, but has a non zero vacuum expectation value. Therefore it is responsible for the spontaneous symmetry breaking of the $SU(2)_L \otimes U(1)_Y$ gauge group. The Higgs field can be represented by the complex scalar $SU(2)_L$ doublet

$$\Phi = \begin{pmatrix} \Phi^+ \\ \Phi^0 \end{pmatrix} = \frac{1}{\sqrt{2}} \begin{pmatrix} \Phi_1 + i\Phi_2 \\ \Phi_3 + i\Phi_4 \end{pmatrix} \quad (1.4)$$

with the potential

$$V(\Phi) = \mu^2 \Phi^\dagger \Phi + \lambda (\Phi^\dagger \Phi)^2. \quad (1.5)$$

For $\mu^2 < 0$ it results in the non-zero vacuum expectation value of

$$v = \frac{|\mu|}{\sqrt{\lambda}}. \quad (1.6)$$

The field can be rewritten without loss of generality by expanding around the vacuum expectation value and moving to a unitary gauge as

$$\Phi = \frac{1}{\sqrt{2}} \begin{pmatrix} 0 \\ v + h \end{pmatrix}, \quad (1.7)$$

where h is a scalar field. Thereby, three of the four degrees of freedom of the field are consumed to give mass terms to the W and Z boson. For the remaining one, a fourth spin-0 boson, the Higgs boson, is postulated. For consistency, leptons acquire also masses in the SM via Yukawa interactions with the Higgs field. Such a spin-0 neutral boson has been observed in proton-proton collisions at the LHC in 2012 [16, 17], and its mass has been determined to be 125.09 ± 0.24 GeV. The Higgs theory is in good agreement with SM predictions [18], and recently also the couplings of Higgs bosons to the top quark [19], and decays of Higgs bosons to bottom quarks and tau leptons have been observed [20, 21], strengthening the presumption, that the found Higgs boson is the postulated SM Higgs boson.

1.2.1. Indications for physics beyond the standard model

Although the SM describes all phenomena observed at high energy particle colliders successfully, different observations and theoretical arguments indicate that there must exist physics beyond the standard model (BSM).

1. Precise measurements of the cosmic microwave background and theoretical interpretations suggest, that only 4.9% of the universe consists of ordinary matter, while the remainder is composed of dark energy and dark matter [22]. The existence of dark matter is also observed in gravitational lensing effects [23], and in rotation curves of spiral galaxies [24]. Inside the SM there exists no particle, that could explain the total amount of dark matter in the universe.
2. It is assumed, that in the early age of the universe there was the same amount of matter and antimatter. But, today we observe the existence of much more matter than antimatter [25, 26]. In order to explain this discrepancy, different conditions, such as \mathcal{CP} -violation and baryon number violation, should be fulfilled [27]. However, there are no known sources of violation effects large enough to give rise to such big differences.
3. In the SM, neutrinos are assumed to be massless particles. But, the observation of neutrino oscillations are only explicable if neutrinos are massive particles [4, 28].
4. The observation of the Higgs boson in 2012 on the one hand marks the great success of the SM, but on the other hand directly leads to a big problem concerning the Higgs

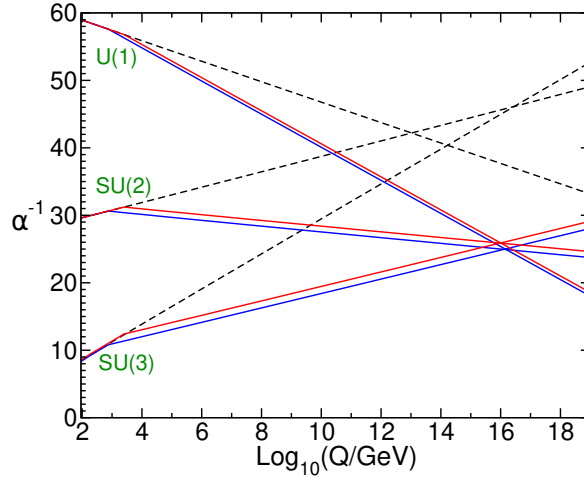


Figure 1.2.: Running couplings for all three fundamental forces in case of the SM (dashed lines) and the MSSM for two different sparticle mass ranges (750 GeV and 2.5 TeV) (solid lines) [29].

mass, which is known as the "Hierarchy Problem". The Higgs boson couples to all massive particles, with coupling strengths proportional to their masses. But unlike for all other particles, the mass term for the Higgs boson is quadratically divergent, caused by virtual loop corrections. The cut-off scale for these corrections can be as large as the validity scale of the SM. Thus, the Higgs boson mass can be pushed to the order of the Planck scale (10^{19} GeV). Since its mass was measured at the LHC to be ≈ 125 GeV, and due to the large difference between the electroweak scale (10^2 GeV) and the Planck scale, these correction terms need to cancel extreme precisely over sixteen orders of magnitude. This is considered "unnatural", leading to the expectation that new physics exists in the energy range between the electroweak and the Planck scales.

5. Driven by the electroweak unification, the unification of all forces in a grand unified theory (GUT) is well motivated. While the couplings of the forces in the SM do not lead to a unification at very high energies [4], a possible extension of the SM with additional new particles could explain such a unification of the electroweak and strong interactions, see Figure 1.2.

1.3. Supersymmetry

Supersymmetry (SUSY) [29, 30] is one of the most popular BSM models and was developed in the 1970s [31, 32]. It is well motivated within theory, because it is the only possible extension of space time symmetry. Since then, many different SUSY models have been established, all based on the same principle: SUSY connects fermions with bosons and the other way around by introducing supersymmetric partners for each SM particle. These superpartners differ only in spin by $\pm 1/2$, all other quantum numbers are kept equal. With the help of generators Q_i , bosonic and fermionic states can be transformed into each

other:

$$Q|fermion\rangle = |boson\rangle, \quad Q|boson\rangle = |fermion\rangle. \quad (1.8)$$

Some of the many advantages of SUSY are, that multiple models directly provide candidates for dark matter particles, and also solve the unification of forces and the Hierarchy Problem without any fine tuning of physical parameters to match the observation.

The simplest model of SUSY is the minimal supersymmetric standard model (MSSM), where only exactly one Q exists. Within the MSSM, for each fermion in the SM exactly two supersymmetric scalar bosons, left and right-handed, are introduced. To differentiate between SM and SUSY particles two, the names of supersymmetric partners are those of the SM particles prepended with an "s-" (standing for scalar). Thus the partners of fermions are called sfermions, and e.g. the partner of the electron is the selectron. The names of superpartners of bosons are constructed by appending the SM name with an "-ino", making them bosinos, so the gluons superpartner for example is called gluino. In general, superpartners are called sparticles, and are labeled the same as their SM counterparts, but with a tilde ($\mu \rightarrow \tilde{\mu}$). Also, all couplings between all sparticles are the same as of their SM partners.

To give masses in the spontaneous symmetry breaking (SSB) to all particles, including both up- and down-type fermions, the SM higgs sector needs to be extended to two complex scalar doublets:

$$H_u = \begin{pmatrix} H_u^+ \\ H_u^0 \end{pmatrix}, \quad H_d = \begin{pmatrix} H_d^0 \\ H_d^- \end{pmatrix}. \quad (1.9)$$

The H_d gives masses to the down-type quarks and charged leptons, while the H_u is responsible for the masses of up-type quarks. Consistently four higgsinos as superpartners are introduced in the MSSM. In the SSB, there are eight degrees of freedom in the Higgs sector instead of four, related to the two Doublets, and giving rise to an expanded Higgs sector consisting of five particles: the two neutral scalars h^0 and H^0 , the two charged scalars H^\pm , and the neutral pseudoscalar A^0 . The remaining three degrees of freedom are used to give masses to the gauge bosons as in the SM. The observed Higgs boson at the LHC can be identified as one of the two neutral scalars, where the lighter h^0 is chosen by convention.

The gauginos and higgsinos mix, similar to the mixing in the electroweak sector, to eight mass eigenstates, which are the four neutral neutralinos $\tilde{\chi}_1^0, \tilde{\chi}_2^0, \tilde{\chi}_3^0, \text{ and } \tilde{\chi}_4^0$, and the four charged charginos $\tilde{\chi}_1^\pm$ and $\tilde{\chi}_2^\pm$.

The total particle content of the MSSM is shown in Figure 1.3. To include gravity, the SM is extended by the graviton G , and the SUSY sector is extended by its superpartner, the gravitino \tilde{G} .

In unbroken SUSY the particles and their corresponding sparticles should have the same masses, and those SUSY particles should have been found easily in the past (considering e.g. an electron/selectron mass of $\approx 511 \text{ keV}$). Therefore, SUSY must be a broken symmetry. There have been many different theories developed over time to explain different breaking scenarios. Attractive approaches are models where gravity is responsible for the SUSY breaking [29], anomaly breaking scenarios [33], and in particular gauge-mediated supersymmetry breaking, which will be discussed in the next section.

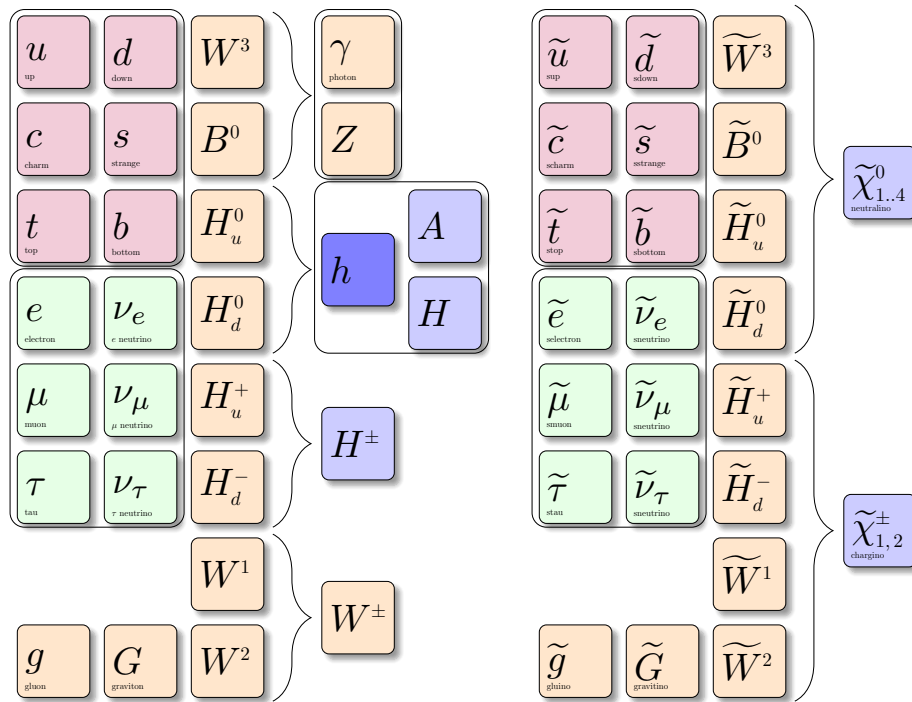


Figure 1.3.: The particle content of the MSSM extended with the graviton and gravitino. Mixings to mass eigenstates are indicated with the brackets.

SUSY can provide Dark Matter candidates, if the lightest supersymmetric particle (LSP), is stable, electrically neutral, and colorless. R-parity

$$R = (-1)^{3B+L+S} \quad (1.10)$$

is therefore introduced as a new conserved quantum number, where S is the spin, B the Baryon number, and L the lepton number. The R-parity is -1 for sparticles, and $+1$ for particles, respectively.

It is not fundamentally necessary, that the LSP is stable. In R-Parity violating scenarios, decays of all SUSY particles into SM particles are allowed. Hence, the conservation of the Baryon number, or the lepton number is violated. R-parity conserving scenarios however are motivated by many precision measurements, such as the life time measurement of protons [34]. In this thesis, only R-parity conserving scenarios are considered. Therefore SUSY particles can only be produced in pairs, and the LSP needs to be stable.

1.3.1. General Gauge Mediation

The phenomenology of SUSY is very rich. While in many models gravity is responsible for SUSY breaking, a different approach, motivating this search, is general gauge mediation (GGM). It is based on the assumption of gauge mediated supersymmetry breaking (GMSB) [35], where an additional "hidden sector" is introduced, that is responsible for the breaking. This sector is mainly decoupled, and the possible interactions between the visible and the hidden sector are only achieved by messenger fields mediated by gauge interactions. In many studied GMSB models, the LSP is the gravitino \tilde{G} . This particle is assumed here to be very light ($\ll 1$ GeV). Therefore, the next-to-lightest supersymmetric particle (NLSP), which basically can be any sparticle, decays promptly. Since the gravitino is stable because of R-parity conservation, electrically and color neutral, it will leave any detector undetected, causing an imbalance in the measured total transverse momentum in proton-proton collisions at the LHC.

In all models considered throughout this thesis, the NLSP is assumed to be the lightest neutralino ($\tilde{\chi}_1^0$). The mixing of the NLSP can include bino, wino, and higgsino components, each enabling different decay channels.

1.3.2. Signal scenarios

The signal scenarios considered in this thesis are discussed in the following. In general, very different production channels for SUSY particles, such as electroweak and strong production, are possible. In case of the LHC proton-proton collisions, SUSY particles can be produced directly in the hard scattering processes of the protons partons, leading to cascade like decay structures down to the decays of the NLSP to the gravitino and a SM boson. The branching fractions of the lightest neutralino to different SM bosons depends on its mixing

$$\tilde{\chi}_1^0 = \sum_{i=1}^N N_{1i} \tilde{\psi}_i^0, \quad (1.11)$$

where $\tilde{\psi}_i^0 = (\tilde{B}, \tilde{W}, \tilde{H}_d^0, \tilde{H}_u^0)$ [36]. The mass eigenstate vectors N_{1i} are defined by four parameters, namely the bino mass M_1 and the wino mass M_2 at the messenger scale, the supersymmetric Higgs mass term μ , and $\tan\beta$, the ratio of the two vacuum expectation values of the up- and down type Higgs bosons. In GGM, a neutralino NLSP has three possible decay branches, all involving the \tilde{G} [36]:

$$\Gamma(\tilde{\chi}_1^0 \rightarrow \tilde{G} + \gamma) = |N_{11}c_W + N_{12}s_W|^2 \mathcal{A} \quad (1.12)$$

$$\Gamma(\tilde{\chi}_1^0 \rightarrow \tilde{G} + Z) = \left(|N_{12}c_W - N_{11}s_W|^2 + \frac{1}{2}|N_{13}c_\beta - N_{14}s_\beta|^2 \right) \left(1 - \frac{m_Z^2}{m_{\tilde{\chi}_1^0}^2} \right)^4 \mathcal{A} \quad (1.13)$$

$$\Gamma(\tilde{\chi}_1^0 \rightarrow \tilde{G} + h) = \frac{1}{2}|N_{13}c_\beta + N_{14}s_\beta|^2 \left(1 - \frac{m_h^2}{m^2} \right)^4 \mathcal{A} \quad (1.14)$$

Here, c_W , s_W , c_β , and s_β are abbreviations for $\cos(\theta_{\text{Weinberg}})$, $\sin(\theta_{\text{Weinberg}})$, $\cos(\beta)$, and $\sin(\beta)$, respectively. The formulae hold in cases of on shell Z and h production. \mathcal{A} is a parameter responsible for the NLSP lifetime [37, 38]:

$$\mathcal{A} = \frac{m_{\tilde{\chi}_1^0}^5}{16\pi F_0^2} \approx \left(\frac{m_{\tilde{\chi}_1^0}}{100 \text{ GeV}} \right)^5 \left(\frac{100 \text{ TeV}}{\sqrt{F_0}} \right)^4 \frac{1}{0.1 \text{ mm}}, \quad (1.15)$$

where F_0 is the scale of SUSY breaking, its range is given by $10 \text{ TeV} \lesssim \sqrt{F_0} \lesssim 10^6 \text{ TeV}$, and it is related to the gravitino mass via $m_{\tilde{G}} = \frac{F_0}{\sqrt{3}M_{\text{Planck}}}$.

Branching fractions for pure bino-, wino- or higgsino-like NLSPs are shown in Figure 1.4. Since the final state investigated in this analysis consists of a Z boson and a photon, the search is sensitive in particular to bino- and wino-like NLSP scenarios.

One scenario used in the development of this search is a full GGM model, where the NLSP is the $\tilde{\chi}_1^0$, and it is assumed to be 100% bino like. The heavier neutralino $\tilde{\chi}_2^0$, and the lightest chargino $\tilde{\chi}_1^\pm$, are assumed to be 100% wino like. Therefore, the bino mass equals the mass of the lightest neutralino, while the $\tilde{\chi}_1^\pm$ and the $\tilde{\chi}_2^0$ are mass degenerate and their mass equals the wino mass. For simplicity reasons higgsinos are decoupled, i.e., set to very high masses. Squarks and gluinos are also decoupled in this scenario, allowing only electroweak production modes. For the most dominant process a diagram is shown in Figure 1.5. The signal cross section depends only on the wino mass, since $\tilde{\chi}_1^0\tilde{\chi}_1^+$ and $\tilde{\chi}_1^+\tilde{\chi}_1^+$ pair production are by far the most dominant production scenarios. The branching fractions of the gauginos are given by the gaugino masses and their gauge eigenstates, and behave as shown in Figure 1.4. The mass of the neutralinos and the lightest chargino directly influence the transverse momenta in the final state. As can be seen in Figure 1.5, larger mass differences between the NLSP mass and the wino mass will lead to higher momenta of the produced bosons in the cascades. The mass of the NLSP is directly responsible for the momenta of the final SM bosons and the gravitino, and therefore directly the missing transverse momentum in an event. A very different approach besides full theoretical models are simplified models (SMS)[39]. Here, only a limited particle content is assumed with simplified assumptions on the mixings and decay channels, providing a more model independent result by probing specifically distinct final states. These results can

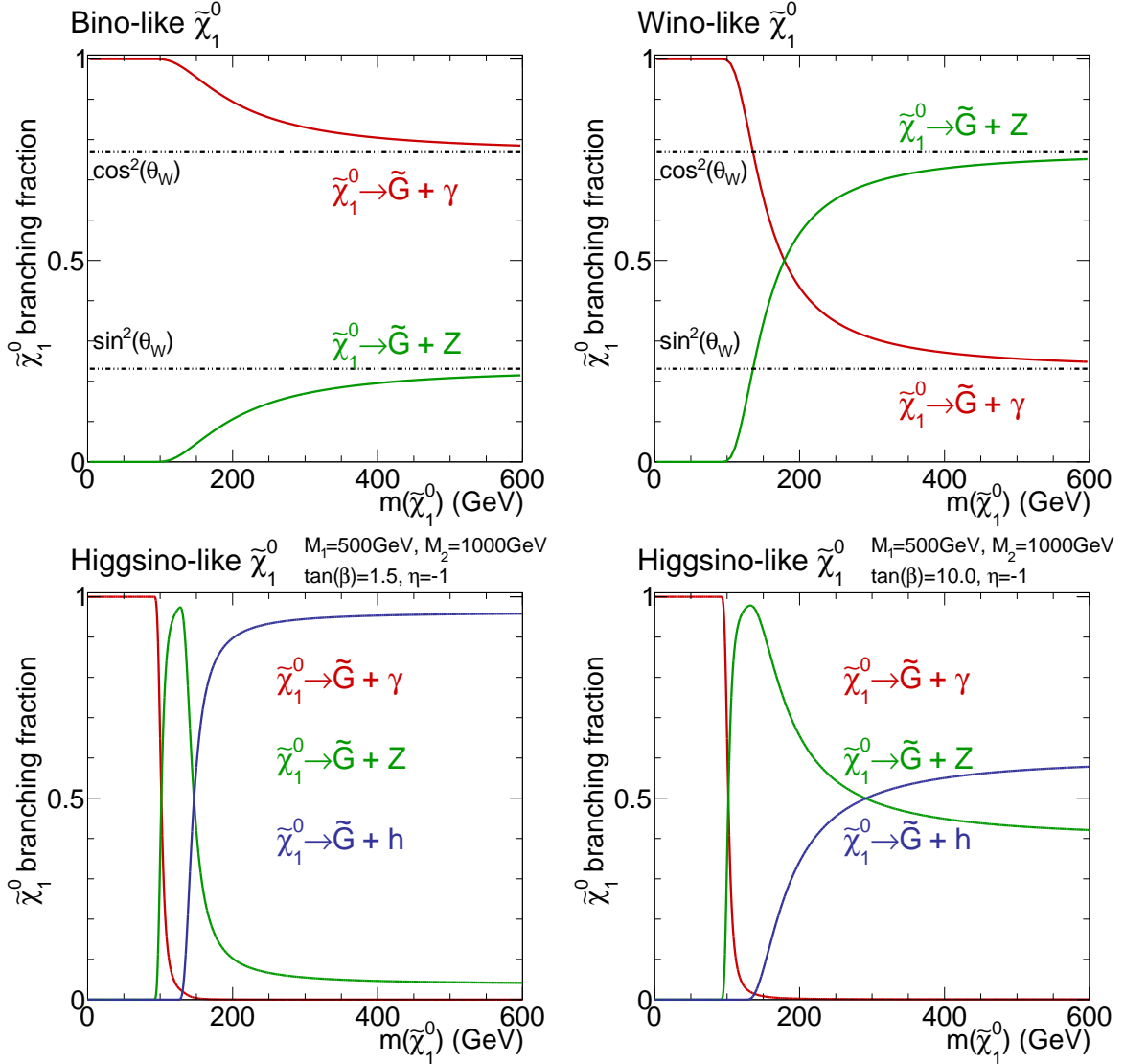


Figure 1.4.: Branching fractions for pure bino (top left), wino (top right), and two higgsino like (bottom) NLPs with different parameters. The parameter η is defined as $\mu = \text{sgn}(\mu)$.

be reinterpreted in various general models [40]. In this thesis two simplified models are considered, one with electroweak production, and the other one with a strong production channel.

The electroweak model is the TChiZG SMS, in which only neutralino-chargino associated and chargino-chargino pair production is assumed. The lightest chargino and lightest neutralino are set to have nearly the same mass, leading to soft emissions of off shell W bosons in the decays of the charginos to the NLSP. The branching fractions of the lightest neutralino to a gravitino and a photon or a Z boson are fixed to 50% each ($\mathcal{BR}(\tilde{\chi}_1^0 \rightarrow \gamma \tilde{G}) = \mathcal{BR}(\tilde{\chi}_1^0 \rightarrow Z \tilde{G}) = 0.5$). A diagram for the process can be found

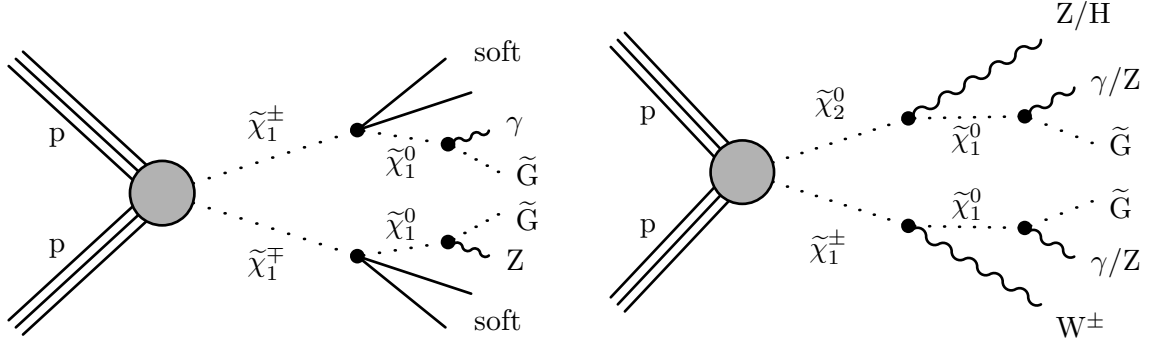


Figure 1.5.: Diagram of the TChiZG scenario with chargino pair production, where the charginos decay to neutralinos under soft emission of off shell W bosons, (left). Also, the chargino-neutralino production is possible. The most dominant production process with a wino-like $\tilde{\chi}_1^+$ and $\tilde{\chi}_2^0$ and a bino-like $\tilde{\chi}_1^0$ of the full GMSB model, (right).

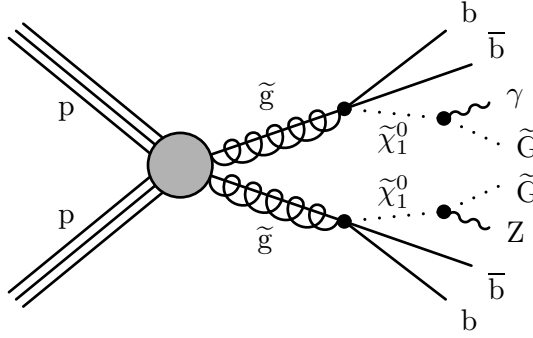


Figure 1.6.: The Feynman diagram for the T5bbbbZG scenario with pair production of gluinos in the hard process, leading to decays to neutralinos under the emission of b quarks.

in Figure 1.5. The squarks and gluinos are decoupled.

The strong model considered here is the T5bbbbZG SMS. A diagram is depicted in Figure 1.6. In this model, gluino pairs are produced in the hard interaction, leading to decays to the NLSP under the emission of pairs of bottom quark pairs. The branching fractions for the $\tilde{\chi}_1^0$ to photons and Z bosons are again set to 50% each.

1.3.3. Status of SUSY searches at the Large Hadron Collider

Searches for SUSY have been performed at the LEP experiment [41], the Tevatron collider [42], and in the LHC RunI data [43]. Although some promising excesses have been observed for example in the opposite-sign dilepton channel [44], no clear evidences for SUSY or other BSM theories have been affirmed. Currently SUSY is also constrained by precision measurements of the Higgs boson properties as mentioned above, and by measurements of rare decay processes, such as the $B_S^0 \rightarrow \mu^- \mu^+$ decay observed by the CMS

and LHCb collaborations [45].

Direct searches for SUSY in terms of SMS interpretations excluded gluino pair production up to gluino masses of around 2 TeV [46], squark pair production up to squark masses of roughly 1500 GeV, and sbottom (stop) masses of approximately 1500 GeV [47] (1200 GeV [48]), respectively. The production of electroweakinos is excluded for chargino/neutralino masses up to around 1.1 TeV [49]. Regarding GMSB scenarios, the currently most stringent exclusion limits obtained by the CMS collaboration [50] are shown in Figure 1.7.

The presented results are based on the proton-proton collision data recorded with the CMS detector in 2016, corresponding to an integrated luminosity of 36 fb^{-1} with a center-of-mass energy of $\sqrt{s} = 13 \text{ TeV}$. Searches similar to the one presented in this thesis exclude electroweakino (electroweak gauge bosino) production scenarios up to roughly 900 GeV, when final states tagged with a high-energy photon and large missing transverse momentum are analyzed [52]. Searches targeting the single lepton plus photon final state [53] have set lower limits. Strong exclusions for gluino and squark pair production scenarios are set by searches targeting events with large hadronic activity and photons [54] and searches investigating events with photons together with high b-jet multiplicity [55]. They set limits up to approximately 2.2 TeV for gluino masses and 1.8 TeV for squark masses. Despite the high exclusion limits set by CMS and ATLAS analyzes [56–58] in comparable ways, large regions of phase space remain unexplored. But since there are many different SUSY models, and the phenomenology of SUSY is very rich, including scenarios with R-parity violation, compressed mass spectra, long-lived particles, and displaced vertices, all described in different breaking scenarios, the search for SUSY stays interesting. Nevertheless, although the sparticle masses are not predicted by theory, natural SUSY scenarios without great fine tuning should lead to sparticle masses in the order of $\mathcal{O}(\text{TeV})$, which are accessible at the LHC [59].

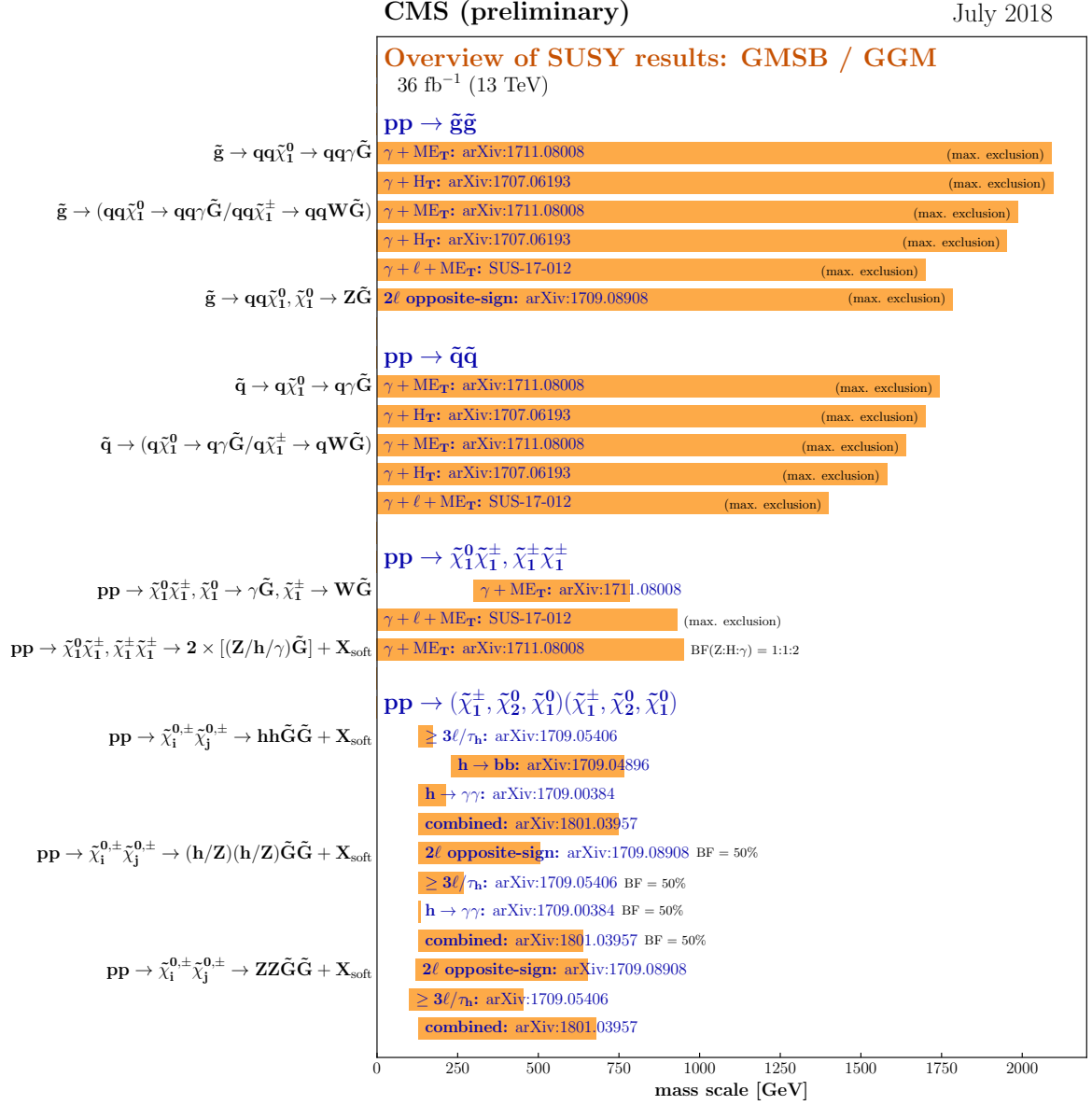


Figure 1.7.: Mass exclusion limits for simplified models in the context of GMSB [51].

Chapter 2

The Experiment

Contents

2.1. The Large Hadron Collider	19
2.2. The Compact Muon Solenoid	21

In this chapter, the relevant experimental setup is discussed. Starting with the description of the Large Hadron Collider (LHC), which is responsible for the acceleration of the proton beams, then the Compact Muon Solenoid (CMS) experiment and detector with all important subdetector components is explained.

2.1. The Large Hadron Collider

The Large Hadron Collider [60, 61], located at the European Organization of Nuclear Research (CERN) near Geneva in Switzerland, is the worlds largest hadron collider. The design center-of-mass energy for proton-proton collisions is $\sqrt{s} = 14$ TeV, while the LHC started operating in 2010 with an energy of 7 TeV. After running also in 2011 at 7 TeV, the energy was increased for the 2012 run period to 8 TeV. After the end of Run I, and after the first long shutdown, the LHC started running again in 2015 with an increased center-of-mass energy of 13 TeV. This setup was maintained trough the whole Run II until the end of 2018. In the following, the LHC will be upgraded again in the long shutdown II, so that with the beginning of 2021 operations with the design energy of 14 TeV are planned. The LHC is also capable of accelerating lead ions with an energy of 2.76 TeV per nucleon.

The LHC is a synchrotron collider built in a tunnel with a circumference of 27 km, which was already used for the Large Electron Positron collider (LEP) [62] in the past. The proton beams are accelerated using various pre-accelerators, such as the Booster, Proton Synchrotron (PS), and the Super Proton Synchrotron (SPS), delivering an proton energy

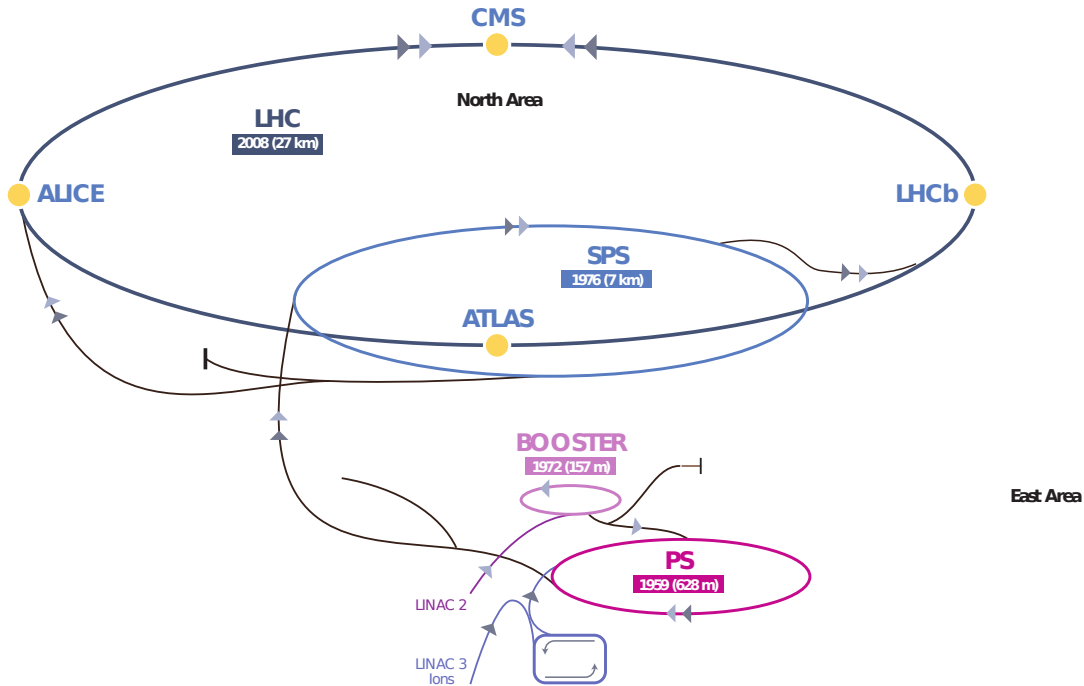


Figure 2.1.: A sketch of the total LHC accelerator complex [66]. The four main experiments are marked as yellow dots, and the preaccelerators are also shown.

of 450 GeV before entering the main storage ring. Four main experiments are located at the LHC, each built around one of the four collisions points. These are: ALICE (A Large Ion Collider Experiment) [63], ATLAS (A Toroidal LHC Apparatus) [64], CMS (Compact Muon Solenoid) [50], and LHCb (LHC Beauty) [65]. CMS and ATLAS were designed to be independent experiments, that are using different technologies, looking both now for BSM physics, measure precisely properties of the SM, and improve the knowledge of the Higgs sector. Besides those tasks, they also analyze lead ion collisions to gain a deeper understanding of the strong interaction. Initially ATLAS and CMS were designed to find the SM Higgs boson. The tasks of ALICE include studies of the quark-gluon-plasma, where the confinement is abrogated, leading to asymptotically free quarks and gluons. LHCb investigates mainly mesons that include charm and bottom quarks, to perform precision measurements of the SM and indirectly look for \mathcal{CP} -violation and hints for new physics. The asymmetric detector design of LHCb favors such studies, since the forward region with particles flying close to the beam axis, is enriched with that kind of events. A schematic sketch of the LHC apparatus including the four big experiment locations and interaction points, and the preaccelerators, is shown in Figure 2.1.

As the protons are accelerated to an energy of 450 GeV, they are injected as bunches of approximately $N = 1.1 \cdot 10^{10}$ particles into the two beam pipes counter rotating in intervals of 25 ns. To achieve a center-of-mass energy of 13 TeV, each beam has to reach an energy of 6.5 TeV. Therefore, superconducting cavities operating at 400 MHz accelerate the protons, and dipole magnets force the beams on their orbital path. Higher order multipoles are needed to focus the beam and correct for different beam and magnetic effects.

One important quantity to characterize a collider is the instantaneous luminosity L , because the rate of any scattering process is proportional to L . It can be defined as

$$L = \frac{N_b^2 n_b f_{rev}}{4\pi\sigma_x\sigma_y} F, \quad (2.1)$$

where N_b is the number of particles per bunch, n_b the number of bunches, f_{rev} the revolution frequency, σ_x and σ_y are the widths of Gaussian distributed beam profiles in x- and y-direction, and F a geometrical factor accounting for the cross section angles of the beams [67]. The integrated Luminosity \mathcal{L}_{int} is related to L via

$$\mathcal{L}_{int} = \int L dt. \quad (2.2)$$

And the number of events N for a given process with cross section σ is given by

$$N = \mathcal{L} \cdot \sigma. \quad (2.3)$$

In 2016 the LHC provided a total integrated luminosity of 40.82 pb^{-1} , while the CMS detector recorded 37.76 pb^{-1} , and 35.92 pb^{-1} were validated as good to be used for physics analysis [68].

2.2. The Compact Muon Solenoid

The data used in this thesis was recorded by the CMS detector [50, 69] in 2016. The CMS detector is a multi-purpose detector housing different subdetector components. From inside to outside these are the tracker system including a pixel and the silicon strip detector, the electromagnetic calorimeter, the hadronic calorimeter, followed by the solenoid and the muon system. A sketch of the openend CMS detector is shown in Figure 2.2. In the following, each subdetector and the trigger system will be briefly explained.

The coordinate system used to describe the detector is originated at the interaction point, and the z-axis points in the direction of the beam axis toward the Jura mountains. The y-axis points upwards, while the x-axis points to the center of the LHC ring. To exploit the underlying symmetry of the detector, a transformation to an angular coordinate system is chosen. The azimuthal angle ϕ is measured in the x-y plane, where $\phi = 0$ equals the direction of the x-axis, and ϕ ranges from $-\pi$ to π . The polar angle θ is measured from the positive z-axis, and the pseudorapidity η can be introduced as

$$\eta = -\ln \left(\tan \left(\frac{\theta}{2} \right) \right). \quad (2.4)$$

The advantage in using η instead of θ is, that differences in η are invariant under Lorentz-boosts along the beam axis, and in the high energy limit the pseudorapidity equals the rapidity.

In proton proton collisions, the initial total momentum of the colliding partons is unknown,

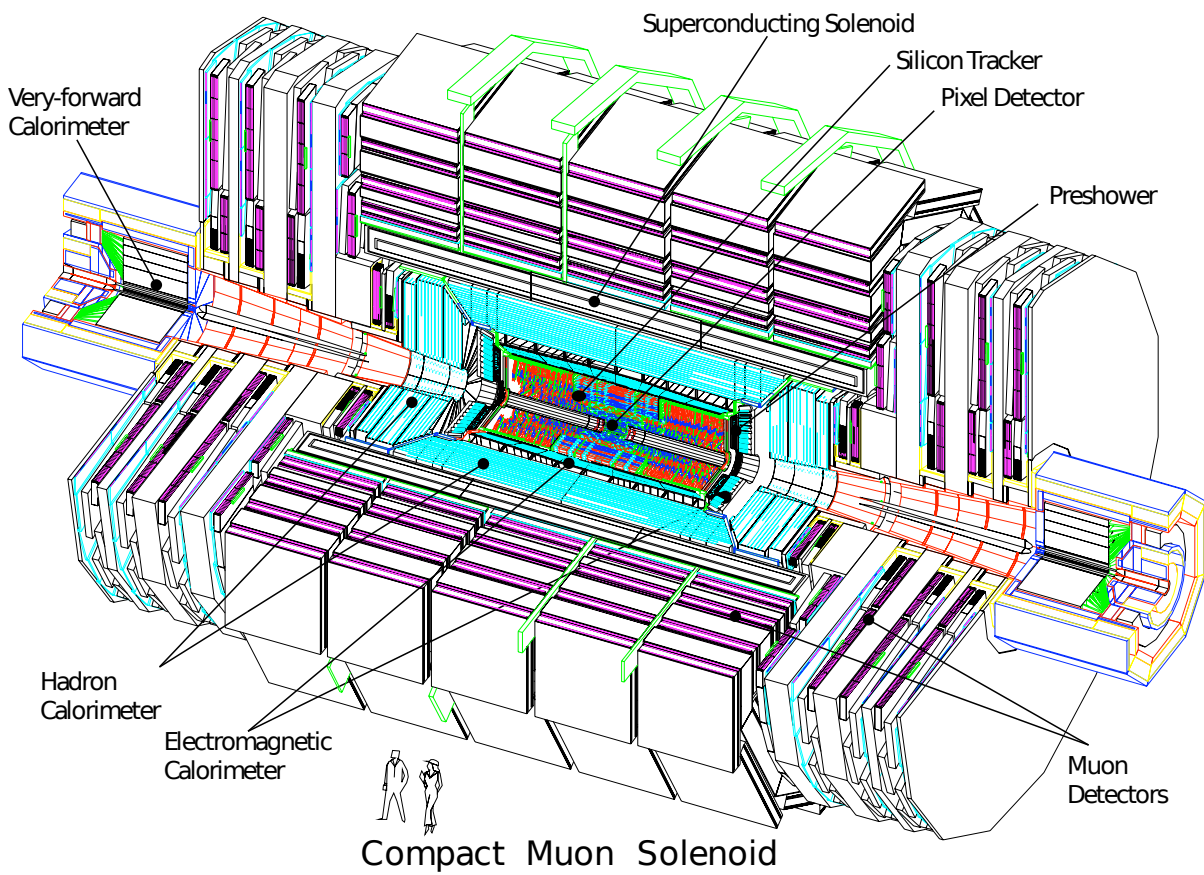


Figure 2.2.: A sketch of the total CMS detector with all subdetectors labeled [69].

since they carry only a fraction of the proton energy. But, the transverse momentum in the initial state is negligible, and therefore, the transverse momentum

$$p_T = |\vec{p}_T| = |\vec{p} \cdot \sin(\theta)| \quad (2.5)$$

is a widely used quantity. Most of the subdetectors are divided in a low η part (barrel), and two high η parts (endcaps). Each of the subdetectors is designed to measure special properties of different particle types, to ensure both a good particle distinction and identification, and precise measurements of energy, momenta, and trajectories.

2.2.1. Tracker system

The most inner part of the CMS detector is the inner tracker, and it consists of two main components, a silicon pixel and a silicon strip detector¹. Both components enclose parts parallel to the beam pipe in the barrel, and parts orthogonal to the beam axis in the endcaps. They cover a length of 5.8 m and a diameter of 2.5 m. A sketch of the total inner tracker divided in all subparts is shown in Figure 2.3. The tracker is designed to perform a precise measurement of particle trajectories and an identification of primary and secondary vertices. Therefore, a high granularity and fast response is needed. The silicon pixel subcomponent is built of three barrel layers (the closest at a radial distance of 4.4 cm to the center of the beam pipe) and two endcap disks, covering a total area size of around 1 m². Each of the ≈ 66 million silicon pixel cells has a size of $100 \times 150 \mu\text{m}^2$. This enables good resolution in all orientations independent of the track direction.

The silicon strip detector consists of four strip layers in the inner (TIB), and six layers in the outer part (TOB). In the direction of the endcaps, it is built of three inner disk layers (TID), and nine layers in the outer part (TEC).

The inner tracker in total covers a range of $|\eta| < 2.5$ and the total sensing system has a size of around 200 m². The performance of the tracker yields a momentum resolution for muons with a transverse momentum of $\approx 100 \text{ GeV}$ of 1 – 2% in the pseudorapidity range of $|\eta| < 1.6$. At higher pseudorapidities the momentum resolution decreases due to a lower granularity.

2.2.2. Electromagnetic calorimeter

Around the tracker, the second subdetector of CMS is the electromagnetic calorimeter (ECAL). Its main purpose is to measure the energy of electrons and photons, which behave very similar in the calorimeter. Only with the combined measurements of the tracker, a differentiation between electrons and photons can be performed. It is made homogeneously of lead-tungstate ($PbWO_4$) crystals, that emit light proportional to the deposited energy of traversing particles in an electromagnetic shower. The emitted light in the visible spectrum is measured by avalanche photomultipliers. The material of lead-tungstate was chosen due to its high density, short Molière radius of 2.2 cm characterizing the shower width, and short radiation length of 0.89 cm. Another big advantage of $PbWO_4$ is the

¹The silicon pixel detector was replaced at the end of the 2016 run. Since in this thesis only 2016 data is used, only the former detector is discussed.

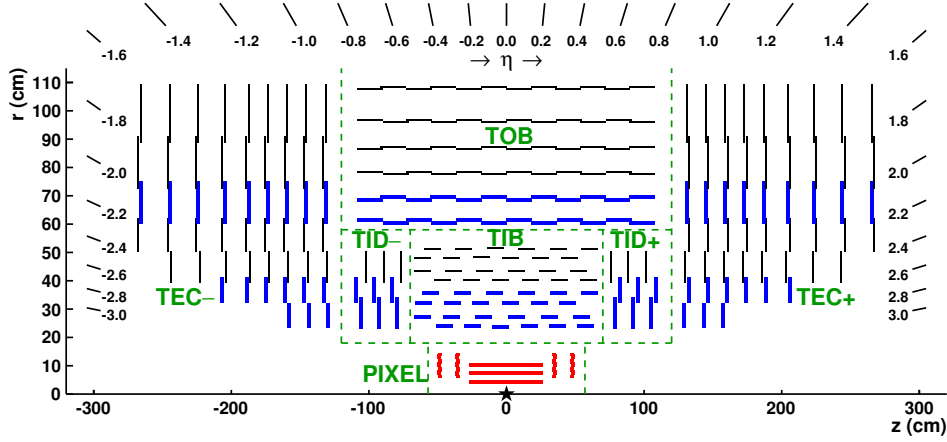


Figure 2.3.: A sketch of one quadrant of the CMS inner tracker [70].

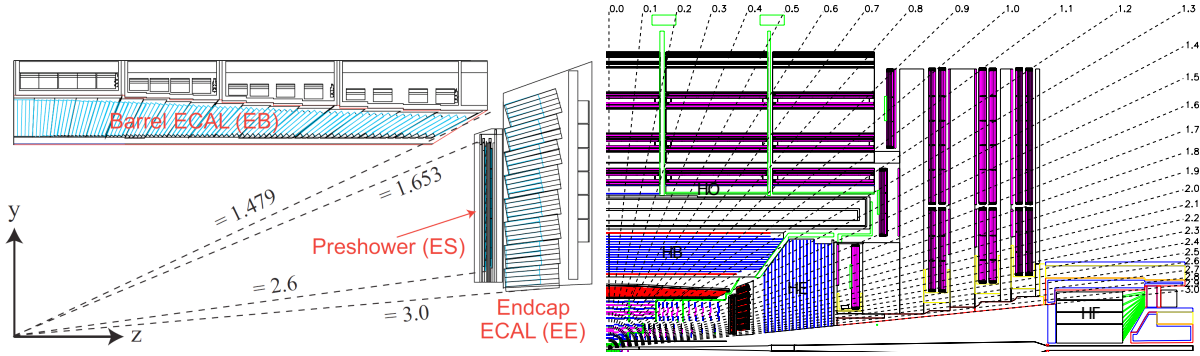


Figure 2.4.: A sketch of one quadrant of the CMS detector for the ECAL (left) [71], and HCAL (right) [50].

short scintillation time. In a time window of 25 ns most of the visible light ($\approx 80\%$) is emitted, thus suiting very well the bunch spacing of 25 ns. The ECAL is divided into a barrel (EB: $|\eta| < 1.479$) and an endcap part (EE: $1.479 < |\eta| < 3.0$), as can be seen in Figure 2.4. The 61200 crystals mounted in the barrel have a length of 23 cm, resulting in 25.8 radiation lengths, and cross section of $22 \times 22 \text{ mm}^2$ matching the Molière radius of $PbWO_4$. In each ECAL endcap, 3662 crystals are placed, having a larger cross section of $28.6 \times 28.6 \text{ mm}^2$ and a length of 22 cm. To prevent particle trajectories to align with the orientation of ECAL crystal borders, the crystals (in EB) are tilted in an angle of 3 degree with respect to their orientation toward the interaction point. In the EE, the tilting varies between 2 – 8 degree in dependence of η . So in total both a compact format and a high granularity could be maintained.

The total energy resolution of the ECAL is determined to be

$$\left(\frac{\sigma_E}{E}\right)^2 = \left(\frac{2.8\%}{\sqrt{E[\text{GeV}]}}\right)^2 + \left(\frac{0.12}{E[\text{GeV}]}\right)^2 + (0.30\%)^2, \quad (2.6)$$

where the first term covers stochastic effects due to the Poissonian distributed number of created scintillation photons, and the second term combines noise effects both from the electronics and multiple collisions per bunch-crossing (pileup). The third term covers constant effects, such as intercalibration effects between the crystals and energy leakage. All the values were obtained in a test beam setup [72]. The energy resolution was designed to be optimal at energies of around ≈ 50 GeV to maximise the sensitivity for the Higgs boson discovery, where photons from the photonic Higgs decay were expected.

An additional preshower detector is installed in front of the ECAL endcap, to identify photons coming from meson decays.

2.2.3. Hadronic calorimeter

The hadronic calorimeter (HCAL), which is designed for the energy measurement of hadrons, consists also of a barrel (HB) and endcap parts (HE). It is placed between the ECAL at a radius of 1.77 m and the magnet coil at a radius of 2.95 m. An additional outer barrel part with lower granularity (HO) extends the HCAL outside of the solenoid, making use of its stopping power, while the hadron forward (HF) is installed to cover high pseudorapidity ranges. The barrel part covers pseudorapidities in the range of $|\eta| < 1.4$, while the HCAL endcap together with the outer HCAL covers the range of $1.3 < |\eta| < 3$. In contrast to the homogeneous ECAL, the HCAL barrel is a so called sampling calorimeter, consisting of alternating layers of brass and plastic scintillating material. The front and backplates are made of steel. Hence, the brass plates stop the incoming particles, and the energy deposit is measured in the form of hadronic showers creating scintillation light in the plastic layers. The outer HCAL makes use of the same principle, but uses in addition the stopping power of the solenoid. The hadron forward, covering pseudorapidity ranges of $3 < |\eta| < 5.2$, needs to be more radiation hard in comparison to the rest of the HCAL, since the energy deposit in the forward region is much higher. It is therefore constructed as a Cherenkov detector made of quartz fibres. A total sketch of the HCAL can be seen in Figure 2.4.

2.2.4. The solenoid

To measure the momentum of the charged particles properly, it is crucial to have bended trajectories. The resolution of the momentum measurement at very high energies is directly proportional to the particles momentum. Thus, for a precise measurement of the curvature of the trajectory, a strong magnetic field is needed. In case of the CMS detector, this is provided by a superconducting NbTi magnet, cooled down to 4.8 K, inducing a magnetic field of 3.8 T. By choosing a solenoid with a length of 12.5 m and a diameter of 6.3 m, the solenoid defines the CMS detector design.

2.2.5. Muon system

The most outside part of the CMS detector is the muon system. Because all other particles besides muons should be stopped in the inner layers, muons are the only particles entering the muon system and leaving a signature there. Three different types of detectors are used to measure and identify muons. The barrel part ($|\eta| < 1.2$) is covered by four stations of

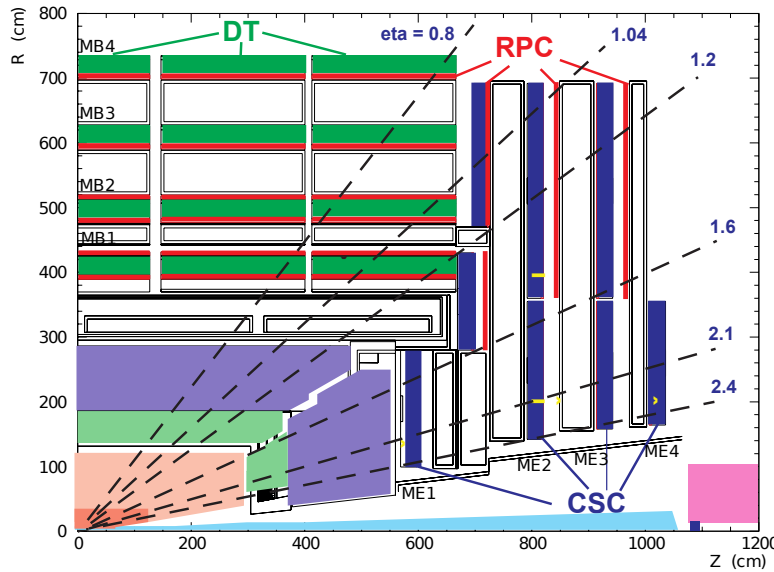


Figure 2.5.: A sketch of one quadrant of the CMS detector is shown with the main detector components [69].

drift tubes (DT). Cathode strip chambers (CSC) are covering the endcap at pseudorapidity $0.9 < |\eta| < 2.4$, because in this region a higher muon rate is expected, and CSCs in contrast to DTs have a faster response time and are more radiation hard. In most of the parts the reconstructed muon efficiency is above 95%, with a misidentification of less than 1%. The muon momentum resolution, dependent on the η region, varies between 1% to 6% for muons with a transverse momentum below 100 GeV, and is of the order of 10% for TeV muons [73]. Again, the energy resolution was designed to be at its maximum at ≈ 50 GeV, where muons from the diboson Z decays of the Higgs boson were expected.

Additional detector components, namely six layers of resistive plate chambers (RPC), are installed in the pseudorapidity range of $|\eta| < 1.8$. Because they show both good time resolution and fast response time, they are mainly used for triggering purposes. The structure of the muon system can be seen in Figure 2.5.

2.2.6. Trigger system

As collisions take place every 25 ns, and therefore at a rate of 40 MHz, it is not achievable to read out and store all events. To keep only physically interesting events and reduce the rate of events to be saved, a trigger system consisting of two stages is implemented [74]. It is composed of the hardware based level 1 triggers (L1), and the software based high level triggers (HLT). Since the L1 trigger needs to deliver decisions in a very short time window, it uses only information provided by the calorimeters and the muon chambers. Usually first requirements on the event, such as a minimal deposited transverse energy, and the presence of first estimates for electron and muon candidates, are imposed. The L1 trigger reduces the event rate to a rate of ≈ 100 kHz.

A more complex decision taking is done by the HLT trigger system. It has full access to

the total readout of all subdetectors, and therefore performs selections close to the offline analysis. It reduces the event rate to $\mathcal{O}(1\text{ kHz})$ [75].

Using the decisions of the HLT, events are categorized into different subsets, based on event kinematics and the trigger objects.

Chapter 3

Simulation, data processing, and event reconstruction

Contents

3.1. Data sets	30
3.2. Simulation	30
3.3. Event and particle reconstruction and identification	34
3.4. Definition of observables	39
3.5. Lepton pair selection and quality requirements	40
3.6. Used triggers and trigger efficiency measurement	41

The data sets, based on the proton-proton (pp) collisions recorded with the CMS detector, are centrally provided in the MINIAOD format [76]. This format contains only parts of the original event and detector information relevant for most of the physics analyses. An analysis looking for deviations from expectations from the SM is supposed not to be biased while development. Thus, SM and signal Monte-Carlo (MC) simulations are performed, and are centrally provided by the CMS collaboration. These are also provided in the MINIAOD format with extended generator information.

All available data sets, including measured data and simulation, are further processed with the help of the CMS software framework (CMSSW¹) [77], the CMS Remote Analysis Builder (CRAB3) [78], and the resources of the Worldwide LHC Computing Grid (WLCG) [79], to obtain files with significantly reduced size. The obtained reduced information is stored in the ROOT [80] file format, and can be used by analysts with self-developed software ².

In this chapter, at first the used data samples are introduced. Thereafter, an overview of MC simulation is given, while the simulated samples used in this analysis are reviewed.

¹Version 8.0.26

²Usually composed of parts developed in C/C++ and Python

After that, the event reconstruction performed on all data sets is explained. A more detailed view is given on the reconstruction and identification of physics objects.

Protons are very complicated objects composed of many different quarks and gluons. The probability to find a distinct parton of a proton with a specific momentum in a deep-inelastic-scattering is given by parton distribution functions (PDFs)[81], that need to be extracted from fits to data, since they are not predicted from QFT. Hence, an event measured with the CMS detector is not clean, but shows different effects. The interaction between the colliding two partons is described in the hard interaction. The products and quantities of these interactions contain the most interesting physical information. But, due to the structure of the proton, many different lower energetic particles can be produced in interactions between additional partons (multi-parton-interactions). These remnants of the scattering process, together with reconstructed remnants of the protons, are denoted as the underlying event. More important for proton-proton colliders, are interactions between protons in the same bunch crossing, that are referred to as pileup.

3.1. Data sets

This analysis uses different data sets based on the pp-collisions of the LHC with a center-of-mass energy of 13 TeV in 2016 and recorded with the CMS detector, corresponding to an integrated luminosity of 35.9 fb^{-1} . Each primary data set (PD) is a composition of events recorded with similar HLT trigger paths. The **DoubleMuon** and **DoubleEG** PDs are used in the central part of the analysis for the signal selection, since they contain events with at least two muons or electrons respectively. **MET** and **HT** PDs are used for trigger efficiency measurements, and the **MuonEG** PD is used to extract a selection relevant for the background prediction. For a list of used triggers see Section 3.6.

The different PDs are separated into several single samples for different run eras throughout 2016. The paths of the used samples, available via the CMS data set bookkeeping service (DBS) [82], with the 03Feb2017 version of reconstruction are listed in Table 3.1.

3.2. Simulation

The simulation process for SM background and SUSY signal samples can be divided in three major steps, which are very similar for both cases. At first, for a specific process events are simulated with an event generator. The event generators used for the generation of the samples considered in this analysis are MADGRAPH 5 in leading order (LO) configuration [83–85], MADGRAPH_MC@NLO in next-to-leading order (NLO) [83, 86], PYTHIA [87] for both cases of accuracy, or POWHEG [88, 89]. Matrix elements for the contributing diagrams are computed, and via convolving with PDFs, cross sections are calculated. These cross sections later can be used to rescale the MC simulation event yield to a given integrated luminosity. Thus, the simulation can be performed with much higher statistics than data in order to minimize the statistical uncertainty of the MC simulation.

Depending on the choice of the chosen generator, a separate generator for the simulation

Table 3.1.: DBS paths for the datasets used in the analysis. Their path is similar, only the PD name varies. The dilepton data sets are used for the key analysis, whereas the H_T and p_T^{miss} datasets are used for the trigger efficiency measurement, see Section 3.6.

PDs	DoubleEG
	DoubleMu
	MuonEG
	HT
	MET
DBS path	/PD/Run2016B-03Feb2017_ver2-v2/MINIAOD
	/PD/Run2016(C-G)-03Feb2017-v1/MINIAOD
	/PD/Run2016H-03Feb2017_ver2-v1/MINIAOD
	/PD/Run2016H-03Feb2017_ver3-v1/MINIAOD

of hadronic showers must be used. This is done with PYTHIA. So that partons generated in matrix element corresponding to the hard interaction, and partons generated with PYTHIA in the showering for e.g. initial state radiation (ISR), are not double counted, a matching with the MLM [84] (LO) or FFX [86] (NLO) matching schemes is performed. The hadronization of the partons (quarks and gluons) is simulated also with PYTHIA, based on the confinement of color charged particles. This, together with the underlying event and pileup, is all covered by the CUETP8M1 generator tune [90]. It is based on 7 TeV proton-proton CMS and proton-antiproton CDF measurements. The PDFs used for the generation of the MC samples are provided by the NNPDF 3.0 sets [91].

The big next step, which is the most time and resource consuming part, is the simulation of the detector response. A full model of the CMS detector was constructed with the GEANT4 [92] package. Hence, it allows a precise simulation of the detector response for the events generated with the procedure described above. In the GEANT4 package, material and particle properties, detector effects, and decay structures are considered in the simulation process. Since this procedure is very time consuming, but leads to a high accuracy, a different method is chosen for signal processes. For the generation of SUSY samples, where theoretical uncertainties dominate and events for many different signal points for each model need to be generated, the CMS FASTSIM packages is used [93]. It is based on a simplified geometry and parametrizations, yielding a reduction in runtime of the factor ≈ 100 . If the "FullSim" and "FastSim" performances are compared [94], a agreement within $\approx 10\%$ for all distributions, such as momentua of particles or jet multiplicity, is observed.

All MC simulated processes used in this analysis are listed in Table 3.2 together with their corresponding cross sections used to rescale the samples later on. The DBS paths are given in the appendix in Table A.1.

The Drell-Yan (DY) Z/γ process, as well as the diboson $Z\gamma$ and $W\gamma$ processes, and tri-boson production of $WW\gamma$ and $WZ\gamma$ are generated with MADGRAPH_MC@NLO in NLO.

Table 3.2.: All SM model simulated samples used in the analysis with their cross sections. For their corresponding accuracy refer to the text. Additional k-factors to obtain NNLO cross sections for the ZZ samples are applied per event in dependence of the p_T of the diboson system. All samples are of the MINIAODSIM format.

process	σ [pb]	process	σ [pb]
ttbar		diboson	
$t\bar{t} \rightarrow \ell^+ \nu b + \ell^- \bar{\nu} \bar{b}$	87.31	$Z\gamma \rightarrow 2\ell\gamma$ ($p_T^\gamma < 130$ GeV)	124.936
ttbarGamma		$Z\gamma \rightarrow 2\ell\gamma$ ($p_T^\gamma > 130$ GeV)	0.1488
$t\bar{t}\gamma \rightarrow 2\ell 2\nu 2b\gamma$	1.679	WZ	4.9125
$t\bar{t}\gamma \rightarrow 4q 2b\gamma$	3.482	$ZZ \rightarrow 2\ell 2\nu$	$0.5644 \cdot k(p_T^{ZZ})$
$t\bar{t}\gamma \rightarrow \ell\nu 2b 2q\gamma$	2.509	$ZZ \rightarrow 2\ell 2\nu$	$0.5644 \cdot k(p_T^{ZZ})$
DrellYan		WW $\rightarrow 2\ell 2\nu$	12.178
$Z/\gamma^* \rightarrow 2\ell$	5765.4	$Wg \rightarrow \ell\nu\gamma$	489
single top		W jets	
$W^+ \rightarrow t\bar{b}$	3.36	$W + jets$	61526.7
$q\bar{b} \rightarrow q'\bar{t}$	80.95	triboson	
$qb \rightarrow q't$	136.02	WW γ	0.2147
$\bar{b} \rightarrow W^+\bar{t}$	11.7	WZ γ	0.04123
$b \rightarrow W^-t$	11.7		

Top pair production in association with a photon ($t\bar{t}\gamma$) and the production of a W boson in association with jets are also simulated using the MADGRAPH_MC@NLO generator in NLO. Top pair production with leptonic decays ($t\bar{t} \rightarrow 2\ell 2\nu 2b$), diboson production of WZ, ZZ, WW, and all singletop production processes are generated using POWHEG. The diboson WW and $W\gamma$ production, the production of $W + jets$, triboson WW γ and WZ γ production, and all singletop production channels are grouped together and denoted as "other" in the following. Next-to-leading order and next-to-next-to-leading order (NNLO) cross sections [95–103] are used for the normalization of the samples.

The generator used for the signal simulation production is MADGRAPH_MC@NLO for the simplified models, and PYTHIA 8 for the full GGM model. The corresponding DBS paths are also listed in the appendix in Table A.2. The cross sections used in the signal normalization are calculated at NLO accuracy for the full GGM scenario, and at NLO+next-to-leading logarithmic (NLL) accuracy for the two simplified models [104–112]. For the electroweak SMS, the applied cross section is calculated for $\tilde{\chi}_1^\pm \tilde{\chi}_1^0$ and $\tilde{\chi}_1^\pm \tilde{\chi}_1^\mp$ production with squarks and gluinos decoupled, and the sum of both is used. In the cross section calculation of gluino pair production for the other SMS, squark decoupling is assumed. The applied cross sections for the GGM scenario are obtained using a full model, thus being different from the ones used for the electroweak SMS.

For the GGM model signal points are generated with wino masses ranging from 215 GeV to 1015 GeV, and bino masses from 205 GeV to $m(\tilde{W}) - 10$ GeV in intervals of 25 GeV. In case of the TChiZG SMS, points are generated with NLSP masses in the range of 300 – 1300 GeV in steps of 25 GeV. The grid of points generated for the T5bbbbZG strong production SMS

includes gluino masses in the range of 800 GeV to 2500 GeV, while the NLSP mass range is scanned from 10 GeV to $m(NLSP) = m(\tilde{g}) - 10$ GeV in non equidistant steps.

As mentioned above, the true number of generated MC events N_{Gen} is very high. Thus, together with the measured integrated luminosity \mathcal{L} , and a given cross section σ , a global event weight of

$$w = \frac{\mathcal{L} \cdot \sigma}{N_{Gen}} \quad (3.1)$$

is used to rescale the simulation to the physical expectation.

Additional event weights are applied on the simulation to account for differences in the pileup distribution. To improve on the MADGRAPH modeling of the multiplicity of additional jets arising from initial state radiation, SUSY SMS MC events are reweighted as a function of N_{Jet}^{ISR} or the transverse momentum of the ISR system, to improve the agreement with observations in data. The latter is based on studies of the transverse momentum of Z events. [113]. The differences to 1 for the reweighting factor is considered as a systematic uncertainty later on. The POWHEG $t\bar{t}$ simulation is also reweighted as a function of the transverse momentum of the top system, based on studies in top pair production cross section measurements [114–117] to improve the agreement of the transverse momentum of the top quark with data.

Overlap removal

Because a very special phase space region is investigated in this analysis, effects play a role, where different physical processes described in higher orders lead to a redundant modeling of distinct diagrams in the matrix element calculation. Different simulated samples are thus needed to achieve a description of the backgrounds with low statistical uncertainty. Since these samples are produced for a distinct process only, e.g. $t\bar{t}$ pair production, NLO contributions in this case overlap with the stand-alone $t\bar{t}\gamma$ samples, because photon radiation in the initial state on the one hand is a NLO contribution for the LO $t\bar{t}$ production, but also on the other hand describes the hard interaction in the $t\bar{t}\gamma$ production. The same holds for the Drell-Yan $Z\gamma^*$ process and the NLO $Z\gamma$ diboson production. To avoid double counting of events, these overlaps need to be removed.

Therefore, the MC simulation for those processes was studied on generator level, to understand which events are exactly produced in both samples. Now that the event properties are identified, the events that have a signature like in samples where photons are produced in the hard interaction, are removed from the nominal samples, to achieve a common higher order description of the selected phase space. Since different generators are used to simulate the different processes, different strategy to remove the overlaps were studied, to ensure that all samples can be added without concerns, and double counting of diagram contributions is rejected.

3.3. Event and particle reconstruction and identification

To maintain both, a precise and robust particle reconstruction, and flexibility in the identification of physical objects, such as electrons or photons, based on the global reconstruction, particle reconstruction and identification is divided in two major parts. This is needed, since very different types of analyses, as searches or SM precision measurements, have very different needs for the requirements of their selected particles in terms of efficiency and misidentification.

In the global event reconstruction, at first, particles and their properties, such as momentum, energy, and trajectory, are reconstructed with the Particle Flow (PF) algorithm [118] by combining information from all CMS subdetectors. After that, identification criteria determined by specialized CMS physics objects groups (POGs) are applied, dependent on the choice of the analyst regarding the demands mentioned above.

In the following the PF algorithm is briefly introduced by explaining its main features, and thereafter more detailed definitions of the physical objects are given.

3.3.1. Particle flow

Traditionally, particles in multi-purpose high energy detectors are identified by their information collected in a certain subdetector component. Electrons for example are identified by measuring the deposited energy in the ECAL, and jets consisting of neutral and charged hadrons and photons are measured independently from the tracker and muon chambers just with the help of the calorimeters. To compensate the only sufficient HCAL performance of the CMS detector, a different method is applied, where all information of all subdetectors are combined and global particle elements are identified. Thus, the excellent performance of the CMS tracking system, the high granularity of the ECAL, and the highly efficient muon tracking system can be exploited. This yields the basis of the particle flow event reconstruction, which showed great performance for the first time in the application in the CMS experiment.

The PF reconstruction and identification procedure is divided in multiple subtasks. At first tracks and clusters are reconstructed separately, and afterwards they are combined by a linking algorithm. In the end, so-called PF blocks are formed out of the links, and final decisions are made on the type of the particle.

A combinatorial track finding algorithm based on Kalman Filtering [119] is used to reconstruct tracks in three stages. At first, seeds are generated that are compatible with a few tracker hits and therefore with a trajectory of a charged particle. Secondly, trajectories are built by using all tracker layers. And finally, the particle properties, such as momentum and direction, are determined in a fit. The tracking procedure is optimized to maintain a high efficiency by keeping a low misidentification rate. Solely achieved with this approach, e.g. a tracking efficiency of 99% for muons, and around 70 – 80% for charged pions is achieved. To further increase the efficiency while retaining the misidentification as low as possible, an iterative tracking procedure is realized, where each step has a lower efficiency, but quality criteria requirements ensure a low misidentification rate.

For electrons another individual track reconstruction is performed. In contrast to the tracker based approach described above, an approach based on reconstructed ECAL clus-

ters is used. Thereby, extrapolations back to the inner tracker are realized based on the cluster energy and position.

The muon tracking is also different, since here in addition the muon system can be used to gain further information and increase the efficiency and lower the misidentification rate. Three types of muon tracks are reconstructed. The first are standalone muon tracks, where only the information of the muon system, in specific seeds built of hits in the DTs and CSCs, are used to reconstruct a muon trajectory through all muon system subcomponents. Global muon tracks are standalone muon tracks, that can be matched to hits in the inner tracker. And finally tracker muon tracks are obtained by extrapolating inner tracker tracks to the muon system, and are only considered if at least one muon segment hit matches the extrapolation.

The aforementioned clustering algorithm is performed in each subcalorimeter separately. It is used to measure the energy and direction of neutral particles such as photons and neutral hadrons, and distinguish between these and charged hadrons, photons originating from electron bremsstrahlung. Via determination of cluster seeds, where the energy deposits are maximal compared to the neighboring cells, thereafter a fit based under the assumption of Gaussian distributed cell entries in topological clusters is realized to obtain the energy and position of each cluster.

The last important part of the PF based reconstruction is the linking procedure, where all gained informations are combined, based on the nature of each particle. Multiple links are then summed up to a particle flow block, in which separately the final decisions are made. After each identification step, the used subdetector informations, such as tracks and clusters, are removed from the PF block.

Muons are identified first, driven by the high reconstruction efficiency and misidentification rate using the muon system. Except of jet remnants entering the muon system, called punch through, muons are the only particles leaving a signature in the muon system.

Electrons and prompt photons are identified next, since they are producing very similar signatures in the ECAL due to electromagnetic showers, and also in the tracker, if photons are converted to electron-positron pairs. Finally neutral and charged hadrons, and non-prompt photons, e.g. originating from meson decays, are identified using the remaining information.

Based on the PF reconstruction, further an analysis specific physical object selection can be performed on top of the PF objects, which will be discussed in the following sections.

3.3.2. Primary vertex

The primary vertex is defined by the vertex with the largest sum of transverse momenta squared determined by vertex reconstruction algorithms [120], and needs to be reconstructed within a distance of 24 cm in z direction, and 2 cm in the x-y-plane.

3.3.3. Muons

Muons are required to have a transverse momentum larger than 15 GeV. And because the muon chambers extend only to a pseudorapidity range of $|\eta| < 2.4$, muons need to be reconstructed within this region. In addition, muons have to pass some quality

requirements suggested by the CMS collaboration, yielding a $\approx 98\%$ efficiency [121].

The muon needs to be reconstructed as a PF muon, and either as a global muon or a tracker muon. If it is reconstructed as a global and a as tracker muon, the segment compatibility, which is a measure for the comparability between the tracker tracks and an extrapolation to the muon system, has to be larger than 0.303. In addition, more than 80% of the inner track layers need to be used in the track fit, the normalized goodness of fit ($\chi^2/ndof$) needs to be less than 3, the match between the standalone muon position and the tracker muon must have $\chi^2 < 12$, and the maximum χ^2 found by a kink finding algorithm, which tries to separate the track into two independent tracks, needs to be smaller than 20. If the muon is reconstructed exclusively as a tracker muon, only the segment compatibility needs to be greater than 0.451, and the other requirements on the track quality are removed.

Besides the identification requirements, conditions on the position of the track relative to the reconstructed primary vertex are imposed. In the transversal direction (d_{xy}), muon tracks need to be closer than 0.05 cm to the vertex, and in the longitudinal direction (d_z), the distance needs to be smaller than 0.1 cm. To quantify the dominance of an object with respect to its surrounding particles in its vicinity, the concept of isolation is introduced. A cone dependent isolation is used, called mini isolation, where the cone size in the $\phi - \eta$ plane is calculated relative to the transverse momentum of the particle as follows:

$$R = \max \left(0.05, \min \left(0.2, \frac{10 \text{ GeV}}{p_T} \right) \right). \quad (3.2)$$

Pileup corrections are also taken into account in the mini isolation calculation. The determined energy deposit in the cone around the muon must not exceed 10% of the transverse momentum of the particle.

Table 3.3.: Identification criteria for muons, spreaded for muons being reconstructed as solely tracker and tracker and global muons.

Variable	Value	
	tracker and global muon	tracker muon
segment compatibility	> 0.303	> 0.451
fraction of valid inner tracker hits	> 0.8	-
normalized χ^2 of global track fit	< 3	-
chi2localposition (track standalone position match)	< 12	-
kink finder	< 20	-
p_T	$> 15 \text{ GeV}$	
η	< 2.4	
miniIsolation	< 0.1	
d_{xy}	$< 0.05 \text{ cm}$	
d_z	$< 0.1 \text{ cm}$	

3.3.4. Electrons

The list of requirements imposed on the electron selection is driven by a symmetric approach between the two lepton selections. The same conditions on the distance to the

Table 3.4.: Identification criteria for electrons given separately for reconstructed electrons in the barrel and endcap.

Variable	Value	
	EB	EE
$\sigma_{i\eta i\eta}$	< 0.00988	< 0.0298
$\Delta\eta_{Seed}$	< 0.00311	< 0.00609
$\Delta\phi_{In}$	< 0.00311	< 0.00609
H/E	< 0.253	0.0878
relative combined PF isolation	< 0.0695	< 0.0821
$ \frac{1}{E} - \frac{1}{p} $	< 0.134	< 0.13
# missing inner hits	≤ 1	≤ 1
Photon conversion veto	true	true
p_T	$> 15 \text{ GeV}$	
η	< 2.4	
miniIsolation	< 0.2	
d_{xy}	$< 0.05 \text{ cm}$	
d_z	$< 0.1 \text{ cm}$	

primary vertex, ($d_{xy} < 0.05$, $d_z < 0.1$), the maximum pseudorapidity ($|\eta| < 2.4$), and transverse momentum ($p_T > 15 \text{ GeV}$) need to be fulfilled. The mini isolation criterion is relaxed to 20%.

The identification requirements determined by the CMS Collaboration [122] separately for electrons reconstructed in the ECAL barrel (EB: $|\eta_{Supercluster}| < 1.479$) and endcap (EE: $|\eta_{Supercluster}| > 1.479$) region are listed in Table 3.4. Here, $\sigma_{i\eta i\eta}$ is a quantity characterizing the width of the electromagnetic shower shape in the ECAL in the η direction. It is calculated as the weighted variance of energy deposits in the full 5x5 pixel ECAL supercluster. Since jets emerging from hadrons have a wider shower in the ECAL than electrons, a differentiation can be achieved. Consistency between the information of the reconstructed track at the vertex, and the supercluster is required, by setting conditions on $\Delta\eta$, $\Delta\phi$, and the supercluster energy E and track momentum p . To further separate electrons from hadrons, more energy should be deposited in the ECAL, rather than in the HCAL (H/E). An isolation requirement based on the PF determined isolation, assures that prompt electrons are separated from electrons coming from e.g. jets. Contributions from photons faking electron signatures are suppressed by imposing a requirement on the number of missing inner hits in the tracker, and an additional veto for photon conversions to electron-positron pairs determined in an χ^2 fit.

3.3.5. Photons

Photons need to have a transverse momentum larger than 20 GeV. Because in the considered SUSY signal scenarios the SUSY particles have typically high masses, central collisions are needed to produce these in the proton-proton interactions. Therefore, the sparticles

decay mainly in rest, and the photons originating from the decays are produced more centrally in comparison to SM processes. Hence, only photons reconstructed in the ECAL barrel are considered ($|\eta| < 1.4442$). Additional identification criteria determined by the CMS Collaboration [123] are listed in Table 3.5. Similar to the requirements on $\sigma_{i\eta i\eta}$ and

Table 3.5.: Identification criteria for photons reconstructed in the ECAL barrel.

Variable	Value
$\sigma_{i\eta i\eta}$	< 0.01031
H/E	< 0.0597
PF charged hadron isolation	< 1.295
PF neutral hadron isolation	$< 10.910 + 0.0148 \cdot p_T + 0.000017 \cdot (p_T)^2$
PF photon isolation	$< 3.630 + 0.0047 \cdot p_T$
η	< 1.4442
p_T	$> 20 \text{ GeV}$
# Pixel Seeds	0

H/E for the electron selection, these conditions in the photon identification ensure the suppression of selecting hadrons faking the photon signature. Additional different isolation criteria lower the amount of selected photons originating from neutral and charged hadrons, and photons coming from light meson decays.

Requirements on the distance in the $\eta - \phi$ plane between the photon and selected lepton candidates ($\Delta R(\gamma, \ell) > 0.3$) significantly reduce contributions from final state radiation (FSR) photons. By requiring that no pixel seed can be assigned to a trajectory between ECAL supercluster and interaction point, a clear differentiation between electrons and photons is achieved.

3.3.6. Jets

Jets, see Section 1.2, are very complicated objects due to the complexity of the hadronization and fragmentation processes. Therefore, a sophisticated clustering algorithm is needed to identify them and measure the energy of jets properly. Jets are clustered with the anti- k_T algorithm [124] included in the FASTJET package [125, 126] with a distance parameter of $R = 0.4$. In the clustering procedure, each PF objects is considered a pseudojet, and these pseudojets are summed up iteratively until a certain breaking conditions is fulfilled. The final jet momentum is defined as the total sum of the momenta of the constituents of the jet. Charged hadrons not emerging from the primary vertex are not considered in the clustering. The jet energy is corrected for effects originating from pileup and the detector response, tuned with the help of different data control selections and simulation [127]. Reconstructed jets need to pass loose identification criteria proposed by CMS Collaboration [128], need to have a transverse momentum larger than 30 GeV, and the pseudorapidity must not exceed $|\eta| = 3$. In addition, jets overlapping with photon and lepton candidates in a cone with radius $R = 0.4$ in the $\eta - \phi$ -plane, are removed from the selection to avoid double counting of objects.

3.3.7. Missing transverse momentum

The missing transverse momentum p_T^{miss} is one of the most important observables in searches for BSM physics. In typical SUSY models, see Section 1.3, a significant amount of p_T^{miss} is expected in the events due to the LSP. In SM processes only neutrinos and mismeasurements of e.g. the jet energies lead to missing transverse momentum, because before a collision the transverse momentum of the colliding protons is nearly negligible. Hence, the missing transverse momentum quantifies the imbalance of all reconstructed particles in an event and is defined as

$$p_T^{\text{miss}} = |\vec{p}_T^{\text{miss}}| = \left| - \sum_{P \text{ Objects}} \vec{p}_{T,i} \right|. \quad (3.3)$$

Jet energy corrections are propagated to the missing transverse momentum vector to reduce a strong bias in events with large hadronic activity.

3.4. Definition of observables

Throughout this thesis different observables are used to define different phase space regions, in particular the signal region and control and validation regions important for the background prediction. All these high level variables are defined based on low level quantities such as the p_T of different objects, or are calculated by complex algorithms combining them.

Total hadronic activity H_T

The hadronic activity H_T is defined as the scalar sum of all jets transverse momenta, that are clustered with the procedure above, and fulfill $|\eta| < 3$ and $p_T > 30 \text{ GeV}$

$$H_T = \sum_{\text{Jets}} |\vec{p}_{T,i}|. \quad (3.4)$$

The transverse mass m_T

The transverse mass of two objects with transverse momentum \vec{p}_T^A and \vec{p}_T^B yields the transverse mass of the mother particle if both particle emerge from the same decay. In cases of invisible decay products, it is a good estimate for the total mother particle mass, because the missing momentum can only be determined in the transverse plane. It is defined as

$$m_T(\vec{p}_T^A, \vec{p}_T^B) = \sqrt{2|\vec{p}_T^A||\vec{p}_T^B|(1 - \cos(\Delta\phi))}, \quad (3.5)$$

where $\Delta\phi$ is the angle between \vec{p}_T^A and \vec{p}_T^B in the transverse plane.

The stransverse mass M_{T2}

In case of two identical particles, decaying both to one invisible and one visible particle, the stransverse mass M_{T2} [129, 130] is a useful generalization of m_T . In this analysis it

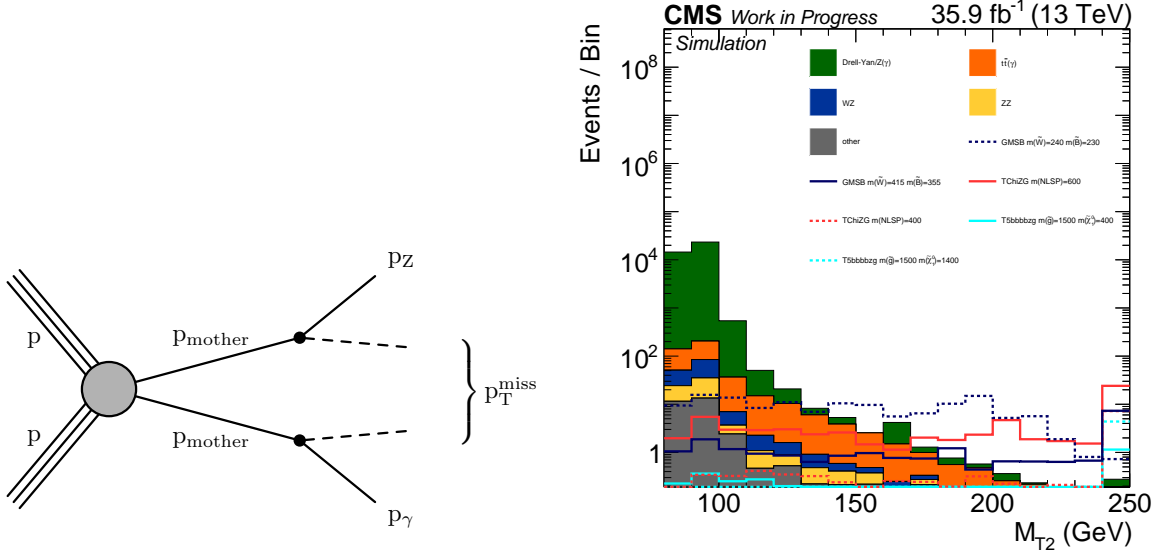


Figure 3.1.: Sketch of decays of pair produced particles to p_T^{miss} and a Z boson or photon respectively (left). Stacked background and different signal points against the stransverse mass M_{T2} (right). Both are obtained from simulation. For each signal model two different signal points are shown. For their masses refer to the legend in the plot.

is calculated to estimate the mass of the NLSP, which decays to an invisible object, the gravitino, and one visible particle, a Z boson or a photon. It is defined as

$$M_{T2} = \min_{\vec{p}_T^{\nu_1} + \vec{p}_T^{\nu_2} = \vec{p}_T^{\text{miss}}} \left(\max \left[m_T(\vec{p}_T^Z, \vec{p}_T^{\nu_1}), m_T(\vec{p}_T^{\gamma}, \vec{p}_T^{\nu_2}) \right] \right), \quad (3.6)$$

where the final value is determined via minimization as indicated by *min* in the equation. Descriptively, the algorithm tries to estimate the transverse mass of the mother particle under the assumption, that the p_T^{miss} is composited of exactly two identical particles each from one decay branch.

For decays of the NLSP in all signal models, the M_{T2} distribution has a cut-off at the mass of the lightest neutralino, while for all SM backgrounds M_{T2} yields much lower values in comparison to the high SUSY masses. See Figure 3.1 for a visualization of the described decay structure and a M_{T2} distribution.

3.5. Lepton pair selection and quality requirements

In the analysis, different datasets triggered with different dilepton triggers are combined, see Section 3.1. Therefore it is possible, that an event is contained in more than one data set. Hence, it is assured with the following procedure, that no event is double counted. At first, all leptons per event are sorted by their transverse momenta. The leading and subleading lepton³ are identified. Their flavor combination then determines the classification of the event as "dielectron", "dimuon", or "electron-muon". For instance, a dielectron

³It is called trailing from now on.

event is classified as such, if the event originates from the `DoubleEG` sample, both the leading and the trailing lepton are electrons, and it is triggered by at least one of the dielectron triggers. This set of conditions ensures the exclusivity of the three selections. In addition, there are some requirements imposed on the dilepton system. The trailing and leading lepton need to be separated at least by a distance of $\Delta R = 0.1$ in the transverse plane, and the invariant dilepton mass $m_{\ell\ell}$ should be larger than 50 GeV. The first requirement provides a cleaning between the lepton collections and ensures, that no lepton is counted twice, while the latter threshold is introduced, because the simulation of the Drell-Yan simulation does not include events with lower dilepton masses. Events with lower invariant dilepton masses are not of interest for this analysis, since in the following only leptons originating from a Z boson decay are selected, resulting in an invariant dilepton mass around the Z boson mass of ≈ 91 GeV.

Hereafter, the dielectron and dimuon selections are combined to a dilepton selection to increase the statistics in the validation, and especially in the signal region.

Additional leptons need to pass the same selection of the trailing lepton.

Also, several event quality filters are applied to reject contaminated events [131]. The rejected events consist mainly of events with faulty detector signals caused by noise or anomalies, spurious energy deposits in ECAL endcap crystals, cosmic muons, muons being misidentified as charged hadrons, or muons produced in scattering processes with the beam halo.

3.6. Used triggers and trigger efficiency measurement

As already pointed out in Section 3.1, the events are recorded with various dilepton triggers. For each dilepton combination ($ee, \mu\mu, e\mu$) multiple triggers are used because of the changing instantaneous luminosity over the 2016 run period, and different triggers were active at different times. The main trigger paths are isolated dilepton triggers, while non-isolated trigger paths are added to increase the efficiency for boosted topologies of the dilepton system. A list of all used HLT trigger paths is given in the appendix in Table ???. While the same flavor dilepton triggers ($ee, \mu\mu$) are used as signal triggers, the different flavor triggers ($e\mu$) are used to select events needed for the background prediction of the top pair production ($t\bar{t}(\gamma)$) background. This will be explained in more in detail in Section 4.2.1. The dilepton triggers altogether have transverse momentum thresholds for the dileptons of around 17 – 33 GeV for the leading lepton, and 8 – 33 GeV for the trailing one. Additional triggers with hadronic activity (H_T) or p_T^{miss} thresholds are relevant for the trigger efficiency measurement, which will be presented in the following.

3.6.1. Trigger efficiency measurement

A trigger efficiency curve is characterized by an inefficient part, a more or less sharp transition ("Turn On") to the efficient part, that is ideally located at the nominal threshold of the trigger path, and a flat efficient part.

Measuring the trigger efficiency is essential to obtain appropriate transverse momentum requirements for the dilepton system. In the signal MC simulation using the FASTSIM

package no trigger simulation is performed, like it is done for the SM background samples. Therefore, the efficiency needs to be measured also on simulation, such that the signal simulation can be scaled accordingly. In addition, the SM simulation samples will be weighted with a factor, correcting for differences in the efficiency between data and simulation.

As indicated, not a single signal trigger or a single trigger for the control region selection is used, but a logical OR combination of all dilepton triggers with the same flavor requirements is used. Thus, for an event only one of the used triggers has to be fired to be selected for the key analysis. Because the total number of produced events including triggered and non triggered events in CMS is not available apparently for data⁴, the combined trigger efficiency ε is measured using a baseline trigger. An appropriate baseline trigger has to be chosen, meaning that it needs to be uncorrelated to the signal trigger which efficiency is being measured. In addition, the baselinetrigger needs to provide a sufficient amount of events to ensure a sample of events large enough to reduce the statistical uncertainty of the measurement. The signal trigger efficiency is defined as the number of events passing baseline and signal trigger, divided by the number of events passing only the baseline trigger:

$$\varepsilon = \frac{\#(baseline \wedge signal)}{baseline}. \quad (3.7)$$

As a consequence, the contribution of the baseline trigger cancels, and the pure signal trigger efficiency is maintained. As baseline triggers a combination of various triggers with H_T thresholds is used. These thresholds range from 200 – 800 GeV. Therefore, the measurement is not performed on the dilepton data streams, but on the H_T datasets. The event selection consists basically of the lepton pair selection introduced in Section 3.5 with an additional $H_T > 200$ GeV requirement to ensure, that the baseline triggers are fully efficient. An additional matching between the selected leptons and the trigger objects responsible for the firing of the trigger is performed.

Since dilepton triggers are used, the beginning of the efficient part needs to be determined for each lepton trigger leg separately. Resulting efficiency curves for all three dilepton combinations measured both on data and simulation are shown in Figure 3.2 against the p_T of the trailing lepton. The statistical uncertainties of the individual bins are calculated using 68% confidence level (CL) Clopper-Pearson intervals [132]. The measurements suffer mainly from the available sample size in the H_T triggered dataset, while the available amount of simulated events is very high per definition. The electron-muon channel is affected the most by this effect. However, the efficiency curves show the structure of multiple transitions into efficient phases, as it is expected from a combination of triggers with very different ranges of thresholds. As indicated by the dotted lines in the plots, the lepton p_T cut was determined to be 20 GeV for the trailing lepton, and 25 GeV for the leading one. Although the dielectron and electron-muon triggers are not yet fully efficient at this threshold, as it is the case for the dimuon trigger, this requirement is imposed also on the other to selections in order to obtain a symmetric lepton selection. The mean plateau efficiencies are shown as a gray band with its statistical uncertainty in the plots. The mean efficiency is also measured on simulation, and all efficiency values are given in

⁴For simulation these informations are available. This is used for further checks to validate the procedure of efficiency measurement.

Table 3.6. These are obtained by requiring both leptons to pass the 25 GeV and 20 GeV threshold, respectively. As can be seen, these values do not differ very much, to the values quoted in the plots, where no lepton p_T requirement in the selection is imposed. Thus, the leading lepton leg is nearly fully efficient, when the trailing lepton has a p_T larger than 20 GeV. Additional efficiency values for the same triggers obtained with a p_T^{miss} baseline selection, that are discussed in the following, are given, too. The efficiency curves after applying the p_T cuts, are also studied in various other distributions to assure the stability of the used triggers.

Table 3.6.: Trigger efficiencies determined both on data and simulation for both baseline trigger configurations for the ee, e μ , and $\mu\mu$ channels.

baseline trigger	Data		Simulation	
	H_T	p_T^{miss}	H_T	p_T^{miss}
ee	$96.0^{+0.2\%}_{-0.2\%}$	$93.7^{+0.3\%}_{-0.3\%}$	$96.60^{+0.01\%}_{-0.01\%}$	$96.79^{+0.02\%}_{-0.02\%}$
e μ	$86.6^{+0.5\%}_{-0.5\%}$	$86.7^{+0.3\%}_{-0.3\%}$	$91.85^{+0.01\%}_{-0.01\%}$	$91.34^{+0.05\%}_{-0.05\%}$
$\mu\mu$	$92.5^{+0.3\%}_{-0.3\%}$	$93.9^{+0.3\%}_{-0.3\%}$	$91.85^{+0.01\%}_{-0.01\%}$	$97.62^{+0.02\%}_{-0.02\%}$

In addition the agreement between rescaled simulation by the factor $\varepsilon' = \varepsilon_{\text{Data}}/\varepsilon_{\text{MC}}$ and data is shown in the ratio plots beneath the efficiency curves. It can be concluded, that the efficiency measurement works fine for both data and simulation, and the efficiencies agree within the systematic uncertainties, which is determined to be 3% to account for the differences between simulation and data. This is indicated with the red uncertainty band in the plots.

As an additional independent check, the whole trigger efficiency measurement was performed also on p_T^{miss} datasets with p_T^{miss} baseline triggers, that have thresholds of around 110 – 600 GeV. This selected phase space region should be more or less orthogonal the H_T selection. It is also much closer to the phase space of the final signal region, since the signal region selection will contain a p_T^{miss} threshold, see Section 4.1.2. Since the efficiency in low H_T region cannot be studied with the H_T baseline selection due to the inherent inefficiency of these triggers, with the p_T^{miss} baseline selection this region can be covered. As can be read from Table 3.6, the values obtained from this method are also in agreement with the efficiencies measured using the H_T selection.

Moreover, the pure simulated trigger efficiency was investigated in dependence of H_T , to strengthen the reliability on the simulation.

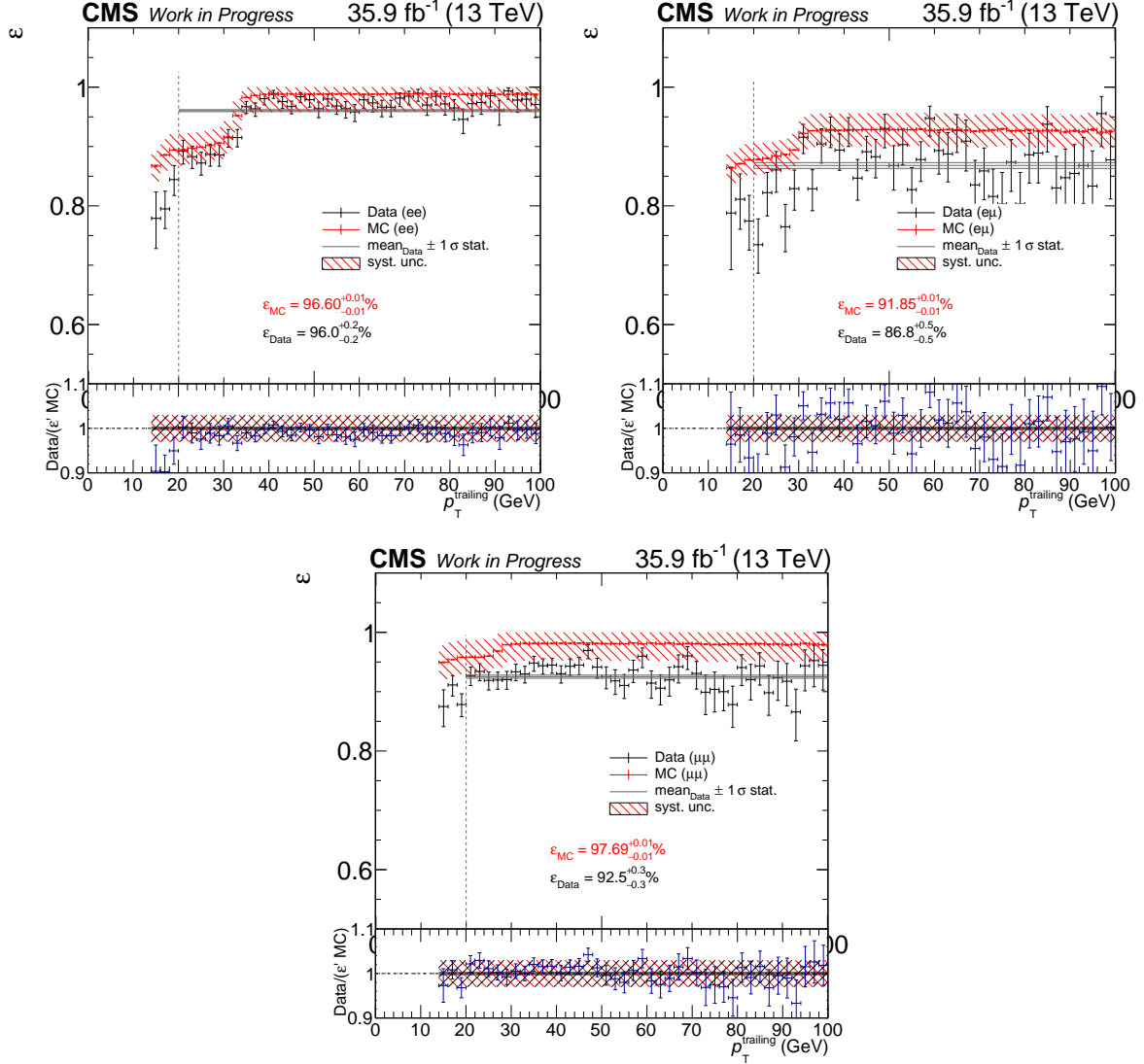


Figure 3.2.: Measurement of the combined efficiency for all dilepton trigger combinations on data (black) and simulation (red) for the ee (top left), $e\mu$ (top right), and $\mu\mu$ (bottom) channels. The measurement is performed using various H_T baseline triggers, while the selection consists of the lepton pair preselection, and a $H_T > 200$ GeV requirement. The mean of the data efficiency with its statistical uncertainty (gray band), and the 3% systematic uncertainty on the measurement (red band) are also shown.

Chapter 4

Analysis strategy and background estimation

Contents

4.1. Event Selection	46
4.2. Background estimation	50
4.3. Study of systematic uncertainties	67

Processes producing SUSY particles have significantly smaller cross sections than most of the SM processes. Therefore, a sophisticated understanding of the relevant production and decay scenarios is needed in order to separate the potential interesting events from the huge amount of SM background. Since this search is targeting SUSY scenarios with bino and wino like NLSPs, final states with photons and Z bosons are expected. In combination with the dileptonic decay of the Z boson, there are not many SM background processes leading to the investigated final state. Especially the requirement of a photon and missing transverse momentum p_T^{miss} in the events reduces most of the background, such that e.g. the QCD background becomes negligible. Leftover are processes producing two same flavor - opposite charge (SFOC) leptons, one photon and missing transverse momentum. The most important ones are $t\bar{t}(\gamma)$ production, Drell-Yan/ $Z(\gamma)$, ZZ , and WZ diboson production. This will be discussed in more detail in Section 4.2.

The key strategy of this analysis is to impose as few as requirements as necessary, to obtain a inclusive event selection, so that many model scenarios can be investigated. Hence, only the existence of all expected final state particles is required, where the Z boson is reconstructed from the two selected leptons. Therefore, the event selection can be rather loose, including also loose requirements on the lepton and photon energies. Not many additional requirements are needed in the following to obtain a sensitive signal region selection.

In the end, in the final selection a counting experiment is performed, where predicted and observed yields are compared, and the result will be interpreted in different signal models.

4.1. Event Selection

In this first section the event selection will be discussed, including region definitions important for the background prediction, which is based on MC simulation. In those control regions, each enriched with a specific type of background events and suppressed signal contribution, the simulation is tuned to match the measured data. In an additional validation region, the background prediction will be examined, and finally a two bin counting experiment will be performed in the signal region. But first, the preselection will be introduced.

4.1.1. Preselection

The preselection acts as a first rough definition of the phase space that is of interest, and rejects inefficient parts of the used triggers. The preselection imposed on the dilepton triggered events is defined as follows:

- exactly one SFOC lepton pair (ee or $\mu\mu$) as defined in Section 3.3,
- at least one photon,
- $\Delta R(\ell_1, \gamma) > 0.3$ and $\Delta R(\ell_2, \gamma) > 0.3$,
- $81 < m_{\ell\ell} < 101 \text{ GeV}$.

The first two conditions imply the existence of the final state particles, including the definition of the physics objects and lepton pair selection explained above. The third requirement reduces contributions of final state radiation photons, that are radiated off by the leptons in electromagnetic showers. The invariant dilepton mass requirement ensures that both leptons originate from an onshell Z boson decay, and reduces different contributions of SM backgrounds that produce dileptons with an invariant mass not in agreement with a Z boson.

4.1.2. Signal region

The signal region (SR) selection is optimized to maintain high sensitivity for various SUSY scenarios both with electroweak and strong production. In the considered models, see Section 1.3.2, the NLSP ($\tilde{\chi}_1^0$) can decay to a Z boson or a photon in combination with gravitinos \tilde{G} , which are undetectable and lead to missing transverse momentum in the event. Therefore, the requirement of missing transverse momentum p_T^{miss} larger than present in most of the SM background processes, enables a good separation between SM background and SUSY signal. The p_T^{miss} threshold is not supposed to be too high, in order to maintain sensitivity to low neutralino masses as well. Additional high separation power is given by the transverse mass M_{T2} , because it yields a good estimate of the NLSP mass. Also, there is no known SM particle which can decay into photons or a Z boson accompanied with neutrinos creating an momentum imbalance in the detector. Therefore, M_{T2} on average is much larger for SUSY processes than for SM processes. Both the M_{T2} and p_T^{miss} distributions of events fulfilling the preselection are shown in Figure 4.1 for the total background and signal points of each model. Hence, the SR is defined by the following criteria:

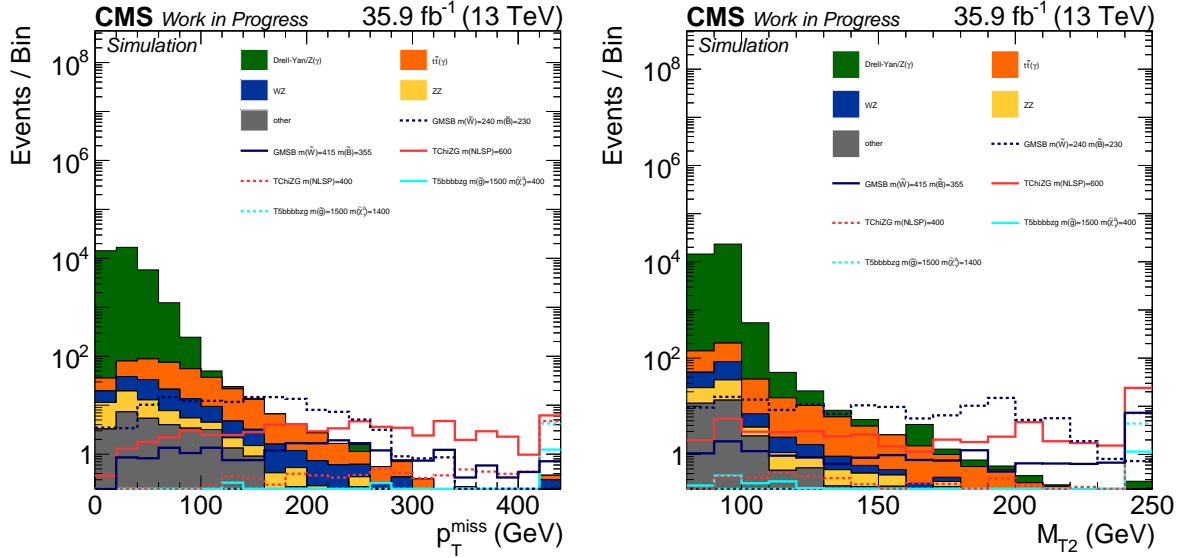


Figure 4.1.: Stacked background and different signal points against p_T^{miss} (left) and the stransverse mass M_{T2} (right). Both are obtained from simulation. For each signal model two different signal points are shown. For their mass parameters refer to the legend in the plots.

- $p_T^{\text{miss}} > 150$ GeV,
- $M_{T2} > 100$ GeV.

The final SR is binned in two search bins in the p_T^{miss} distribution, one ranging from 150 to 200 GeV, and the second one ranging from 200 to infinity, see Section 5.1.

4.1.3. Control regions

Different control regions (CRs) are defined for the four main background contributions, in order develop a background prediction for the corresponding background. These CRs are built such, that they are fully orthogonal to the signal region and among each other and include a large amount of events for precise studies. The main groups of backgrounds are $t\bar{t}(\gamma)$, $DY/Z(\gamma)$, WZ , and ZZ production.

$t\bar{t}(\gamma)$ - control region

To obtain a CR for the $t\bar{t}(\gamma)$ background, the flavor symmetry of the process is exploited. The two top quarks can decay independently with the same probability to an electron or a muon, resulting in an equal number of same flavor and different flavor final state events. The different flavor triggers are needed to guarantee a basis data set containing a sufficient amount of events. In addition, the background can be studied in the same high p_T^{miss} and M_{T2} regions where the SR is defined due to the underlying symmetry of the dilepton production. The preselection criteria need to be adjusted accordingly, resulting in a CR definition of

- exactly one different flavor - opposite charge (DFOC) lepton pair ($e\mu$),
- at least one photon,
- $\Delta R(\ell_1, \gamma) > 0.3$ and $\Delta R(\ell_2, \gamma) > 0.3$.

The invariant dilepton mass window requirement is removed from the preselection, since the reconstructed dilepton mass is not in coincidence with the Z boson mass. In contrast, it shows a continuous distribution different from the top quark mass, because the neutrinos originating from the leptonic top decays cannot be reconstructed individually and are therefore not considered in the calculation. The requirement being responsible for the orthogonality to the SR is the different dilepton composition requirement.

Drell-Yan/ $Z(\gamma)$ - control region

The Drell-Yan/ $Z(\gamma)$ background has nearly the same phenomenological topology as the SUSY signal, except for lower missing transverse momentum, since it is mainly present due to mismeasurements of jets. Therefore, the p_T^{miss} distribution of the Drell-Yan/ $Z(\gamma)$ background is defined by the p_T^{miss} resolution of the detector and reconstruction. The final control region definition on top of the preselection reads

- $p_T^{\text{miss}} < 100 \text{ GeV}$.

This region is orthogonal to the SR per definition due to the inverted p_T^{miss} requirement.

WZ - control region

In order to obtain a high purity WZ control region, the SFOC dilepton criteria is adjusted such, that the fully leptonic decay of the diboson system is studied. As in the preselection, a SFOC lepton pair is required, but the additional lepton veto is removed. Hence, the existence of third lepton, which can be either an electron or a muon, is demanded. This ensures exclusivity between the SR and this CR. Since the $W \rightarrow 2\ell\nu$ boson decays are selected, with the help of additional p_T^{miss} and m_T requirements a further purification of WZ diboson production events is achieved. the transverse mass m_T is calculated using the third lepton assumed to come from the W boson and the missing transverse momentum, and is therefore an estimate for the W boson mass. In the identification of the lepton pair belonging to the decayed Z boson, all combinations fulfilling flavor and charge requirements are tested. In case of multiple valid combinations, the combination with the invariant dilepton mass closest to the Z boson mass is chosen. To ensure a selection with a suitable amount of data, since the cross section for diboson production is rather low, the existence of at least one photon from the preselection is removed. The final region selection reads

- exactly one SFOC lepton pair (ee or $\mu\mu$),
- exactly one additional third lepton (e or μ),
- $\Delta R(\ell_1, \gamma) > 0.3$ and $\Delta R(\ell_2, \gamma) > 0.3$,
- $81 < m_{\ell\ell} < 101 \text{ GeV}$,
- $p_T^{\text{miss}} > 70 \text{ GeV}$,

- $m_T(\vec{p}_T^{\text{miss}}, p_{\ell_3}) > 50 \text{ GeV}$.

ZZ - control region

The strategy to achieve a pure ZZ diboson selection that is not overlapping with the SR selection is very similar to the WZ CR selection described above. By selecting events, where both Z bosons decay leptonically to charged leptons (ee or $\mu\mu$), per definition an exclusive control region is obtained. As in the WZ CR selection, flavor and charge requirements are considered to construct Z boson candidates from the four selected leptons. In cases, where multiple valid solutions for the reconstruction of two Z bosons exist, the possibility with the first Z boson candidate mass closest to the nominal Z boson mass is chosen. The second Z boson candidate has to fulfill a looser mass agreement compared to the first one. Also, the existence of a photon in the event is not required. In total the selection criteria read:

- exactly two SFOC lepton pairs (ee or $\mu\mu$),
- $\Delta R(\ell_1, \gamma) > 0.3$ and $\Delta R(\ell_2, \gamma) > 0.3$ for the first pair,
- $76 \text{ GeV} < m_{\ell\ell} < 106 \text{ GeV}$ for the mass of the first Z boson candidate,
- $50 \text{ GeV} < m_{\ell\ell} < 130 \text{ GeV}$ for the mass of the second Z boson candidate.

4.1.3.1. Validation region

An additional validation region (VR) is constructed, where the developed background predictions are verified by performing data to background prediction comparisons. Therefore, it is convenient to choose the VR close in phase space to the SR. This is achieved by applying the same selection requirements as for the SR, but demanding either the p_T^{miss} or the M_{T2} requirement to fail. Hence, the VR is built as a sideband to the SR. The VR must also not overlap with the DY/Z(γ) CR, thus a minimal p_T^{miss} requirement needs to be imposed. The selection requirements for the VR in addition to the preselection are the following:

- $p_T^{\text{miss}} > 100 \text{ GeV}$,
- either $p_T^{\text{miss}} < 150 \text{ GeV}$ or $M_{T2} > 100 \text{ GeV}$.

A visualization of the signal, validation, and DY/Z(γ) control region definitions in the M_{T2} - p_T^{miss} plane can be found in Figure 4.2. Two dimensional histograms for the number of expected events motivating the region definitions are shown in Figure 4.3 for all background processes, together with distributions of different benchmark points for all three considered signal models. These distributions show also specific features of the considered signal models regarding important kinematic observables. Because the TChiZG model is a one parameter scan, and the only free parameter is the NLSP mass, it directly determines the maximum amount of transverse momentum for the decay products and thus directly the boson p_T and the p_T^{miss} originating from the gravitinos. Hence, p_T^{miss} and M_{T2} calculated from the bosons and p_T^{miss} are strongly correlated. Also, the endpoints of the p_T^{miss} and M_{T2} distributions are of the same order and coincide with the NLSP mass. In case of the strong SMS, this is not directly the case. Since this is a two dimensional parameter scan, the

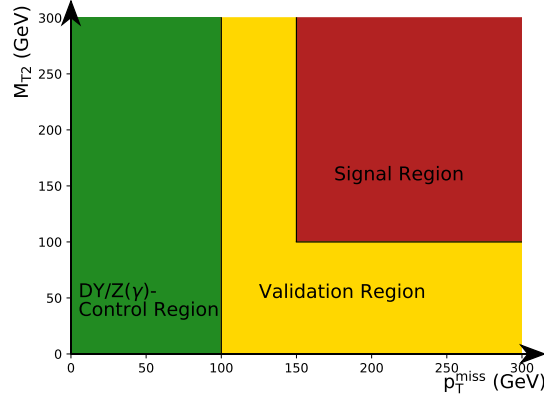


Figure 4.2.: Visualization of the definition of the signal, validation and $DY/Z(\gamma)$ control region in the M_{T2} - p_T^{miss} plane.

event kinematic depends also on the mass difference of the gluino and the NLSP mass, as discussed in Section 1.3.2. In cases where the mass difference is small, the kinematics evolve similar as for the EWK SMS, while for larger mass differences, as shown in Figure 4.3, the correlation between M_{T2} and p_T^{miss} is much weaker and the distributions are much broader. The distributions of the GMSB model behave like a mixture of the two SMSs, depending on the wino and bino masses.

And most importantly, the signal events mainly populate the SR for all models, with small contributions in the CRs and the VR, while the majority of the background events contribute to the $DY/Z(\gamma)$ CR and a minor part to the VR. Only a minority contributes to the SR, as it is desired. In total, a good separation between background and signal is achieved.

4.2. Background estimation

In this section the used background estimation methods are discussed, including the study of systematic effects. The total background is composited of $t\bar{t}(\gamma)$ production, Drell-Yan and $Z(\gamma)$ events, WZ and ZZ diboson production, and a remaining group of backgrounds, composited of e.g. singletop and triboson production (See Section 3.2 and Section 4.1.3). The relative amounts for all background contributions in the two SR bins are depicted in Figure 4.4. The most dominating background is $t\bar{t}(\gamma)$, followed by WZ , ZZ , and Drell-Yan/ $Z(\gamma)$.

The leptonic decays of the top pairs generated in association with a photon significantly contribute to the SR, because the final state signatures appear very similar to those of the SUSY models and the production cross section is very high. If both W bosons decay leptonically, a SFOC lepton pair in connection with neutrinos can be produced, that generate a large amount of p_T^{miss} in the detector. Also real photons can be produced in the hard interaction, or can be radiated off in the initial or the final state by participating charged particles. Since the total mass of the top pair cannot be reconstructed due to the

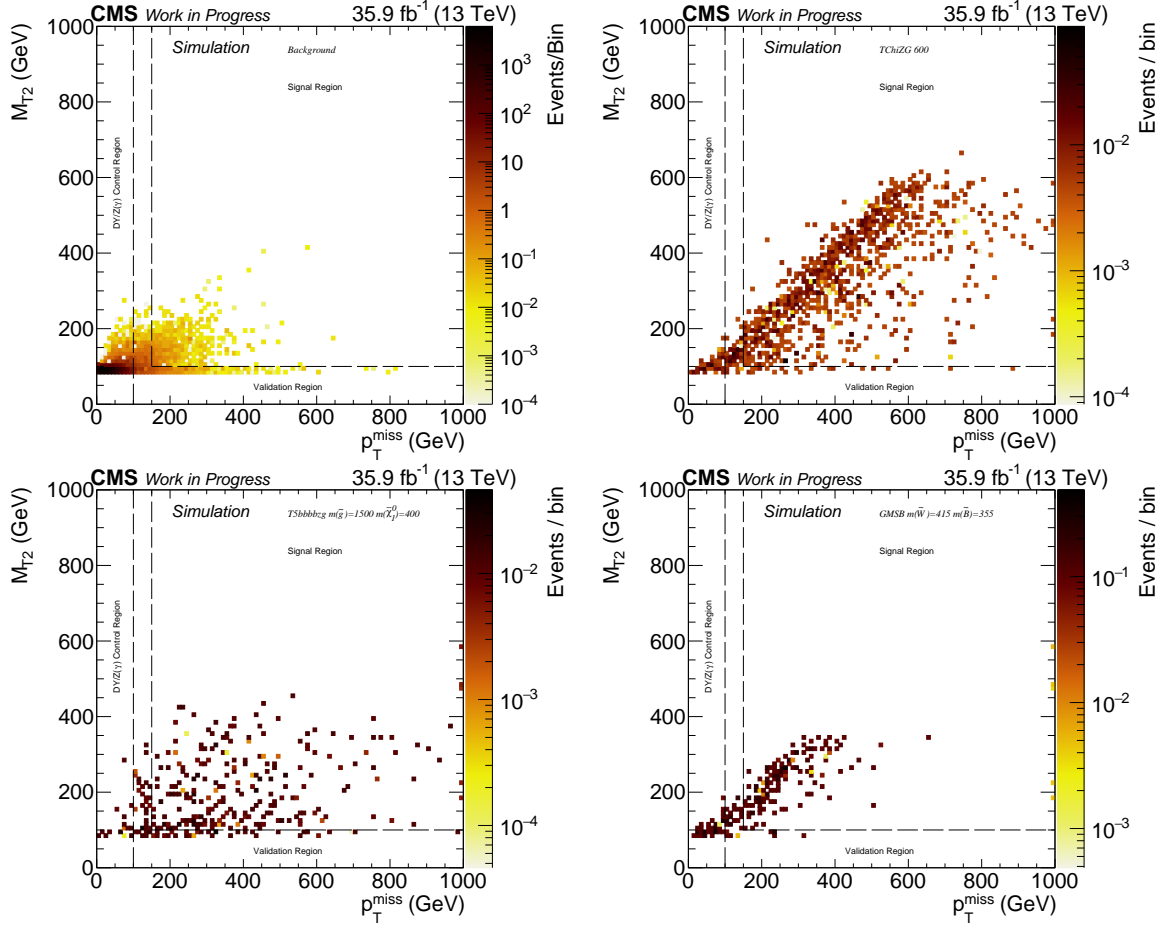


Figure 4.3.: Distribution of the total number of expected background events in the M_{T2} - p_T^{miss} plane (upper left). Distributions for the number of expected signal events for the TChiZG SMS with an NLSP mass of 600 GeV (upper right), the T5bbbbZG SMS with a gluino mass of 1.5 TeV and a neutralino mass of 400 GeV (bottom left), and the GMSB model with $m(\tilde{W} = 455 \text{ GeV})$ and $m(\tilde{B} = 355 \text{ GeV})$ (bottom right).

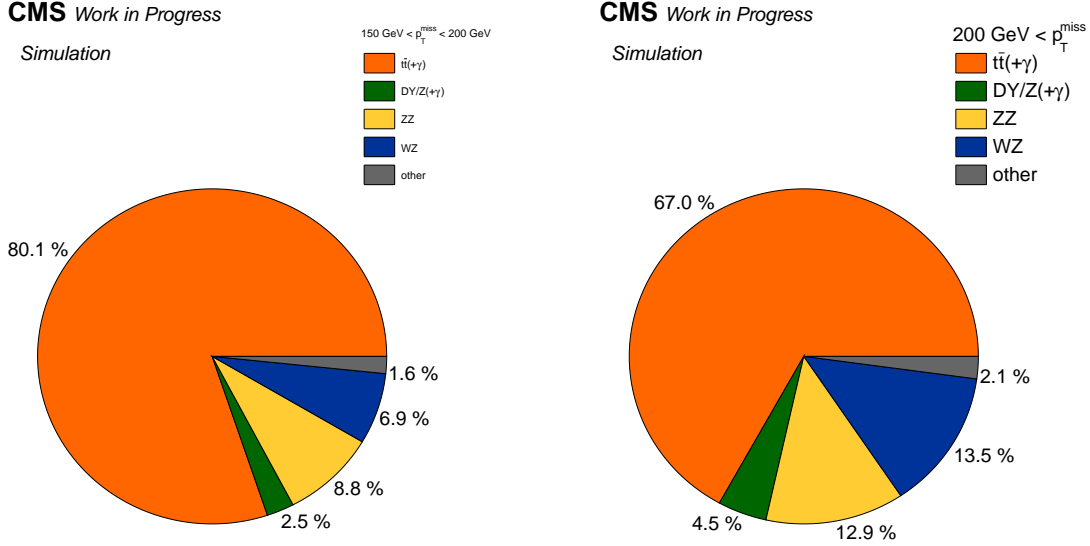


Figure 4.4.: Relative amounts for all group of considered backgrounds for the two search bins in the SR.

momentum imbalance, there is a sufficient probability to measure an invariant dilepton mass close to the Z boson mass.

In the Drell-Yan process, in context with FSR or ISR, and in $Z\gamma$ production, directly an on-shell Z boson is produced, thus the $m_{\ell\ell}$ requirement for the dileptons in the SR is fulfilled. Although additional a photon is produced, this background does not contribute significantly to the SR, because only nongenuine p_T^{miss} is generated in the process due to mismeasurements and therefore the p_T^{miss} distribution drops steeply.

WZ production is also an important background for this search, since the W boson can decay leptonically and therefore creates a sufficient amount of genuine p_T^{miss} to pass the SR requirements. While a photon can be generated in all possible radiation processes, an additional electron or jet originating from the W boson can fake a photon signature in the detector. In cases of real photons, the additional lepton can also be lost in the reconstruction.

Lastly, the ZZ event signature can be very similar to the one expected from the considered SUSY signals. One boson can decay to a pair of charged leptons, while the other decays to neutrinos leading to a large amount of p_T^{miss} in the event. Together with FSR or ISR of a photon, it mimics the signal topology in many ways.

If the different background processes are compared, the diboson processes may have a more similar event kinematic than the $t\bar{t}(\gamma)$ process, but due to the lower diboson production cross sections, and the small branching fraction for a Z or W boson to decay to charged leptons, the $t\bar{t}(\gamma)$ background dominates the other contributions.

The strategy to perform a sophisticated background prediction is based on MC simulation for all backgrounds. As mentioned in Section 4.1.3, different CRs are developed, that are enriched with corresponding background events. In those CRs scale factors (SF) α_i are calculated by scaling the total simulation to the measured data yield. Contributions of

other backgrounds in the CR are considered in the calculation by fixing their contribution, thus only one background is scaled. The SFs are calculated via the following formula:

$$1 = \frac{\#Data}{\#FixedBackground + \alpha_i \cdot \#BackgroundToScale} \quad (4.1)$$

$$\Rightarrow \alpha_i = \frac{\#Data - \#FixedBackground}{\#BackgroundToScale}. \quad (4.2)$$

Due to the used method, which is performed similar in each CR, possible uncertainties in the normalization cancel, and only uncertainties in the shape need to be considered, see Section 4.3. The uncertainty arising from the SF calculation is purely of statistical origin, and is calculated via error propagation

$$\sigma_{\alpha_i}^2 = \sigma_D^2 \cdot \left(\frac{D}{B}\right)^2 + \sigma_F^2 \cdot \left(\frac{F}{B}\right)^2 + \sigma_B^2 \cdot \left(\frac{D-F}{B^2}\right)^2, \quad (4.3)$$

where $B = \#BackgroundToScale$, $F = \#FixedBackground$, $D = \#Data$, and σ_i are the corresponding statistical uncertainties. These are assumed to be uncorrelated Poissonian uncertainties, and can be calculated via $\sigma_i = \sqrt{N_i}$, where N is the associated total integral in the selection. In the case of MC simulation, for the calculation of the SF the normalized event yield is used, whereas in the error calculation the pure MC event count is considered to reflect the underlying precision of the simulation. This method is referred to as the "integral method" in the following.

After determining all SFs, the background prediction will be tested in the VR. Therefore, the simulated backgrounds in the VR will be scaled accordingly, and the result will be investigated, see Section 4.2.6.

4.2.1. Top pair production in association with a photon

As shown in Figure 4.4, the main background contribution is $t\bar{t}(\gamma)$, which is composed of standard top pair production with and without photon radiation, and top-pair production in association with a photon, while the latter dominates. Both compositions will be determined together by rescaling the simulation, such that the integral of events of the MC simulation in the CR matches the integral of events in data as explained in Section 4.2. The raw and rescaled yields of the simulation, together with the observation in the CR are quoted in Table 4.1. The overall purity of the selection is of the order of 84.62%. For the scaled event yields, only weights to account for the trigger efficiency correction and a global weight as mentioned in Section 3.2 to normalize the simulation to the physical expectation are made use of. With the integral method applied, the SF given in Equation (4.4) is obtained.

$$\alpha_{t\bar{t}(\gamma)} = 0.806 \pm 0.324(stat.) [\hat{=} 4.02\%]. \quad (4.4)$$

After application of $\alpha_{t\bar{t}(\gamma)}$, the number of events in data and total simulation match per definition.

Since the analyzed final state in this CR is very sensitive to higher order effects such as jet and photon radiation, and complex matrix elements are needed to describe the hard interaction, and these are very hard to model in the simulation, a SF differing from unity is

Table 4.1.: Yields in the $t\bar{t}(\gamma)$ CR for the pure simulation and measured data.

process	raw simulation	simulation	data
$t\bar{t}$	12077	416.93	
$t\bar{t}\gamma$	128396	1420.19	
sum	140473	1837.12	1750
other	14631	269.21	

not unexpected. Because the generation of MC simulation in general is time and resource consuming, simplifications are made on e.g. radiation effects, and not all aspects of a specific process are calculated and generated at NLO, although MC@NLO was used for the generation of the $t\bar{t}\gamma$ sample. NNLO electroweak effects can cause negative corrections for example due to destructive terms in higher order corrections. The uncertainty of the order of 4% indicates, that a sufficient amount of events is present in the corresponding CR.

The resulting prediction shows a good agreement with data, as can be seen from the p_T^{miss} and M_{T2} distributions in the CR after rescaling in Figure 4.5. The uncertainty of the fit method is of statistical origin, and is treated as a systematic in the following. The agreement of additional important observables, such as the transverse momentum of the photon and both leptons, is also investigated, and the plots can be found in the appendix in Figure ??**TODO November 6, 2018: ref.** To strengthen the confidence in the outcome, Kolmogorov-Smirnov [133] tests are performed to study the shape agreement. No significant disagreement is found, and the KS-values from the tests results are quoted on the plots for each individual distribution. KS-values much larger than 0.1 indicate agreement between the input distributions. In order to study a possible bias of observables not well modeled within the simulation, additional cross checks are performed. Similar to the SF calculation in the integral method, SFs are determined via χ^2 minimization in the same CRs. Albeit this method is somewhat correlated to the method explained above, it enables the possibility to study influences of different distributions in different binnings. Therefore, $\alpha_{t\bar{t}(\gamma)}$ was varied in a range in small steps of 0.01 for each binning and distribution, and for every iteration the simulation was scaled and the χ^2 was calculated, which is defined as:

$$\chi^2 = \sum_i^{N_{bins}} \frac{\left(N_{i,bin}^{obs} - N_{i,bin}^{predicted}\right)^2}{N_{i,bin}^{predicted}}. \quad (4.5)$$

The best fit value is determined to be at the minimum of the χ^2 distribution, which is obtained by fitting a polynomial of fourth grade to the measured points. The uncertainty of the χ^2 -fit method, that is also of statistical origin, is calculated by taking the difference between the best fit value and the values, where $\chi^2 = \chi_{BestFit}^2 + 1$. An example fit in the p_T^{miss} distribution is shown in Figure 4.6 left. The number of degrees of freedom (ndf) is given by the number of bins used to obtain the χ^2 distribution reduced by the number of parameters that are being optimized. The only free parameter is $\alpha_{t\bar{t}(\gamma)}$, so ndf equals the bin number subtracted by one. The resulting curves are smooth, indicating a proper performance of the fit. A comparison of all obtained SFs for the different setups and the SF obtained by the integral method is shown in Figure 4.6 right. No significant deviation

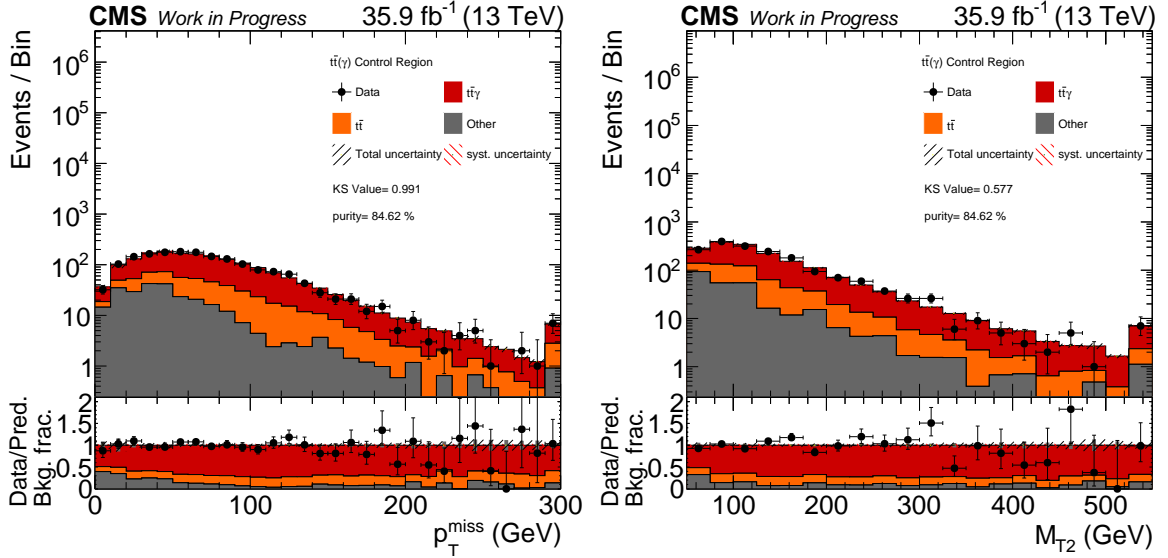


Figure 4.5.: Comparisons between data and rescaled simulation in the $t\bar{t}(\gamma)$ CR in the p_T^{miss} and M_{T2} distribution. Below each plot, a ratio between data and prediction is shown. The uncertainty bands correspond to the systematic (red) and total uncertainty (gray). In addition, in the ratio plot the relative composition of the backgrounds is visualized. KS-values for the performed Kolmogorov-Smirnov test are also quoted.

can be observed, and all SFs are in agreement within each other. Hence, the scaling of the $t\bar{t}(\gamma)$ background seems stable and well described in the CR.

Further studies

Since the $t\bar{t}(\gamma)$ background is the most dominating one, further studies are realized in which the underlying MC simulation samples and their combination are examined. Hence, different overlap removal procedures, see Section 3.2, and different available cross sections are used, while the fit procedure itself is varied. In addition, available corrections to improve the modeling of jet radiation in the initial state, and corrections to enhance the description of the top quark p_T distribution, that are used both to correct the LO samples and the samples that are generated with POWHEG (see Section 3.2), are applied in different combinations. The used fit methods include a χ^2 -template fit, where the ratio between the fractions of the $t\bar{t}$ and $t\bar{t}\gamma$ simulation is left free as an additional parameter, and a fit where only the $t\bar{t}\gamma$ simulation is made use of. Eventually, no substantial differences are observed, and the best performance and stability is provided by the initial approach explained above in detail.

4.2.2. Drell-Yan and $Z\gamma$ diboson production

Although the Drell-Yan and dibosonic $Z\gamma$ background is admittedly small in the two SR bins, its contribution is the fourth largest. Hence, it needs to be assured, that the background is modeled well. As in the case of the $t\bar{t}(\gamma)$ background, it is composited of

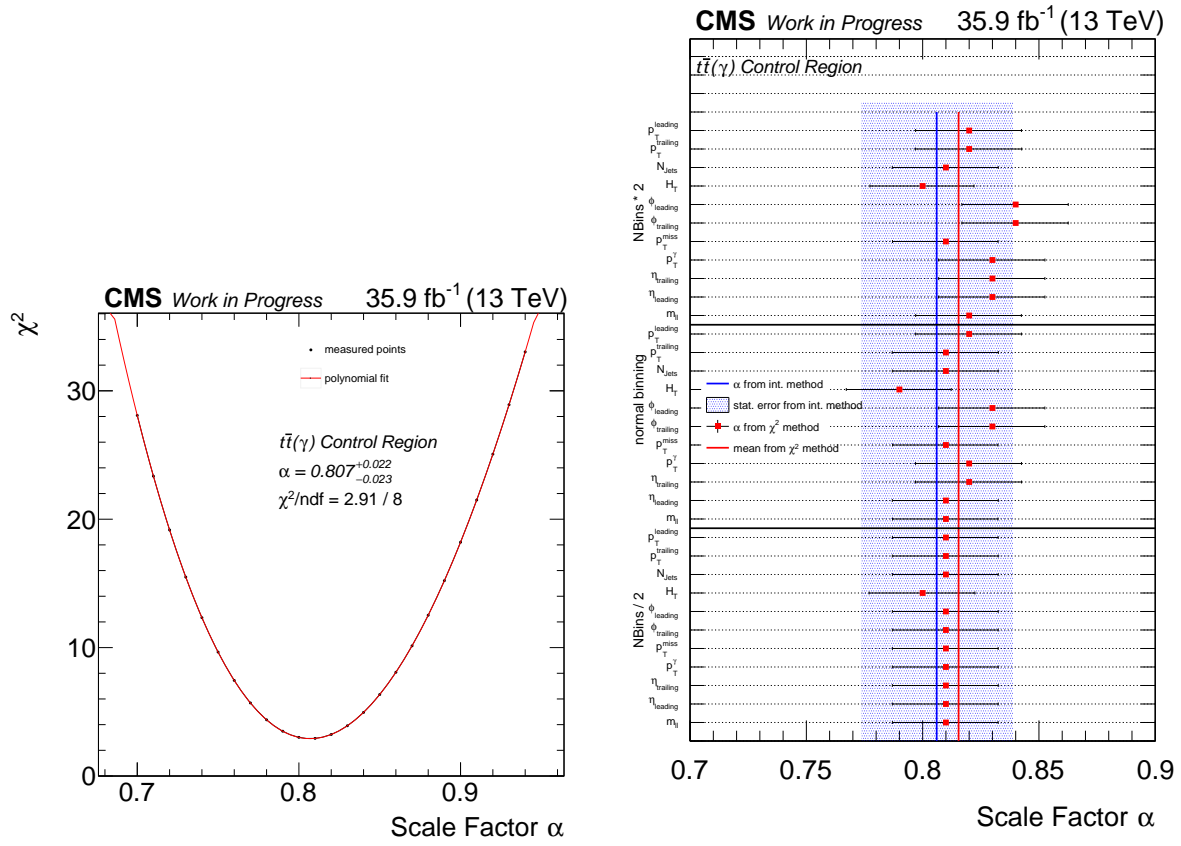


Figure 4.6.: Example χ^2 fit in the $t\bar{t}(\gamma)$ CR in the p_T^{miss} distribution (left) with the polynomial fit. All fit results compared with the SF obtained from the integral method in different binnings and variables (right.)

Table 4.2.: Yields in the $DY/Z(\gamma)$ CR for the pure simulation and measured data.

process	raw simulation	simulation	data
Drell-Yan	11710	13008.83	
$Z\gamma$	170161	22692.88	
sum	181871	35701.41	38419
other	87337	374.00	

two major parts, the Drell-Yan process, where quarks annihilate to off shell photons or Z bosons and generate leptons in their decays, and the diboson production of $Z\gamma$ pairs. The integral method as explained above is used to determine the SF $\alpha_{DY/Z(\gamma)}$ in the dedicated CR defined in Section 4.1.3. The relevant event yields are quoted in Table 4.2, and the resulting SF is stated in Equation (4.6). With a purity of about 99%, and a total event count that large, a precise SF determination is feasible, as can be concluded also from the small statistical uncertainty of $\approx 1\%$. The agreement between simulation and data is very good, even before application of $\alpha_{DY/Z(\gamma)}$, since it equals nearly unity. The post-scaling distributions of p_T^{miss} and M_{T2} are shown in Figure 4.7. They show overall a good agreement, only in the high M_{T2} region there are some fluctuations due to the limited statistics being present both in data and simulation. Further distributions are investigated, that can be found in the appendix in Figure ???. The same cross checks as for the $t\bar{t}(\gamma)$ background are made, including the Kolmogorov-Smirnov tests, and the additional χ^2 -fits with variable bin size in different observables. All in all the KS-values indicate a very good matching between predicted and observed shape, albeit the Kolmogorov-Smirnov test provides a very small KS value for the consistency between the p_T^{miss} distributions. But, this is mainly due to the high statistics in data and therefore a higher absolute discrepancy, contradicting with the lower statistics in simulation, leading to larger fluctuations. These discrepancy is not visible in the ratio shown under the plot.

$$\alpha_{DY/Z(\gamma)} = 1.066 \pm 0.001(\text{stat.})[\triangleq 0.87\%]. \quad (4.6)$$

The χ^2 -fit studies, shown in Figure 4.8 together with an example fit in the p_T^{miss} distribution, show excellent agreement over all variations. Hence, the background prediction seems to work fine also in the $DY/Z(\gamma)$ CR.

4.2.3. WZ diboson production

The diboson production of WZ pairs is the second important background contribution for this analysis. It is also tuned to agree with the measurement in the WZ CR, while the SF α_{WZ} is calculated with the integral method. The expected purity of selected WZ events in this CR is about 84%, and the total event yields given in Table 4.3 point out, that the number of events is sufficient to determine a SF with adequate precision. The agreement beforehand is also very good, although this background is a higher order process and is therefore simulated at NLO, see Section 3.2, which includes several complicated effects the

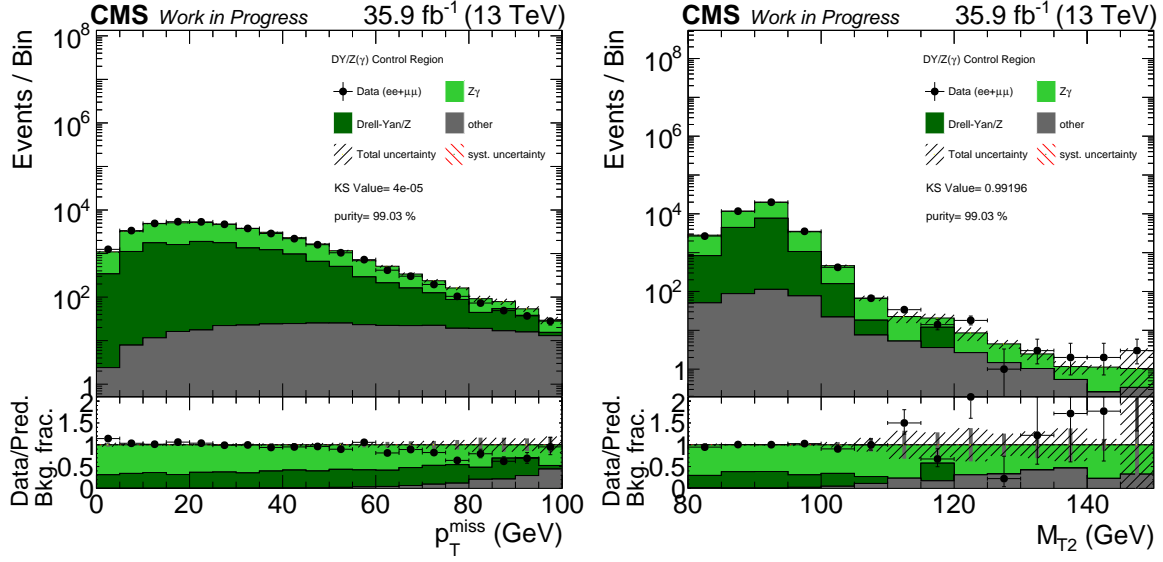


Figure 4.7.: Comparisons between data and rescaled simulation in the DY/ $Z(\gamma)$ CR in the p_T^{miss} and M_{T2} distribution. Below each plot, a ratio between data and prediction is shown. The uncertainty bands correspond to the systematic (red) and total uncertainty (gray). In addition, in the ratio plot the relative composition of the backgrounds is visualized. KS-values for the performed Kolmogorov-Smirnov test are also quoted.

Table 4.3.: Yields in the WZ CR for the pure simulation and measured data.

process	raw simulation	simulation	data
WZ	113744	895.74	
sum	113744	895.74	1193
other	93914	186.94	

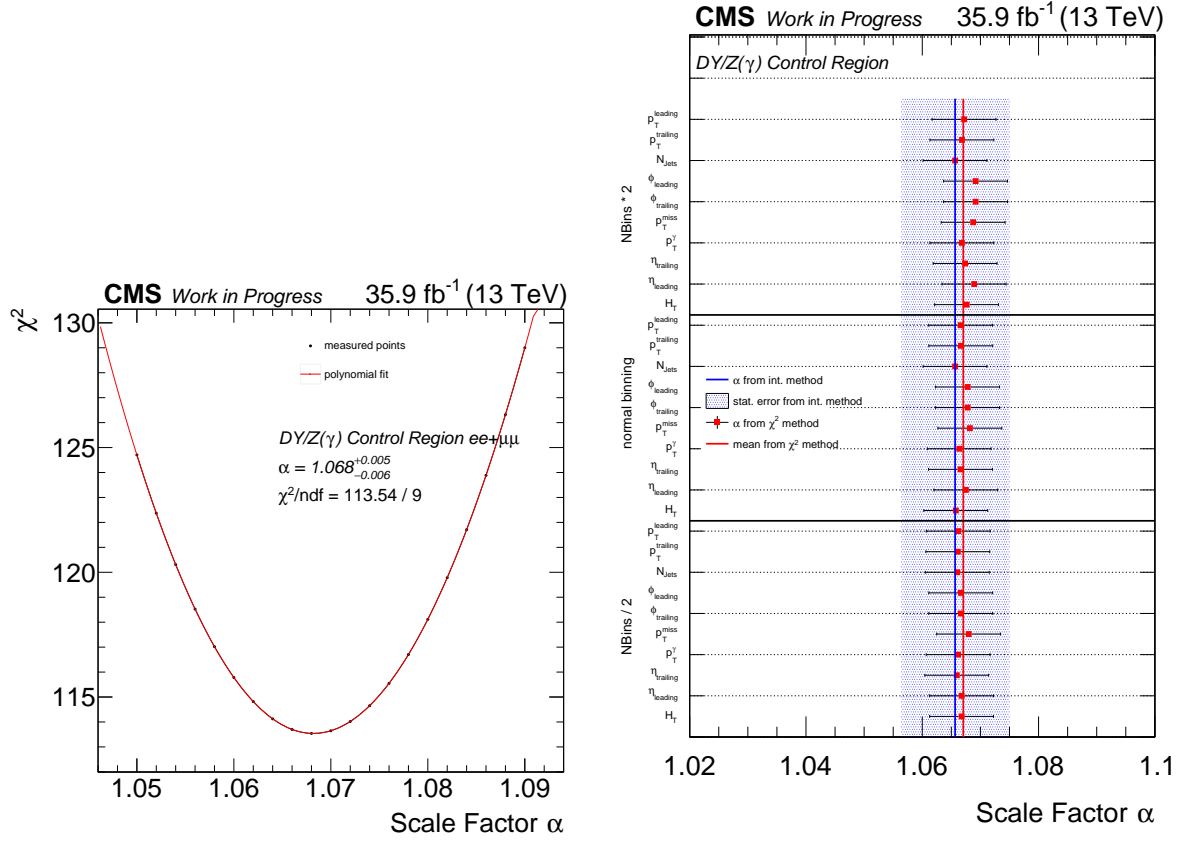


Figure 4.8.: Example χ^2 fit in the $DY/Z(\gamma)$ CR in the p_T^{miss} distribution (left) with the polynomial fit. All fit results compared with the SF obtained from the integral method in different binnings and variables (right.)

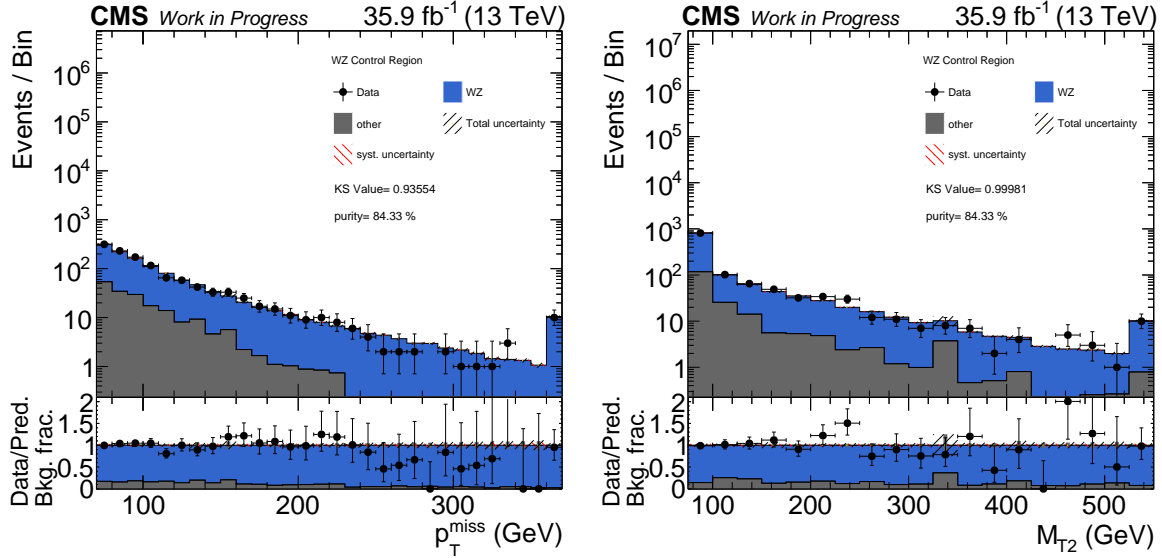


Figure 4.9.: Comparisons between data and rescaled simulation in the WZ CR in the p_T^{miss} and M_{T2} distribution. Below each plot, a ratio between data and prediction is shown. The uncertainty bands correspond to the systematic (red) and total uncertainty (gray). In addition, in the ratio plot the relative composition of the backgrounds is visualized. KS-values for the performed Kolmogorov-Smirnov test are also quoted.

event generator needs to handle properly. The SF $\alpha_{DY/Z(\gamma)}$ is determined to be

$$\alpha_{WZ} = 1.123 \pm 0.037(\text{stat.}) [\triangleq 3.29\%], \quad (4.7)$$

which indicates that usage of NNLO cross sections for the WZ samples is nearly sufficient enough to describe the background. Of course higher order effects can lead to higher cross sections, thus it is not unexpected to obtain a SF varying $\approx 12\%$ from unity. Resulting distributions of the description of the p_T^{miss} and M_{T2} variables are shown in Figure 4.9. As can be seen, the predicted shape is in consistency over the whole range with the observed data, also in the very high p_T^{miss} and M_{T2} regime. This is further confirmed by the additional cross checks, that are also realized in the other two CRs described above. The KS-values close to one strengthen the trust in the background estimation method. The comparison plots for other distributions can be found in the appendix in Figure ???. The χ^2 -fit studies lead to the same outcome, the uncertainties seem to be well estimated and of statistical origin, since no large shape deviation can be observed in the performed fits, as can be seen in Figure 4.10 right. Each individual χ^2 -fit seems to behave properly, see Figure 4.10 left for an example in the p_T^{miss} distribution.

4.2.4. ZZ diboson production

The last important and fourth biggest background contribution is ZZ diboson production, where both Z bosons decay leptonically, one to charged leptons such as electrons or muons, and the other one to neutrinos. To simplify the construction of a dedicated

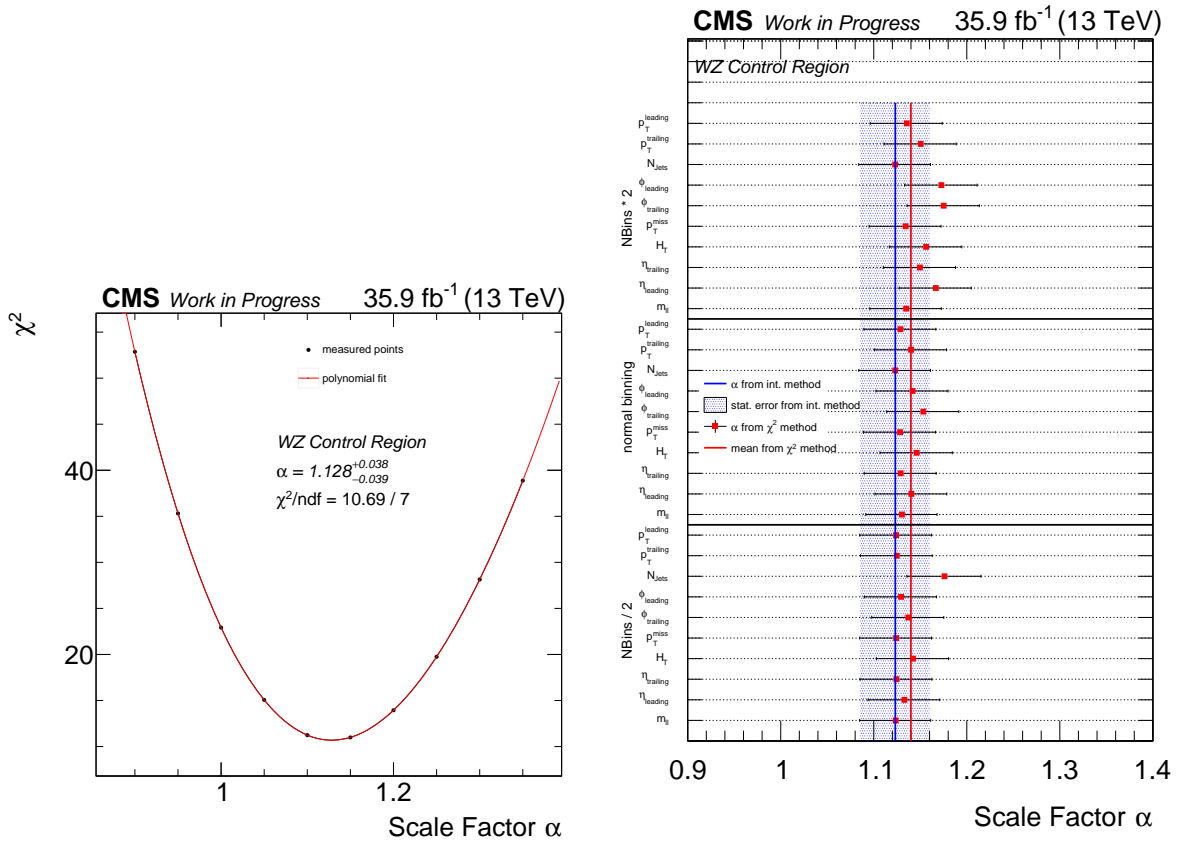


Figure 4.10.: Example χ^2 fit in the WZ CR in the p_T^{miss} distribution (left) with the polynomial fit. All fit results compared with the SF obtained from the integral method in different binnings and variables (right.)

Table 4.4.: Yields in the ZZ CR for the pure simulation and measured data.

process	raw simulation	simulation	data
$ZZ(\rightarrow 2\ell 2\nu)$	5	0.0005	
$ZZ(\rightarrow 4\ell)$	459221	226.94	
sum	459226	226.94	251
other	79	0.07	

CR, as explained in Section 4.1.3, the assumption is made, that there is no difference for the generator to generate neutral or charged leptons. Only the detector response should differ. Therefore, ZZ can be well estimated in a four lepton CR. A pure selection of ZZ events can be established, although the statistics in data is quite low due to small cross section and the low branching fraction for the $Z \rightarrow \ell\ell$ decay. Event counts are quoted in Table 4.4, with a selection purity of nearly 100%. With the integral method applied, a SF α_{ZZ} stated in Equation (4.8) is determined, being relatively close to one.

$$\alpha_{ZZ} = 1.109 \pm 0.064(stat.) [\simeq 5.74\%]. \quad (4.8)$$

Post-fit distributions to show the good agreement in the p_T^{miss} and M_{T2} distribution can be found in Figure 4.11. As mentioned, the precision is limited by the low statistics of the selected sample, but nevertheless is sufficient enough to establish a working background prediction. The shapes agree very well, as it is additionally indicated by the KS-values printed on the plots, also in the high M_{T2} region. The properties of the $ZZ \rightarrow 4\ell$ processes does not allow to study the prediction in the high p_T^{miss} regime, since only nongenuine p_T^{miss} is produced, but agreement of the p_T distributions of the leptons, that are listed in Figure ?? in the appendix, can be translated into the agreement of the p_T^{miss} in the $ZZ \rightarrow 2\ell 2\nu$ background, that is generated with the same event generator. The χ^2 -fit studies, see Figure 4.12, are performed as for the other three background estimations discussed above, and yield the same conclusion, although some fluctuations in the choice of the variable or binning are present due to the lower total event count in the observed data. But, all in all also this background estimation method behaves properly.

4.2.5. Other standard model backgrounds

Additional minor backgrounds, such as triboson processes as $WZ\gamma$, $WW\gamma$, diboson WW and $W\gamma$ production, the production of W bosons in association with jets, and single top processes as listed in Table 3.2, are taken from plane simulation after reweighting them as described in Section 3.2 to the measured luminosity and NLO and NNLO cross sections.

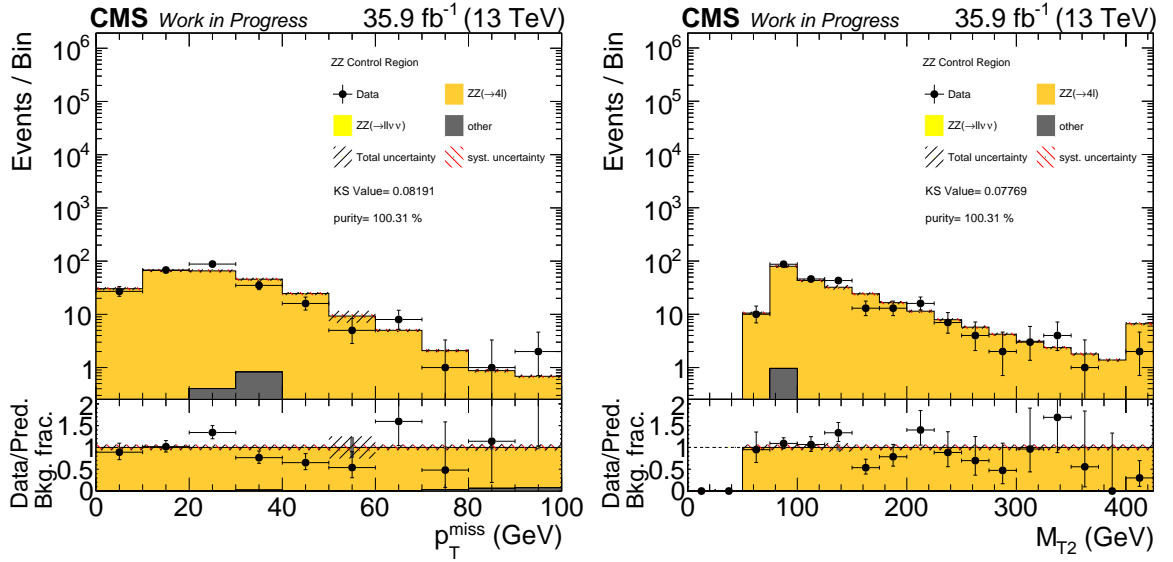


Figure 4.11.: Comparisons between data and rescaled simulation in the ZZ CR in the p_T^{miss} and M_{T2} distribution. Below each plot, a ratio between data and prediction is shown. The uncertainty bands correspond to the systematic (red) and total uncertainty (gray). In addition, in the ratio plot the relative composition of the backgrounds is visualized. KS-values for the performed Kolmogorov-Smirnov test are also quoted.

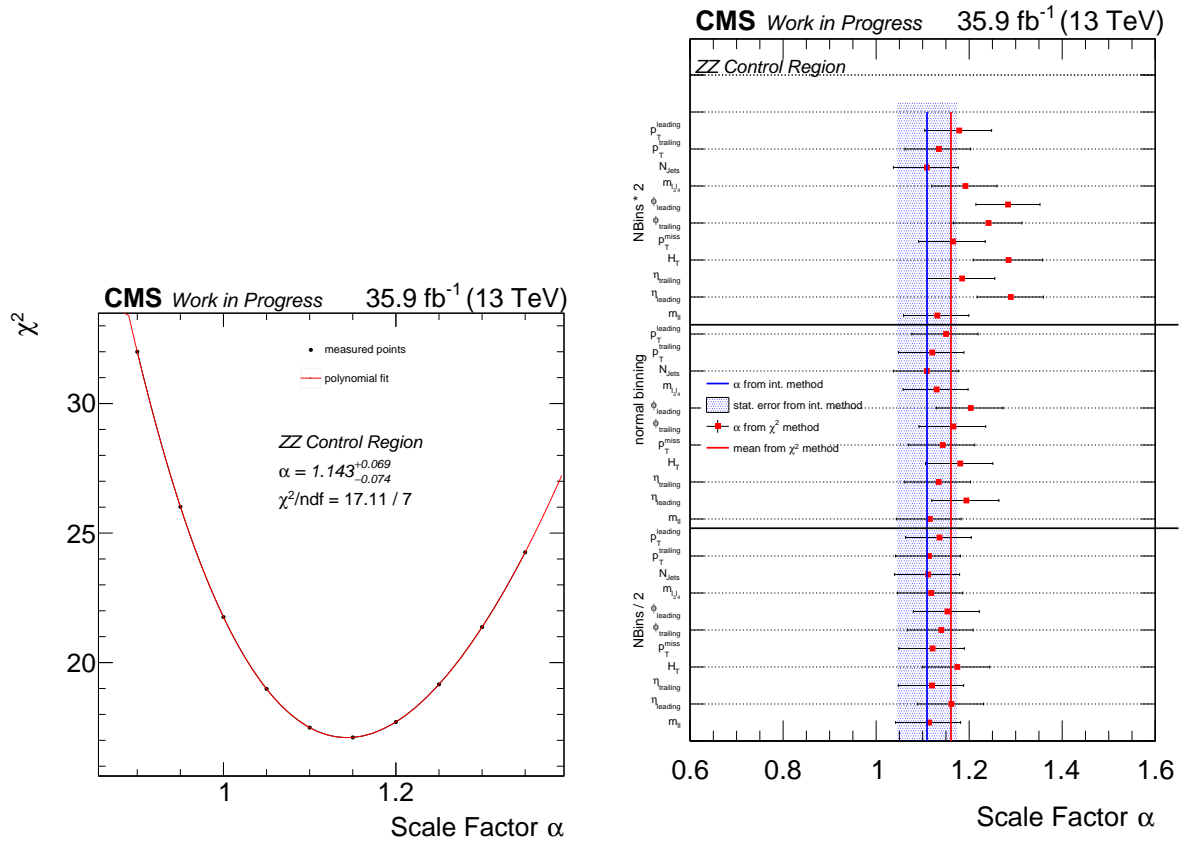


Figure 4.12.: Example χ^2 fit in the ZZ CR in the p_T^{miss} distribution (left) with the polynomial fit. All fit results compared with the SF obtained from the integral method in different binnings and variables (right.)

4.2.6. Validation of the background estimation

After all main backgrounds are tuned in various corresponding CRs and SFs are determined, and the remainder is taken from pure simulation, the background prediction is validated in the VR defined in Section 4.1.3. In phasespace it is very close to the SR where the background prediction shall work sufficiently well, and therefore the VR is ideal to study the obtained background prediction.

Resulting comparisons between prediction and observed data in different distributions are shown in Figure 4.13 for the most important variables, such as p_T^{miss} and M_{T2} , together with p_T distributions of the leading and trailing lepton. Comparisons for the photon p_T and the invariant dilepton mass $m_{\ell\ell}$ distributions are shown in Figure 4.14.

Overall, the agreement is very good in all distributions, although being limited by the lower statistics in some kinematic regions. The same Kolmogorov-Smirnov tests as for the different CRs are performed to gain more trust in the background prediction. As can be read from the resulting KS-values, each quoted on the corresponding plot, the shape agreement considering statistical uncertainties and systematic uncertainties originating from the statistical ones from the integral method, is very good. With 97 data events measured and 93.6 predicted, the total agreement is very good.

Therefore, the background prediction is assumed to work fine in the SR due to the similar kinematics in the VR based on the design as a kinematic sideband in p_T^{miss} and M_{T2} .

4.2.7. Signal contamination

If case of measurable SUSY signals, it would of course not only produce events being observable in the SR, but also some of them may appear in the CRs that are used to determine a proper background prediction. To account for this effect, the so-called signal contamination of the background CRs is not considered in the background estimation itself, but is rather translated into a reduction of the predicted signal yield in the SR. Hence, at first the signal contamination needs to be measured for each signal point of all samples individually in all CRs.

Therefore, the fraction of expected signal events relative to the total amount of background events in each CR is measured. Examples for the contamination of the TChiZG SMS in the DY/Z(γ) CR and the GMSB model in the WZ CR are shown in Figure 4.15, because they are the largest ones observed. As can be seen, the contributions of signal events are mainly negligible, although the signal contamination reaches $\approx 3\%$ for very low bino and wino masses in the GMSB model.

To account for those effects, these relative fractions are used to lower the signal expectation in each SR bin individually. This can be accomplished in a simple way, since the background prediction method is based on simulation which is rescaled with constant SFs. If ρ is the fraction of signal events in the CR, in each SR bin the absolute signal event yield reduced with the following formula

$$\#signal_{after} = \#signal_{before} - \rho \cdot \#background, \quad (4.9)$$

where $\#signal_{before}$ and $\#signal_{after}$ are the total number of signal events per bin before and after the correction, and $\#background$ is the number of predicted background events

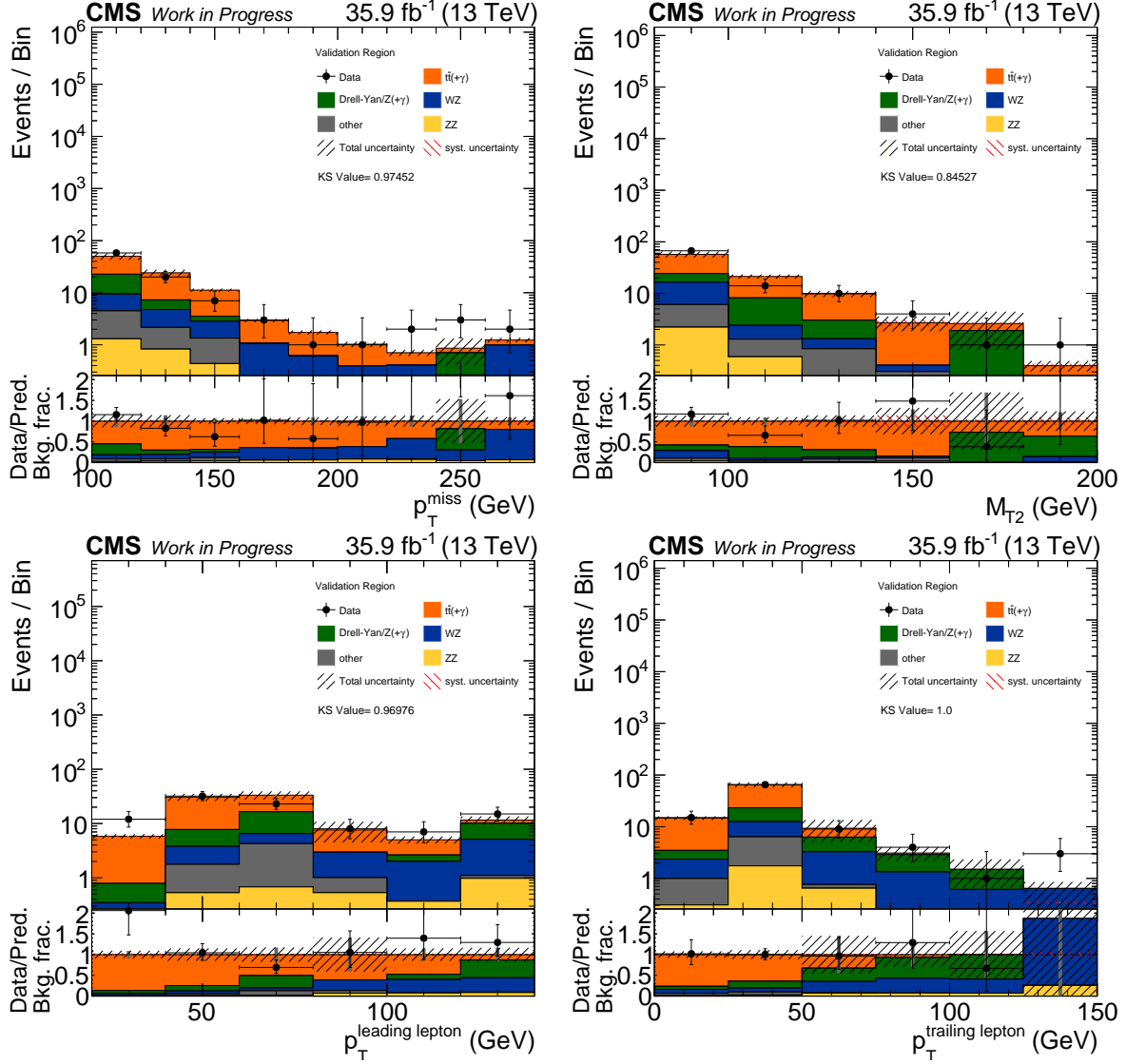


Figure 4.13.: Comparisons between data and rescaled simulation in theVR in the p_T^{miss} , M_{T2} , and lepton p_T distributions. Below each plot, a ratio between data and prediction is shown. The uncertainty bands correspond to the systematic (re) and total uncertainty (gray). In addition, in the ratio plot the relative composition of the backgrounds is visualized. KS-values for the performed Kolmogorov-Smirnov test are also quoted.

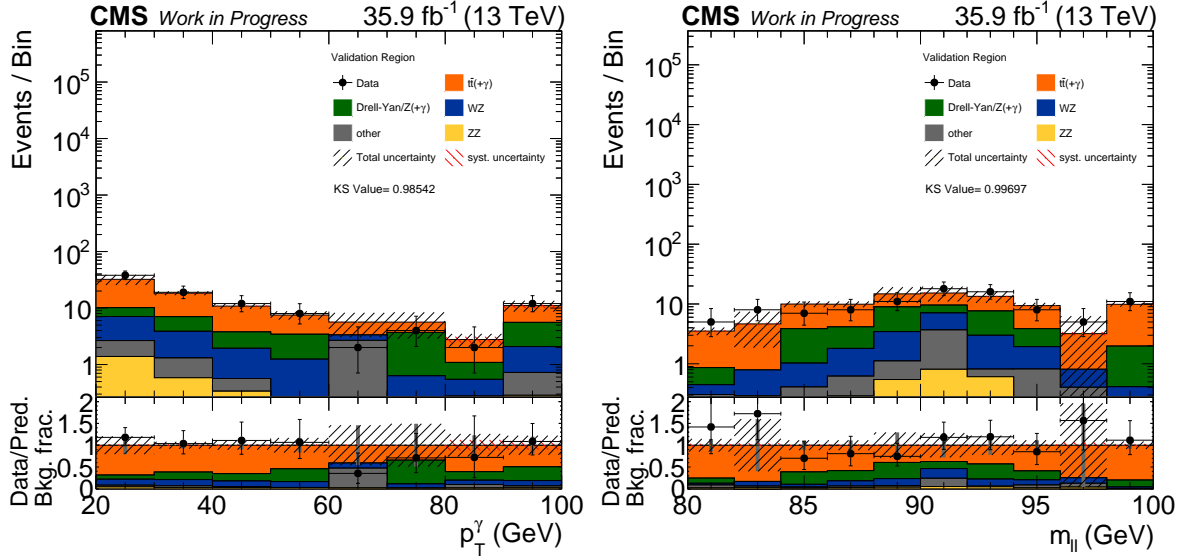


Figure 4.14.: Comparisons between data and rescaled simulation in the VR in the photon p_T and invariant dilepton mass distribution. Below each plot, a ratio between data and prediction is shown. The uncertainty bands correspond to the systematic (red) and total uncertainty (gray). In addition, in the ratio plot the relative composition of the backgrounds is visualized. KS-values for the performed Kolmogorov-Smirnov test are also quoted.

in this bin.

In total, the influence of signal contamination to the final result is rather negligible, because for most of the signal points the contributions to all CRs are very low. In cases where they exceed the level of some percent, their influence will not matter in the final interpretation, since for those low SUSY mass signal points, the expectation for the signal yield in the SR is sufficiently high enough.

4.3. Study of systematic uncertainties

In addition to the statistical uncertainties coming from the background prediction method itself, various systematic effects and their impact on the final prediction need to be evaluated.

4.3.1. Background uncertainties

Sources of systematic uncertainties arise from the measured pileup distribution, which is needed to rescale the simulated samples as explained in Section 3.2, the measurement of the total integrated luminosity, the measurement of the jet energy scale (JES) and the jet energy resolution (JER), that are important for the p_T^{miss} description, the measured trigger efficiencies as discussed in Section 3.6, corrections for a different photon and lepton reconstruction in simulation and data, the PDF used in the MC simulation process, and the factorization scale and renormalization scale.

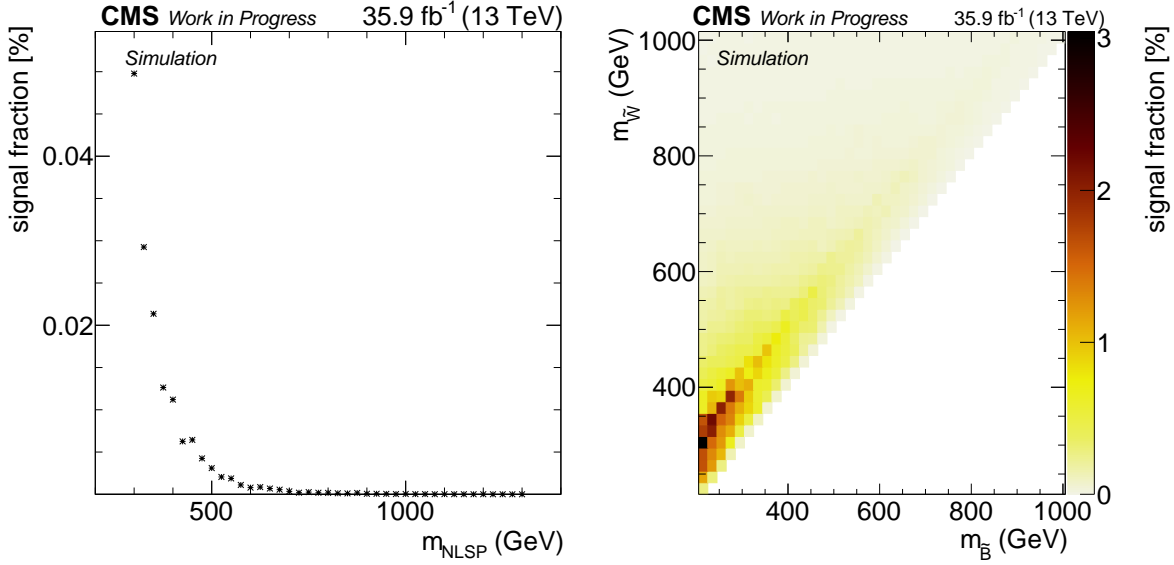


Figure 4.15.: Signal fraction for different signal points of the TChiZG in the DY/Z(γ) CR (left) and the GMSB model in the WZ CR (right).

These measurements and underlying effects all provide systematic uncertainties on the final background prediction. Cross section uncertainties cancel for the four main background contributions due to the applied method, but are relevant for the other minor contributions as a relative uncertainty. They are assumed to be 50% to account for the biggest differences between the measurement and theoretical prediction, and consider the circumstance, that only a special phase space is used in the analysis.

The uncertainty on the luminosity measurement with 2.5% [134] and the uncertainty on the trigger efficiency, that is estimated to be 3% (see Section 3.6), propagate directly as relative uncertainties to the final prediction.

All other uncertainties are uncertainties in the shape, and need to be determined another way. In order to estimate the impact of the JEC and JER, the pileup reweighting, and the lepton and photon identification and reconstruction corrections, the whole background prediction is performed again with the underlying quantities shifted one standard deviation up and down. Hence, two additional predictions for each SR bin are obtained, and half of the difference between those, relative to the nominal prediction, is taken as the systematic uncertainty.

To estimate the effect on the choice of the renormalization scale μ_R and factorization scale μ_F , these two are varied in combinations of the factors 0.5, 1, and 2, and nine new background predictions are obtained. The half of the difference between the two outliers, relative to the nominal prediction, is treated as the systematic uncertainty.

To determine the systematic uncertainty arising from the used PDFs, one hundred different PDF variations are studied, and for each the background prediction method is performed again, thus one hundred different predictions for the SR are obtained. From this distribution of predicted yields, the standard deviation and the mean can be calculated. The standard deviation normalized to the mean is considered as the systematic uncertainty.

Table 4.5.: Systematic uncertainty ranges for all background predictions in the signal region.

	$tt(\gamma)$	DY/Z(γ)	WZ	ZZ	Other
PDF	0.8 – 1.5%	2.6 – 3.3%	0.5 – 0.7%	2.2 – 2.4%	1.1 – 1.2%
Renorm. and fact. scale	3.4 – 7.1%	18.2 – 22.5%	4 – 6%	3.7 – 4.1%	2.1 – 9.3%
JES	4.6 – 6.5%	4.4 – 5%	2.8 – 4.8%	1 – 1.9%	0 – 50.7%
JER	1.6 – 3.1%	0.7 – 16.1%	1 – 1.8%	0.2 – 1.4%	0 – 50.7%
Lepton ID and reconstruction	2.8 – 2.9%	2.2 – 3.4%	3.3%	1.8%	4.2%
Photon ID and reconstruction	0.7 – 0.8%	1.4 – 1.5%	1 – 1.1%	0.9%	0.7 – 1.9%
Luminosity	-	-	-	-	2.5%
Pileup	1.2 – 2%	1 – 5%	0.2 – 2.5%	1.5 – 1.7%	0.1 – 10%
Trigger efficiency	-	-	-	-	3%
Scale factor α_i	4%	0.9%	3.3%	5.7%	-
Cross section	-	-	-	-	50%

Table 4.5 lists ranges for all systematic uncertainties for all backgrounds individually. Besides uncertainties for some backgrounds, such as DY/Z(γ) and the other composed backgrounds, exceed the level of 10%, where statistical fluctuations based on changes of different quantities play an important role, all other systematic uncertainties are of the order of some percent. This reflects the stability and robustness, that was observed in the scale factor determination itself.

4.3.2. Signal uncertainties

Whereas all derivations of systematic uncertainties on the final event yields are covered, further signal uncertainties need to be studied in order to interpret the results statistically in each SUSY model. Most of the signal uncertainty determination methods behave the same as explained above for the backgrounds, but some additional effects need to be considered, and some calculations change, since the detector response in the signal MC simulation was performed using FASTSIM.

For the determination of the pileup uncertainty, a different method was applied. The pileup distribution is split into a low PU (< 20) and a high PU (> 20) region, and the difference in the total signal acceptance was determined. Half of this difference is treated as the systematic uncertainty.

Because the modeling of the p_T^{miss} distribution is very complicated, and in the FASTSIM package only a simplified detector response is parameterized, the difference between generated p_T^{miss} and reconstructed p_T^{miss} is investigated. Thus, the whole analysis is reperformed for the signal, where the reconstructed p_T^{miss} is replaced with the generated one for each event, and the difference in the acceptance is examined. Half of the deviation is taken as the systematic uncertainty.

For the signal simulation no PDF uncertainties are available. In addition, the initial state radiation dependent reweightings mentioned in Section 3.2 introduce systematic effects on the signal yield expectation. Therefore the same method as mentioned above for the identification and reconstruction uncertainties on the background prediction is performed. Ranges for all signal uncertainties including the statistical one are given in Table 4.6 al-

Table 4.6.: Ranges for all the systematic uncertainties for all signal models.

Uncertainty	Range [%]
Statistical	3.2 – 85
Luminosity	2.6
PileUp	< 0.1 – 143
JES	< 0.1 – 62
JER	< 0.1 – 63
Trigger Efficiency	3
Lepton Scale Factor	< 0.1 – 5.6
Photon Scale Factor	1.4 – 1.5
MET/GEN MET	< 0.1 – 293
ISR Reweighting	< 0.1 – 10.5
Scale	0.1 – 10.9

together for all signal models considered in the analysis. Large ranges are observable due to the limited statistics that is available for each signal point. Mainly all other systematic effects are correlated with the statistical uncertainty. This is due to time and resource saving reasons, since a huge amount of different signal points is being generated. In addition, the already low amount of generated signal events becomes much lower, as only leptonic decay branches of the Z boson are considered and this branching fraction is very low. Nevertheless, in most of the relevant signal points the uncertainties do not exceed the level of a few percent.

Chapter 5

Results and interpretation

Contents

5.1. Results	71
5.2. Statistical interpretation	73

Now that all backgrounds are well estimated, the background prediction works fine in the validation region, and all uncertainties are determined, the background prediction can be applied to the SR, $p_{\text{T}}^{\text{miss}} > 150$ GeV and $M_{\text{T}2} > 100$ GeV, and predicted and observed event counts can be compared. An excess or other significant deviations from the prediction would be indicators for BSM physics.

5.1. Results

Signal region binning

In order to perform the counting experiment, a distinct binning in one or multiple variables needs to be applied to the SR. This binning can be optimized considering different criteria, e.g. observation and exclusion power. Since the most sensitive variables are $p_{\text{T}}^{\text{miss}}$ and $M_{\text{T}2}$, different one dimensional and two dimensional binnings are trialed. For individual benchmark points of all three signal models, simplified significances $\frac{s}{s+b}$, where s is the number of signal events and b the number of background events per bin, the binnings are varied. Because the total predicted event count in the SR is of the order of 13 events, special care has to be taken regarding this issue. Albeit many sensitive bins with lower SM prediction and high signal expectation would push expected exclusion limits, this would make reinterpretations and observations difficult due to the high statistical uncertainties of the measured data.

To take into consideration all those aspects, a binning consisting of two bins in the $p_{\text{T}}^{\text{miss}}$

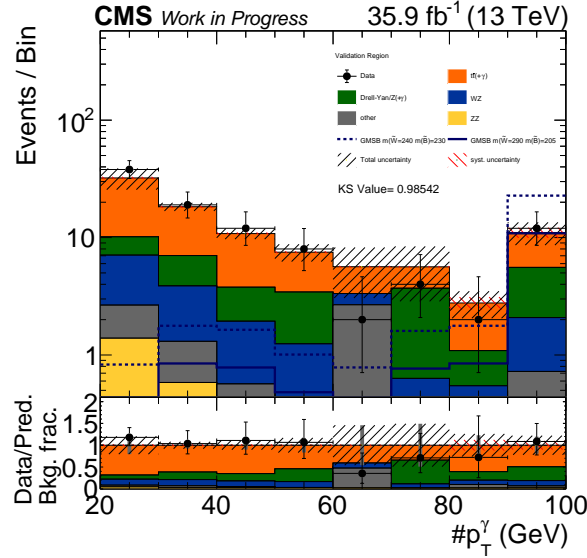


Figure 5.1.: The transverse momentum distribution of the photon in the VR. Signal benchmark points are also added to show the possible sensitivity in the high p_T^γ regime.

distribution are chosen, as already introduced in Section 4.1.2. The first bin starts at 150 GeV and ends at 200 GeV, while the second one is an overflow bin, meaning all events with $p_T^{\text{miss}} > 200$ GeV in the SR are counted in that bin. This binning yields on the one side good exclusion power, because the p_T^{miss} distribution is observed to be more sensitive than the M_{T2} distribution, and on the other side includes an amount of events large enough in each bin, so that the reinterpretation is not restricted by statistical uncertainties. Due to the same reasons, two dimensional binnings are discarded.

Possible influence of signal to the validation region

The SR and the VR are very close to each other in phase space due to the chosen side-band structure of the VR. Thus, some signal events, especially for low SUSY masses, are expected to populate also the VR. The distribution most sensitive to this effect is the p_T^γ distribution of the selected photon, as shown in Figure 5.1. At high p_T^γ ranges (> 80 GeV), a considerable amount of signal events is measurable in the VR. Since the predicted background and observed data are already compared in the VR, and no background prediction is performed here, there is no need to account for this effect like in the other CR in terms of signal contamination.

Hence, the subtraction of this region from the VR, and the addition to the SR as a third search bin would increase the total sensitivity. But, because the number of expected signal events in the two SR bins is already high enough for the relevant signal points, this strategy does not show any improvement in the overall sensitivity, + that is large enough to justify the deterioration in the simplicity of the analysis.

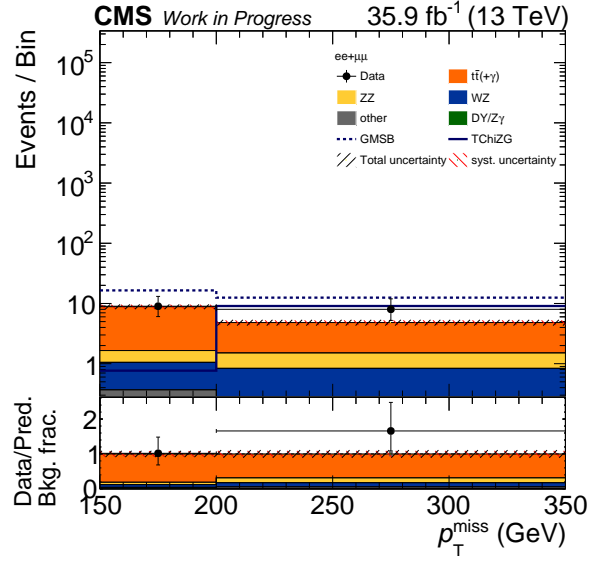


Figure 5.2.: Comparison between final prediction and observation with statistical and systematic uncertainties in the signal region. Two signal expectations for the TChiZG model with $m(NLSP) = 600$ GeV and the GMSB model with $m(\tilde{W}) = 290$ GeV and $m(\tilde{B}) = 205$ GeV are also shown.

5.1.1. Event yields

The final background prediction together with the observed event yield is shown in Figure 5.2. The total background uncertainties are obtained by adding the individual uncertainties quadratically. The statistical uncertainties on the measurement are calculated using 68% confidence intervals of the Poisson distribution with the mean set to the observed yield. To show the effect of a possible signal in the counting experiment, contributions of two example signal points are drawn for comparison. The measured data yields are in good agreement with the predicted background events, thus no evidence for BSM physics is found. The measured excess corresponds to a significance of 1.26σ . The number of background and observed events together with their total uncertainties are given also in Table 5.1.

5.2. Statistical interpretation

No evidence for BSM physics is found, but the results can be interpreted in various SUSY models in terms of exclusion of available model parameter space.

5.2.1. Limit calculation

Upper cross section limits are calculated for signal points in the parameter space of simplified models with both electroweak and strong production, and a consistent GMSB model, as introduced in Section 1.3.2. All limits are calculated using modified frequentist CL_s approach [135–137] with a likelihood test statistics and asymptotic formulae [138] at a con-

Table 5.1.: Observed yields and final predicted background yields with the statistical and systematic uncertainties for each bin and background.

p_T^{miss}	150 – 200 GeV			200 GeV –		
	yield	σ_{stat}	σ_{syst}	yield	σ_{stat}	σ_{syst}
$t\bar{t}(\gamma)$	7.191	0.316	0.664	3.320	0.229	0.395
DY/Z(γ)	0.152	0.060	0.039	0.042	0.024	0.010
WZ	0.684	0.081	0.063	0.579	0.076	0.054
ZZ	0.601	0.019	0.052	0.667	0.020	0.061
Other	0.215	0.215	0.191	0.214	0.214	0.108
Total	8.843	0.396	0.697	4.822	0.324	0.418
Data	9	$^{+4.11}_{-2.94}$	/	8	$^{+3.95}_{-2.76}$	/

fidence level (CL) of 95%. The compatibility of the background only (b) and signal plus background ($s + b$) hypotheses with the results is tested. Therefore, the signal strength modifier μ is introduced, in order to express both hypotheses in a uniform way $\mu s + b$, where $\mu = 0$ yields the background only hypotheses, and $\mu > 0$ corresponds to the $s + b$ hypotheses.

To account for systematic uncertainties, for each signal or background uncertainty a nuisance parameter θ is introduced, and signal and background yield are rewritten as functions of θ : $s(\theta)$ and $b(\theta)$. Different probability density functions (pdf) $p(\tilde{\theta}|\theta)$ are also implemented in the likelihood, to reflect degree of belief in the true value of the nuisance parameter θ , where $\tilde{\theta}$ is the default value of the nuisance parameter. Different pdfs are used to describe the uncertainties, such as the log normal or log uniform distributions. The total likelihood function $\mathcal{L}(\text{data}|\mu, \theta)$ reads

$$\mathcal{L}(\text{data}|\mu, \theta) = \text{Poisson}(\text{data}|\mu \cdots (\theta + b(\theta)) \cdot p(\tilde{\theta}|\theta)). \quad (5.1)$$

Here, data represents the actual experimental observation, and $\text{Poisson}(\text{data}|\mu \cdots (\theta + b(\theta)))$ stands for the probability to observe n_i events in i bins:

$$\prod_i \frac{(\mu s_i + b_i)^{n_i}}{n_i!} e^{-\mu s_i - b_i}. \quad (5.2)$$

A test statistics \tilde{q}_μ is introduced as a likelihood ratio, because according to the Neyman-Pearson Lemma this is the discriminator suited best for the testing of two alternative statistical hypotheses while minimizing the rate of wrongly rejected true hypotheses and accepted false hypotheses:

$$\tilde{q}_\mu = -2 \ln \frac{\mathcal{L}(\text{data}|\mu, \hat{\theta}_\mu)}{\mathcal{L}(\text{data}|\hat{\mu}, \hat{\theta})}, \text{ with } 0 \leq \hat{\mu} \leq \mu. \quad (5.3)$$

Here, $\hat{\theta}_\mu$ refers to the conditional maximum likelihood estimators of θ , given the signal strength μ and the data. The parameters $\hat{\theta}$ and $\hat{\mu}$ correspond to the global maximum of the likelihood. The constraints on $\hat{\mu}$ ensure, that only positive signal rates are considered,

and a one sided confidence interval is guaranteed.

The probability to obtain values of $\hat{\theta}_\mu$ larger than observed in data ($\hat{\theta}_\mu^{obs}$) is given by CL_b for the background only hypothesis and CL_{s+b} for the signal plus background hypothesis. Now the ratio CL_s can be calculated

$$CL_s = \frac{CL_{s+b}}{CL_b}. \quad (5.4)$$

The $(1 - \alpha) = 95\%$ CL upper limit is found by varying μ until $CL_s = \alpha = 0.05$ is reached. The limits on μ can be translated into cross section upper limits by multiplying it with the cross section that was used to determine the expected signal yield.

The whole calculation is performed using the Higgs Combine tool [137], while all systematic uncertainties are treated as fully correlated over all bins and background, except for the statistical uncertainties. Additional expected upper limits are calculated using pseudo-data, that are useful to show the maximum sensitivity of the analysis, since statistical fluctuations are not considered.

5.2.2. Exclusion limits

Three different SUSY models are used to interpret the results of the counting experiment discussed above individually for each masspoint. If the given theoretical cross section exceeds the calculated limit, the points is considered as excluded. In cases of two dimensional parameter scans, exclusion contours can be determined.

Limits on electroweak production of charginos and neutralinos

Two different models are used to interpret the results for EWK SUSY production. For the TChiZG SMS, expected (dashed line) and observed upper limits shown in Figure 5.3 (left) as a function of the NLSP mass parameter. The theoretical cross section together with the uncertainty band is plotted as the blue curve. The error band of the expected limit reflects all uncertainties of the analysis.

This analysis is capable of excluding NLSP masses below 600 GeV in this scenario. Due to the excess of data in the second SR bin, which is the most sensitive one for all signal points of this parameter scan, the observed limit is approximately one standard deviation weaker than the expected limit of 675 GeV.

Upper cross section limits for the two dimensional GMSB model are shown in Figure 5.3 (right) together with the expected limit contour (red) and the observed limit contour (black). The uncertainty band of the expected limit represents all analysis specific uncertainties, while the uncertainty band of the observed limit reflects theoretical cross section uncertainties. The limits are shown in the wino-bino mass plane, where the wino mass corresponds to the $\tilde{\chi}_1^\pm$ and $\tilde{\chi}_2^0$ mass, and the bino mass corresponds to the NLSP $\tilde{\chi}_1^0$ mass, as discussed in Section 1.3.2. The analysis has highest sensitivity in cases where the bino and wino mass differ by around 90 GeV, so that the Z boson production in the decays of the wino is enhanced, as can be seen by the diagonal-like structure in the cross section limit plane. The sensitivity weakens for lower and higher wino masses, since the available energy is split between all decay products. For degenerate bino and wino masses, the

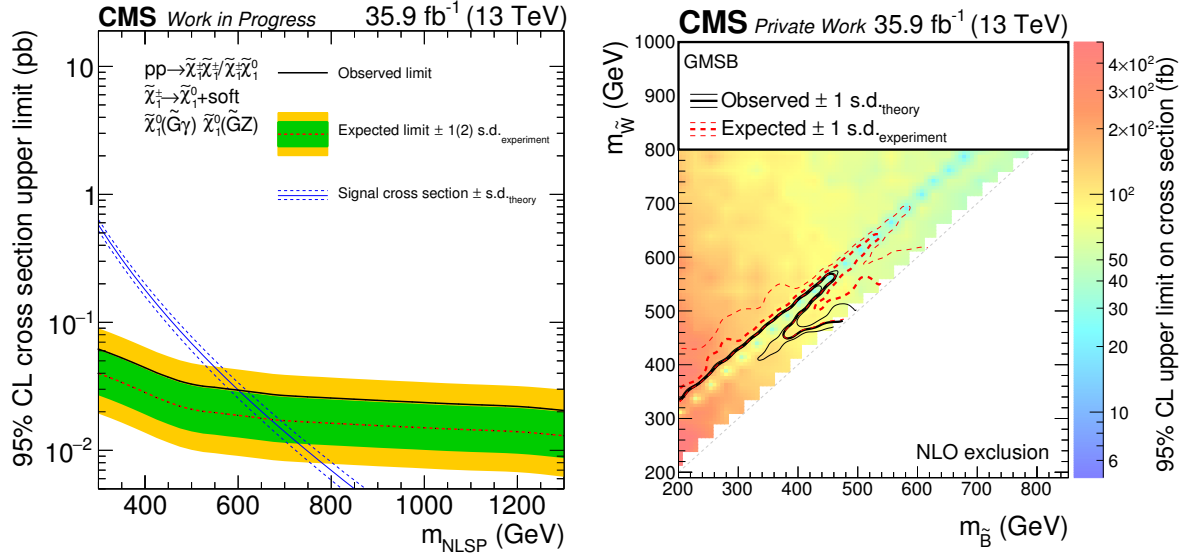


Figure 5.3.: Expected and observed upper limits for the TChiZG electroweak SMS (left) and the full GMSB model (right).

sensitivity increases again, because nearly all energy is transferred into the final decay products, the gravitinos and the selected bosons. Due to the cross section increase for larger bino masses, the sensitivity loses there. In total the analysis can exclude bino and wino masses in a range up to 400 – 500 GeV depending on the wino mass.

The exclusion contours show the same behavior as for the one dimensional exclusion discussed above, due to the overfluctuation in data in the second SR bin. Therefore, the observed limit is weaker than the expected limit.

Limits on strong production of gluinos

In addition to the limits on EWK SUSY production, the results are interpreted in a SMS with gluino pair production. The cross section upper limits are shown in Figure 5.4 in the gluino-NLSP mass plane.

The analysis can exclude gluino masses up to 1.4 TeV, depending on the mass of the NLSP ($\tilde{\chi}_1^0$), and thus the mass splitting between them. For NLSP masses lower than the 150 GeV the sensitivity drops because of the applied M_{T2} threshold of 100 GeV and its poor mass resolution due to the difficulty in the interpretation of p_T^{miss} . With increased $\tilde{\chi}_1^0$ mass the sensitivity rises, since the final state products carry much more energy than for lower $\tilde{\chi}_1^0$ masses. Again, the same effect between expected and observed limit contour is observable.

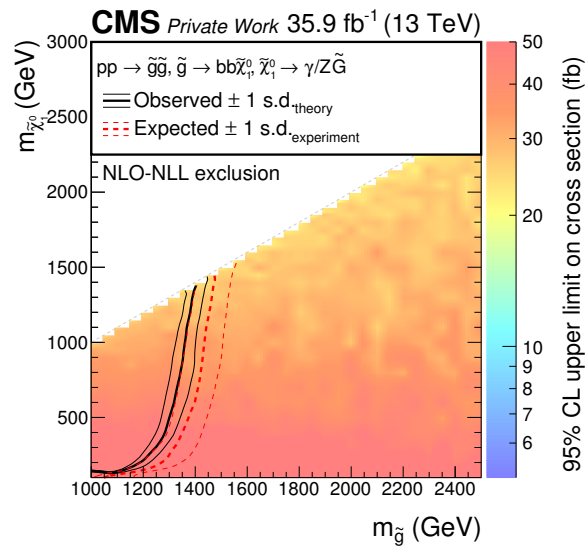


Figure 5.4.: Expected and observed upper limits for the T5bbbbZG SMS with strong production.

Chapter 6	
	Conclusion

Bibliography

- [1] F. Pisano and N. O. Reis, “Natural units, numbers and numerical clusters”, [arXiv:hep-ph/0112097](#).
- [2] A. Pich, “The Standard model of electroweak interactions”, in *The Standard model of electroweak interactions*, pp. 1–49. 2008. [arXiv:0705.4264](#). [1(2007)].
- [3] A. Einstein, “The Foundation of the General Theory of Relativity”, *Annalen Phys.* **49** (1916), no. 7, 769–822, [doi:10.1002/andp.200590044](#), [10.1002/andp.19163540702](#). [65(1916)].
- [4] Particle Data Group Collaboration, “Review of Particle Physics”, *Chin. Phys. C* **40** (2016), no. 10, 100001, [doi:10.1088/1674-1137/40/10/100001](#).
- [5] K. G. Wilson, “Confinement of quarks”, *Phys. Rev. D* **10** (Oct, 1974) 2445–2459, [doi:10.1103/PhysRevD.10.2445](#).
- [6] LHCb Collaboration, “Evidence for exotic hadron contributions to $\Lambda_b^0 \rightarrow j/\psi p \pi^-$ decays”, *Phys. Rev. Lett.* **117** (Aug, 2016) 082003, [doi:10.1103/PhysRevLett.117.082003](#).
- [7] S. Weinberg, “Effects of a neutral intermediate boson in semileptonic processes”, *Phys. Rev. D* **5** (Mar, 1972) 1412–1417, [doi:10.1103/PhysRevD.5.1412](#).
- [8] S. Weinberg, “A model of leptons”, *Phys. Rev. Lett.* **19** (Nov, 1967) 1264–1266, [doi:10.1103/PhysRevLett.19.1264](#).
- [9] A. Salam and J. Ward, “Electromagnetic and weak interactions”, *Physics Letters* **13** (1964), no. 2, 168 – 171, [doi:https://doi.org/10.1016/0031-9163\(64\)90711-5](#).
- [10] S. L. Glashow, “Partial-symmetries of weak interactions”, *Nuclear Physics* **22** (1961), no. 4, 579 – 588, [doi:https://doi.org/10.1016/0029-5582\(61\)90469-2](#).

- [11] C. S. Wu et al., “Experimental test of parity conservation in beta decay”, *Phys. Rev.* **105** (Feb, 1957) 1413–1415, doi:10.1103/PhysRev.105.1413.
- [12] M. Goldhaber, L. Grodzins, and A. W. Sunyar, “Helicity of neutrinos”, *Phys. Rev.* **109** (Feb, 1958) 1015–1017, doi:10.1103/PhysRev.109.1015.
- [13] P. W. Higgs, “Broken symmetries and the masses of gauge bosons”, *Phys. Rev. Lett.* **13** (Oct, 1964) 508–509, doi:10.1103/PhysRevLett.13.508.
- [14] F. Englert and R. Brout, “Broken symmetry and the mass of gauge vector mesons”, *Phys. Rev. Lett.* **13** (Aug, 1964) 321–323, doi:10.1103/PhysRevLett.13.321.
- [15] G. S. Guralnik, C. R. Hagen, and T. W. B. Kibble, “Global conservation laws and massless particles”, *Phys. Rev. Lett.* **13** (Nov, 1964) 585–587, doi:10.1103/PhysRevLett.13.585.
- [16] CMS Collaboration, “Observation of a new boson at a mass of 125 GeV with the CMS experiment at the LHC”, *Phys. Lett. B* **716** (2012) 30–61, doi:10.1016/j.physletb.2012.08.021, arXiv:1207.7235.
- [17] ATLAS Collaboration, “Observation of a new particle in the search for the Standard Model Higgs boson with the ATLAS detector at the LHC”, *Phys. Lett. B* **716** (2012) 1–29, doi:10.1016/j.physletb.2012.08.020, arXiv:1207.7214.
- [18] CMS Collaboration, “Precise determination of the mass of the Higgs boson and tests of compatibility of its couplings with the standard model predictions using proton collisions at 7 and 8 TeV”, *Eur. Phys. J.* **C75** (2015), no. 5, 212, doi:10.1140/epjc/s10052-015-3351-7, arXiv:1412.8662.
- [19] CMS Collaboration, “Observation of $t\bar{t}h$ production”, *Phys. Rev. Lett.* **120** (Jun, 2018) 231801, doi:10.1103/PhysRevLett.120.231801.
- [20] CMS Collaboration, “Observation of the Higgs boson decay to a pair of τ leptons with the CMS detector”, *Phys. Lett. B* **779** (2018) 283–316, doi:10.1016/j.physletb.2018.02.004, arXiv:1708.00373.
- [21] CMS Collaboration, “Observation of Higgs boson decay to bottom quarks”, *Phys. Rev. Lett.* (2018) arXiv:1808.08242.
- [22] Planck Collaboration, “Planck 2015 results. XIII. Cosmological parameters”, *Astron. Astrophys.* **594** (2016) A13, doi:10.1051/0004-6361/201525830, arXiv:1502.01589.
- [23] R. Massey, T. Kitching, and J. Richard, “The dark matter of gravitational lensing”, *Rept. Prog. Phys.* **73** (2010) 086901, doi:10.1088/0034-4885/73/8/086901, arXiv:1001.1739.
- [24] M. Persic, P. Salucci, and F. Stel, “The Universal rotation curve of spiral galaxies: 1. The Dark matter connection”, *Mon. Not. Roy. Astron. Soc.* **281** (1996) 27, doi:10.1093/mnras/281.1.27, 10.1093/mnras/278.1.27,

- arXiv:astro-ph/9506004.
- [25] L. Canetti, M. Drewes, and M. Shaposhnikov, “Matter and Antimatter in the Universe”, *New J. Phys.* **14** (2012) 095012, doi:10.1088/1367-2630/14/9/095012, arXiv:1204.4186.
 - [26] G. R. Farrar and M. E. Shaposhnikov, “Baryon asymmetry of the universe in the minimal Standard Model”, *Phys. Rev. Lett.* **70** (1993) 2833–2836, doi:10.1103/PhysRevLett.71.210.2, 10.1103/PhysRevLett.70.2833, arXiv:hep-ph/9305274. [Erratum: *Phys. Rev. Lett.* 71,210(1993)].
 - [27] A. D. Sakharov, “Violation of CP Invariance, C asymmetry, and baryon asymmetry of the universe”, *Pisma Zh. Eksp. Teor. Fiz.* **5** (1967) 32–35, doi:10.1070/PU1991v034n05ABEH002497. [*Usp. Fiz. Nauk* 161,no.5,61(1991)].
 - [28] M. C. Gonzalez-Garcia and Y. Nir, “Neutrino masses and mixing: Evidence and implications”, *Rev. Mod. Phys.* **75** (2003) 345–402, doi:10.1103/RevModPhys.75.345, arXiv:hep-ph/0202058.
 - [29] S. P. Martin, “A Supersymmetry primer”, doi:10.1142/9789812839657_0001, 10.1142/9789814307505_0001, arXiv:hep-ph/9709356. [*Adv. Ser. Direct. High Energy Phys.* 18,1(1998)].
 - [30] J. Wess and B. Zumino, “Supergauge Transformations in Four-Dimensions”, *Nucl. Phys. B* **70** (1974) 39–50, doi:10.1016/0550-3213(74)90355-1. [24(1974)].
 - [31] S. Coleman and J. Mandula, “All possible symmetries of the s matrix”, *Phys. Rev.* **159** (Jul, 1967) 1251–1256, doi:10.1103/PhysRev.159.1251.
 - [32] R. Haag, J. T. Łopuszański, and M. Sohnius, “All possible generators of supersymmetries of the s -matrix”, *Nuclear Physics B* **88** (1975), no. 2, 257 – 274, doi:https://doi.org/10.1016/0550-3213(75)90279-5.
 - [33] S. P. de Alwis, “On Anomaly Mediated SUSY Breaking”, *Phys. Rev. D* **77** (2008) 105020, doi:10.1103/PhysRevD.77.105020, arXiv:0801.0578.
 - [34] SNO Collaboration, “Constraints on nucleon decay via ‘invisible’ modes from the Sudbury Neutrino Observatory”, *Phys. Rev. Lett.* **92** (2004) 102004, doi:10.1103/PhysRevLett.92.102004, arXiv:hep-ex/0310030.
 - [35] P. Meade, N. Seiberg, and D. Shih, “General Gauge Mediation”, *Prog. Theor. Phys. Suppl.* **177** (2009) 143–158, doi:10.1143/PTPS.177.143, arXiv:0801.3278.
 - [36] P. Meade, M. Reece, and D. Shih, “Prompt Decays of General Neutralino NLSPs at the Tevatron”, *JHEP* **05** (2010) 105, doi:10.1007/JHEP05(2010)105, arXiv:0911.4130.
 - [37] S. Dimopoulos, S. D. Thomas, and J. D. Wells, “Sparticle spectroscopy and electroweak symmetry breaking with gauge mediated supersymmetry breaking”,

- Nucl. Phys. B* **488** (1997) 39–91, doi:10.1016/S0550-3213(97)00030-8, arXiv:hep-ph/9609434.
- [38] S. Ambrosanio et al., “Search for supersymmetry with a light gravitino at the Fermilab Tevatron and CERN LEP colliders”, *Phys. Rev. D* **54** (1996) 5395–5411, doi:10.1103/PhysRevD.54.5395, arXiv:hep-ph/9605398.
- [39] D. A. and Nima Arkani-Hamed et al., “Simplified models for lhc new physics searches”, *Journal of Physics G: Nuclear and Particle Physics* **39** (2012), no. 10, 105005.
- [40] CMS Collaboration, “Interpretation of searches for supersymmetry with simplified models”, *Phys. Rev. D* **88** (Sep, 2013) 052017, doi:10.1103/PhysRevD.88.052017.
- [41] S. Ask, “A Review of the supersymmetry searches at LEP”, in *38th Rencontres de Moriond on Electroweak Interactions and Unified Theories Les Arcs, France, March 15-22, 2003*. 2003. arXiv:hep-ex/0305007.
- [42] X. P. Bueso, “Supersymmetry Searches at the Tevatron and the LHC Collider Experiments”, in *Proceedings, 31st International Conference on Physics in collisions (PIC 2011): Vancouver, Canada, August 28-September 1, 2011*. 2011. arXiv:1112.1723.
- [43] C. Autermann, “Experimental status of supersymmetry after the LHC Run-I”, *Prog. Part. Nucl. Phys.* **90** (2016) 125–155, doi:10.1016/j.ppnp.2016.06.001, arXiv:1609.01686.
- [44] CMS Collaboration, “Search for Physics Beyond the Standard Model in Events with Two Leptons, Jets, and Missing Transverse Momentum in pp Collisions at $\sqrt{s} = 8$ TeV”, *JHEP* **04** (2015) 124, doi:10.1007/JHEP04(2015)124, arXiv:1502.06031.
- [45] LHCb, CMS Collaboration, “Observation of the rare $B_s^0 \rightarrow \mu^+ \mu^-$ decay from the combined analysis of CMS and LHCb data”, *Nature* **522** (2015) 68–72, doi:10.1038/nature14474, arXiv:1411.4413.
- [46] CMS Collaboration, “Search for Physics Beyond the Standard Model in Events with High-Momentum Higgs Bosons and Missing Transverse Momentum in Proton-Proton Collisions at 13 TeV”, *Phys. Rev. Lett.* **120** (2018), no. 24, 241801, doi:10.1103/PhysRevLett.120.241801, arXiv:1712.08501.
- [47] CMS Collaboration, “Search for new phenomena in final states with two opposite-charge, same-flavor leptons, jets, and missing transverse momentum in pp collisions at $\sqrt{s} = 13$ TeV”, *JHEP* **03** (2018) 076, doi:10.1007/s13130-018-7845-2, 10.1007/JHEP03(2018)076, arXiv:1709.08908.
- [48] CMS Collaboration, “Search for top squarks and dark matter particles in

- opposite-charge dilepton final states at $\sqrt{s} = 13$ TeV”, *Phys. Rev. D* **97** (2018), no. 3, 032009, doi:10.1103/PhysRevD.97.032009, arXiv:1711.00752.
- [49] CMS Collaboration, “Search for electroweak production of charginos and neutralinos in multilepton final states in proton-proton collisions at $\sqrt{s} = 13$ TeV”, *JHEP* **03** (2018) 166, doi:10.1007/JHEP03(2018)166, arXiv:1709.05406.
- [50] CMS Collaboration, “The CMS experiment at the CERN LHC”, *Journal of Instrumentation* **3** (2008), no. 08, S08004.
- [51] CMS Collaboration, “CMS Supersymmetry Physics Results”. Accessed: 2018-09-25. <https://twiki.cern.ch/twiki/bin/view/CMSPublic/PhysicsResultsSUS>.
- [52] CMS Collaboration, “Search for gauge-mediated supersymmetry in events with at least one photon and missing transverse momentum in pp collisions at $\sqrt{s} = 13$ TeV”, *Phys. Lett. B* **780** (2018) 118–143, doi:10.1016/j.physletb.2018.02.045, arXiv:1711.08008.
- [53] CMS Collaboration, “Search for supersymmetry using events with a photon, a lepton, and missing transverse momentum in pp collisions at $\sqrt{s} = 13$ TeV”, Technical Report CMS-PAS-SUS-17-012, CERN, Geneva, 2018.
- [54] CMS Collaboration, “Search for supersymmetry in events with at least one photon, missing transverse momentum, and large transverse event activity in proton-proton collisions at $\sqrt{s} = 13$ TeV”, *JHEP* **12** (2017) 142, doi:10.1007/JHEP12(2017)142, arXiv:1707.06193.
- [55] CMS Collaboration, “Search for supersymmetry in events with a photon, jets, and missing transverse momentum in proton-proton collisions at 13 TeV”, Technical Report CMS-PAS-SUS-18-002, CERN, Geneva, 2018.
- [56] ATLAS Collaboration, “Search for supersymmetry in events with four or more leptons in $\sqrt{s} = 13$ TeV pp collisions with ATLAS”, *Phys. Rev. D* **98** (2018), no. 3, 032009, doi:10.1103/PhysRevD.98.032009, arXiv:1804.03602.
- [57] ATLAS Collaboration, “Search for pair production of higgsinos in final states with at least three b -tagged jets in $\sqrt{s} = 13$ TeV pp collisions using the ATLAS detector”, *Phys. Rev.* (2018) arXiv:1806.04030.
- [58] ATLAS Collaboration, “Search for photonic signatures of gauge-mediated supersymmetry in 13 TeV pp collisions with the ATLAS detector”, *Phys. Rev. D* **97** (2018), no. 9, 092006, doi:10.1103/PhysRevD.97.092006, arXiv:1802.03158.
- [59] J. L. Feng, “Naturalness and the Status of Supersymmetry”, *Ann. Rev. Nucl. Part. Sci.* **63** (2013) 351–382, doi:10.1146/annurev-nucl-102010-130447, arXiv:1302.6587.
- [60] L. R. F. Castillo, “The large hadron collider”, in *The Search and Discovery of the Higgs Boson*, 2053–2571, pp. 3–1 to 3–9. Morgan Claypool Publishers, 2015. doi:10.1088/978-1-6817-4078-2ch3.

- [61] L. Evans and P. Bryant, “Lhc machine”, *Journal of Instrumentation* **3** (2008), no. 08, S08001.
- [62] G. Bachy et al., “The LEP collider”, *Part. Accel.* **26** (1990) 19–32.
- [63] ALICE Collaboration, “The ALICE experiment at the CERN LHC”, *Journal of Instrumentation* **3** (2008), no. 08, S08002.
- [64] ATLAS Collaboration, “The ATLAS Experiment at the CERN Large Hadron Collider”, *Journal of Instrumentation* **3** (2008), no. 08, S08003.
- [65] LHCb Collaboration, “The LHCb Detector at the LHC”, *Journal of Instrumentation* **3** (2008), no. 08, S08005.
- [66] E. Mobs, “The CERN accelerator complex - August 2018”, Aug, 2018. General Photo, Modified. <http://cds.cern.ch/record/2636343>.
- [67] W. Herr and B. Muratori, “Concept of luminosity”, in *Intermediate accelerator physics. Proceedings, CERN Accelerator School, Zeuthen, Germany, September 15-26, 2003*, pp. 361–377. 2003.
- [68] CMS Collaboration, “Public CMS data quality information”. Accessed: 2018-09-25. https://twiki.cern.ch/twiki/bin/view/CMSPublic/DataQuality#Dataset_For_Morion17_Conference.
- [69] CMS Collaboration, “CMS Physics: Technical Design Report Volume 1: Detector Performance and Software”. Technical Design Report CMS. CERN, Geneva, 2006.
- [70] CMS Collaboration, “Description and performance of track and primary-vertex reconstruction with the CMS tracker”, *JINST* **9** (2014), no. 10, P10009, doi:10.1088/1748-0221/9/10/P10009, arXiv:1405.6569.
- [71] CMS Collaboration, “The CMS ECAL performance with examples”, Technical Report CMS-CR-2013-430, CERN, Geneva, Nov, 2013.
- [72] CMS Collaboration, “Performance and operation of the CMS electromagnetic calorimeter”, *Journal of Instrumentation* **5** (2010), no. 03, T03010.
- [73] CMS Collaboration, “Performance of CMS muon reconstruction in pp collision events at $\sqrt{s} = 7$ TeV”, *JINST* **7** (2012) P10002, doi:10.1088/1748-0221/7/10/P10002, arXiv:1206.4071.
- [74] CMS Collaboration, “The CMS trigger system”, *Journal of Instrumentation* **12** (2017), no. 01, P01020.
- [75] CMS Collaboration, “The CMS trigger in Run 2”, Technical Report CMS-CR-2017-340, CERN, Geneva, Oct, 2017.
- [76] CMS Collaboration, “Mini-AOD: A New Analysis Data Format for CMS”, *J. Phys. Conf. Ser.* **664** (2015), no. 7, 072052, doi:10.1088/1742-6596/664/7/072052, arXiv:1702.04685.

- [77] CMS Collaboration, “CMSSW Application Framework”. Accessed: 2018-10-01. <https://twiki.cern.ch/twiki/bin/view/CMSPublic/WorkBookCMSSWFramework>.
- [78] D. Spigaet al., “The cms remote analysis builder (crab)”, in *Proceedings of the 14th International Conference on High Performance Computing, HiPC’07*, pp. 580–586. Springer-Verlag, Berlin, Heidelberg, 2007.
- [79] I. Bird, “Computing for the large hadron collider”, *Annual Review of Nuclear and Particle Science* **61** (2011), no. 1, 99–118, doi:[10.1146/annurev-nucl-102010-130059](https://doi.org/10.1146/annurev-nucl-102010-130059), arXiv:<https://doi.org/10.1146/annurev-nucl-102010-130059>.
- [80] R. Brun and F. Rademakers, “Root - an object oriented data analysis framework”, *Nuclear Instruments and Methods in Physics Research Section A: Accelerators, Spectrometers, Detectors and Associated Equipment* **389** (1997), no. 1, 81 – 86, doi:[https://doi.org/10.1016/S0168-9002\(97\)00048-X](https://doi.org/10.1016/S0168-9002(97)00048-X). New Computing Techniques in Physics Research V.
- [81] R. Placakyte, “Parton Distribution Functions”, in *Proceedings, 31st International Conference on Physics in collisions (PIC 2011): Vancouver, Canada, August 28-September 1, 2011*. 2011. arXiv:1111.5452.
- [82] A. Afaqet al., “The cms dataset bookkeeping service”, *Journal of Physics: Conference Series* **119** (2008), no. 7, 072001.
- [83] J. Alwall et al., “The automated computation of tree-level and next-to-leading order differential cross sections, and their matching to parton shower simulations”, *JHEP* **07** (2014) 079, doi:[10.1007/JHEP07\(2014\)079](https://doi.org/10.1007/JHEP07(2014)079), arXiv:1405.0301.
- [84] J. Alwall et al., “Comparative study of various algorithms for the merging of parton showers and matrix elements in hadronic collisions”, *Eur. Phys. J. C* **53** (2008) 473–500, doi:[10.1140/epjc/s10052-007-0490-5](https://doi.org/10.1140/epjc/s10052-007-0490-5), arXiv:0706.2569.
- [85] J. Alwall et al., “MadGraph 5 : Going Beyond”, *JHEP* **06** (2011) 128, doi:[10.1007/JHEP06\(2011\)128](https://doi.org/10.1007/JHEP06(2011)128), arXiv:1106.0522.
- [86] R. Frederix and S. Frixione, “Merging meets matching in MC@NLO”, *JHEP* **12** (2012) 061, doi:[10.1007/JHEP12\(2012\)061](https://doi.org/10.1007/JHEP12(2012)061), arXiv:1209.6215.
- [87] T. Sjostrand, S. Mrenna, and P. Z. Skands, “PYTHIA 6.4 Physics and Manual”, *JHEP* **05** (2006) 026, doi:[10.1088/1126-6708/2006/05/026](https://doi.org/10.1088/1126-6708/2006/05/026), arXiv:hep-ph/0603175.
- [88] S. Frixione, P. Nason, and C. Oleari, “Matching NLO QCD computations with Parton Shower simulations: the POWHEG method”, *JHEP* **11** (2007) 070, doi:[10.1088/1126-6708/2007/11/070](https://doi.org/10.1088/1126-6708/2007/11/070), arXiv:0709.2092.
- [89] S. Alioli, P. Nason, C. Oleari, and E. Re, “A general framework for implementing NLO calculations in shower Monte Carlo programs: the POWHEG BOX”, *JHEP* **06** (2010) 043, doi:[10.1007/JHEP06\(2010\)043](https://doi.org/10.1007/JHEP06(2010)043), arXiv:1002.2581.

- [90] CMS Collaboration, “Event generator tunes obtained from underlying event and multiparton scattering measurements”, *Eur. Phys. J. C* **76** (2016), no. 3, 155, doi:10.1140/epjc/s10052-016-3988-x, arXiv:1512.00815.
- [91] NNPDF Collaboration, “Parton distributions for the LHC Run II”, *JHEP* **04** (2015) 040, doi:10.1007/JHEP04(2015)040, arXiv:1410.8849.
- [92] S. Agostinelli et al., “Geant4 - a simulation toolkit”, *Nuclear Instruments and Methods in Physics Research Section A: Accelerators, Spectrometers, Detectors and Associated Equipment* **506** (2003), no. 3, 250 – 303, doi:https://doi.org/10.1016/S0168-9002(03)01368-8.
- [93] A. Giammanco, “The fast simulation of the cms experiment”, *Journal of Physics: Conference Series* **513** (2014), no. 2, 022012.
- [94] CMS Collaboration, “Recent Developments in CMS Fast Simulation”, *PoS ICHEP2016* (2016) 181, doi:10.22323/1.282.0181, arXiv:1701.03850.
- [95] J. Alwall et al., “The automated computation of tree-level and next-to-leading order differential cross sections, and their matching to parton shower simulations”, *JHEP* **07** (2014) 079, doi:10.1007/JHEP07(2014)079, arXiv:1405.0301.
- [96] M. Czakon and A. Mitov, “Top++: A Program for the Calculation of the Top-Pair Cross-Section at Hadron Colliders”, *Comput. Phys. Commun.* **185** (2014) 2930, doi:10.1016/j.cpc.2014.06.021, arXiv:1112.5675.
- [97] M. Grazzini, S. Kallweit, D. Rathlev, and M. Wiesemann, “ $W^\pm Z$ production at the LHC: fiducial cross sections and distributions in NNLO QCD”, *JHEP* **05** (2017) 139, doi:10.1007/JHEP05(2017)139, arXiv:1703.09065.
- [98] F. Cascioli et al., “ZZ production at hadron colliders in NNLO QCD”, *Phys. Lett. B* **735** (2014) 311–313, doi:10.1016/j.physletb.2014.06.056, arXiv:1405.2219.
- [99] F. Caola, K. Melnikov, R. R{ontsch, and L. Tancredi, “QCD corrections to ZZ production in gluon fusion at the LHC”, *Phys. Rev. D* **92** (2015), no. 9, 094028, doi:10.1103/PhysRevD.92.094028, arXiv:1509.06734.
- [100] J. M. Campbell, R. K. Ellis, M. Czakon, and S. Kirchner, “Two loop correction to interference in $gg \rightarrow ZZ$ ”, *JHEP* **08** (2016) 011, doi:10.1007/JHEP08(2016)011, arXiv:1605.01380.
- [101] T. Gehrmann et al., “ W^+W^- Production at Hadron Colliders in Next to Next to Leading Order QCD”, *Phys. Rev. Lett.* **113** (2014), no. 21, 212001, doi:10.1103/PhysRevLett.113.212001, arXiv:1408.5243.
- [102] M. Grazzini, S. Kallweit, and D. Rathlev, “ZZ production at the LHC: fiducial cross sections and distributions in NNLO QCD”, *Phys. Lett. B* **750** (2015) 407–410, doi:10.1016/j.physletb.2015.09.055, arXiv:1507.06257.

- [103] M. Grazzini, S. Kallweit, D. Rathlev, and M. Wiesemann, “ $W^\pm Z$ production at hadron colliders in NNLO QCD”, *Phys. Lett. B* **761** (2016) 179–183, doi:10.1016/j.physletb.2016.08.017, arXiv:1604.08576.
- [104] W. Beenakker, R. Hopker, M. Spira, and P. M. Zerwas, “Squark and gluino production at hadron colliders”, *Nucl. Phys. B* **492** (1997) 51–103, doi:10.1016/S0550-3213(97)80027-2, arXiv:hep-ph/9610490.
- [105] A. Kulesza and L. Motyka, “Threshold resummation for squark-antisquark and gluino-pair production at the LHC”, *Phys. Rev. Lett.* **102** (2009) 111802, doi:10.1103/PhysRevLett.102.111802, arXiv:0807.2405.
- [106] A. Kulesza and L. Motyka, “Soft gluon resummation for the production of gluino-gluino and squark-antisquark pairs at the LHC”, *Phys. Rev. D* **80** (2009) 095004, doi:10.1103/PhysRevD.80.095004, arXiv:0905.4749.
- [107] W. Beenakker et al., “Soft-gluon resummation for squark and gluino hadroproduction”, *JHEP* **12** (2009) 041, doi:10.1088/1126-6708/2009/12/041, arXiv:0909.4418.
- [108] W. Beenakker et al., “Squark and Gluino Hadroproduction”, *Int. J. Mod. Phys. A* **26** (2011) 2637–2664, doi:10.1142/S0217751X11053560, arXiv:1105.1110.
- [109] C. Borschensky et al., “Squark and gluino production cross sections in pp collisions at $\sqrt{s} = 13, 14, 33$ and 100 TeV”, *Eur. Phys. J. C* **74** (2014), no. 12, 3174, doi:10.1140/epjc/s10052-014-3174-y, arXiv:1407.5066.
- [110] W. Beenakker et al., “The Production of charginos / neutralinos and sleptons at hadron colliders”, *Phys. Rev. Lett.* **83** (1999) 3780–3783, doi:10.1103/PhysRevLett.100.029901, 10.1103/PhysRevLett.83.3780, arXiv:hep-ph/9906298. [Erratum: *Phys. Rev. Lett.*100,029901(2008)].
- [111] B. Fuks, M. Klasen, D. R. Lamprea, and M. Rothering, “Gaugino production in proton-proton collisions at a center-of-mass energy of 8 TeV”, *JHEP* **10** (2012) 081, doi:10.1007/JHEP10(2012)081, arXiv:1207.2159.
- [112] B. Fuks, M. Klasen, D. R. Lamprea, and M. Rothering, “Precision predictions for electroweak superpartner production at hadron colliders with Resummino”, *Eur. Phys. J. C* **73** (2013) 2480, doi:10.1140/epjc/s10052-013-2480-0, arXiv:1304.0790.
- [113] CMS Collaboration, “Search for top-squark pair production in the single-lepton final state in pp collisions at $\sqrt{s} = 8$ TeV”, *Eur. Phys. J. C* **73** (2013), no. 12, 2677, doi:10.1140/epjc/s10052-013-2677-2, arXiv:1308.1586.
- [114] CMS Collaboration, “Measurement of the differential cross section for $t\bar{t}$ production in the dilepton final state at $\sqrt{s} = 13$ TeV”, Technical Report CMS-PAS-TOP-16-011, CERN, Geneva, 2016.
- [115] CMS Collaboration, “Measurement of differential cross sections for top quark pair

- production using the lepton+jets final state in proton-proton collisions at 13 TeV”, *Phys. Rev. D* **95** (2017), no. 9, 092001, doi:10.1103/PhysRevD.95.092001, arXiv:1610.04191.
- [116] CMS Collaboration, “Measurement of the differential cross section for top quark pair production in pp collisions at $\sqrt{s} = 8$ TeV”, *Eur. Phys. J. C* **75** (2015), no. 11, 542, doi:10.1140/epjc/s10052-015-3709-x, arXiv:1505.04480.
- [117] CMS Collaboration, “Measurement of the $t\bar{t}$ production cross section in the all-jets final state in pp collisions at $\sqrt{s} = 8$ TeV”, *Eur. Phys. J. C* **76** (2016), no. 3, 128, doi:10.1140/epjc/s10052-016-3956-5, arXiv:1509.06076.
- [118] CMS Collaboration, “Particle-flow reconstruction and global event description with the CMS detector”, *JINST* **12** (2017), no. 10, P10003, doi:10.1088/1748-0221/12/10/P10003, arXiv:1706.04965.
- [119] W. Adam, B. Mangano, T. Speer, and T. Todorov, “Track Reconstruction in the CMS tracker”, Technical Report CMS-NOTE-2006-041, CERN, Geneva, Dec, 2006.
- [120] T. Speer et al., “Vertex Fitting in the CMS Tracker”, Technical Report CMS-NOTE-2006-032, CERN, Geneva, Feb, 2006.
- [121] A. M. Sirunyan et al., “Performance of the CMS muon detector and muon reconstruction with proton-proton collisions at $\sqrt{s} = 13$ TeV”,.
- [122] CMS Collaboration, “Cut Based Electron ID for Run 2”. Accessed: 2018-10-08. <https://twiki.cern.ch/twiki/bin/view/CMS/CutBasedElectronIdentificationRun2?rev=59>.
- [123] CMS Collaboration, “Cut Based Photon ID for Run 2”. Accessed: 2018-10-09. <https://twiki.cern.ch/twiki/bin/view/CMS/CutBasedPhotonIdentificationRun2?rev=46>.
- [124] M. Cacciari, G. P. Salam, and G. Soyez, “The anti- k_t jet clustering algorithm”, *JHEP* **04** (2008) 063, doi:10.1088/1126-6708/2008/04/063, arXiv:0802.1189.
- [125] M. Cacciari, G. P. Salam, and G. Soyez, “FastJet User Manual”, *Eur. Phys. J. C* **72** (2012) 1896, doi:10.1140/epjc/s10052-012-1896-2, arXiv:1111.6097.
- [126] M. Cacciari and G. P. Salam, “Dispelling the N^3 myth for the k_t jet-finder”, *Phys. Lett. B* **641** (2006) 57–61, doi:10.1016/j.physletb.2006.08.037, arXiv:hep-ph/0512210.
- [127] CMS Collaboration, “Jet energy scale and resolution in the CMS experiment in pp collisions at 8 TeV”, *JINST* **12** (2017), no. 02, P02014, doi:10.1088/1748-0221/12/02/P02014, arXiv:1607.03663.
- [128] CMS Collaboration, “Jet Identification for the 13 TeV data Run2016”. Accessed: 2018-10-09. <https://twiki.cern.ch/twiki/bin/view/CMS/JetID13TeVRun2016?rev=11>.

- [129] A. Barr, C. Lester, and P. Stephens, “m(T2): The Truth behind the glamour”, *J. Phys. G* **29** (2003) 2343–2363, doi:10.1088/0954-3899/29/10/304, arXiv:hep-ph/0304226.
- [130] C. G. Lester and D. J. Summers, “Measuring masses of semiinvisibly decaying particles pair produced at hadron colliders”, *Phys. Lett. B* **463** (1999) 99–103, doi:10.1016/S0370-2693(99)00945-4, arXiv:hep-ph/9906349.
- [131] CMS Collaboration, “MET Filter Recommendations for Run II”. Accessed: 2018-10-10. <https://twiki.cern.ch/twiki/bin/view/CMS/MissingETOptionalFiltersRun2?rev=119>.
- [132] C. J. Clopper and E. S. Pearson, “The use of confidence or fiducial limits illustrated in the case of the binomial”, *Biometrika* **26** (1934), no. 4, 404–413.
- [133] “Kolmogorov–Smirnov Test”, pp. 283–287. Springer New York, New York, NY, 2008. doi:10.1007/978-0-387-32833-1_214.
- [134] CMS Collaboration, “CMS Luminosity Measurements for the 2016 Data Taking Period”, Technical Report CMS-PAS-LUM-17-001, CERN, Geneva, 2017.
- [135] T. Junk, “Confidence level computation for combining searches with small statistics”, *Nucl. Instrum. Meth. A* **434** (1999) 435–443, doi:10.1016/S0168-9002(99)00498-2, arXiv:hep-ex/9902006.
- [136] A. L. Read, “Presentation of search results: the cl_s technique”, *Journal of Physics G: Nuclear and Particle Physics* **28** (2002), no. 10, 2693.
- [137] The ATLAS Collaboration, The CMS Collaboration, The LHC Higgs Combination Group Collaboration, “Procedure for the LHC Higgs boson search combination in Summer 2011”, Technical Report CMS-NOTE-2011-005. ATL-PHYS-PUB-2011-11, CERN, Geneva, Aug, 2011.
- [138] G. Cowan, K. Cranmer, E. Gross, and O. Vitells, “Asymptotic formulae for likelihood-based tests of new physics”, *Eur. Phys. J. C* **71** (2011) 1554, doi:10.1140/epjc/s10052-011-1554-0, 10.1140/epjc/s10052-013-2501-z, arXiv:1007.1727. [Erratum: *Eur. Phys. J. C* 73,2501(2013)].

Appendix A

Used simulated data sets

Simulated standard model data sets

Table A.1.: All SM MC samples used in the analysis with their cross section. In the case k-factors are applied, they are given separately. $\{.. \}$ stands for RunIISummer16MiniAODv2-PUMoriond17_80X_mcRun2_asymptotic_2016_TracheIV_v6 in abbreviation. All samples are of the MINIAODSIM format.

process	data set	$\sigma \cdot k [\text{pb}]$
ttbar		
$t\bar{t} \rightarrow \ell^+ \nu b + \ell^- \bar{\nu} \bar{b}$	/TTTo2L2Nu_Tune*_ttHtranche3_13TeV-powheg-pythia8/{..}-v1	87.31
ttbarGamma		
$t\bar{t}\gamma$	/TTGamma_Dilept_Tune*_13TeV-amcatnlo-pythia8/{..}-v2	1.679
	/TTGamma_Hadronic_Tune*_13TeV-amcatnlo-pythia8/{..}-v2	3.482
	/TTGamma_SingleLeptFromT_Tune*_13TeV-amcatnlo-pythia8/{..}-v2	2.509
	/TTGamma_SingleLeptFromTbar_Tune*_13TeV-amcatnlo-pythia8/{..}-v2	2.509
DrellYan		
$Z/\gamma^* \rightarrow 2\ell$	/DYJetsToLL_M-50_TuneCUETP8M1_13TeV-amcatnloFXFX-pythia8/{..}_ext2-v1	5765.4
diboson		
$Z\gamma \rightarrow 2\ell\gamma$	/ZGTo2LG_Tune*_13TeV-amcatnloFXFX-pythia8/{..}_ext1-v1	117.864 · 1.06
	/ZGTo2LG_Tune*_13TeV-amcatnloFXFX-pythia8/{..}-v1	117.864 · 1.06
	/ZGTo2LG_PtG-130_Tune*_13TeV-amcatnloFXFX-pythia8/{..}-v1	0.1404 · 1.06
WZ	/WZTo3LNU_Tune*_13TeV-powheg-pythia8/{..}-v1	4.42965 · 1.109
	/WZTo3LNU_Tune*_13TeV-powheg-pythia8/{..}_ext1-v3	4.42965 · 1.109
$ZZ \rightarrow 2\ell 2\nu$	/ZZTo2L2Nu_13TeV-powheg_pythia8_ext1/{..}-v1	0.5644 · k
	/ZZTo2L2Nu_13TeV-powheg_pythia8/{..}-v1	0.5644 · k
$ZZ \rightarrow 4\ell$	/ZZTo4L_13TeV-powheg_pythia8/{..}-v1	1.212 · k
	/ZZTo4L_13TeV-powheg_pythia8_ext1/{..}-v1	1.212 · k
WW $\rightarrow 2\ell 2\nu$	/WWTo2L2Nu_13TeV-powheg/{..}-v1	12.178
$Wg \rightarrow \ell\nu g$	/WGToLNUg_Tune*_13TeV-amcatnloFXFX-pythia8/{..}_ext3-v1	489
W jets		
$W + jets$	/WJetsToLNU_Tune*_13TeV-amcatnloFXFX-pythia8/{..}_ext2-v2	61526.7
	/WJetsToLNU_Tune*_13TeV-amcatnloFXFX-pythia8/{..}-v1	61526.7
triboson		
WWg	/WWG_Tune*_13TeV-amcatnlo-pythia8/{..}_ext1-v1	0.2147
WZg	/WZG_Tune*_13TeV-amcatnlo-pythia8/{..}-v1	0.04123
single top		
$W^+ \rightarrow t\bar{b}$	/ST_s-channel_4f_leptonDecays_13TeV-amcatnlo-pythia8_*/{..}-v1	3.36
$q\bar{b} \rightarrow q'\bar{t}$	/ST_t-channel_antitop_4f_incl*Decays_13TeV-powhegV2-*pythia8_*/{..}-v1	80.95
$q\bar{b} \rightarrow q't$	/ST_t-channel_top_4f_incl*Decays_13TeV-powhegV2-*pythia8_*/{..}-v1	136.02
$\bar{b} \rightarrow W^+ \bar{t}$	/ST_tW_antitop_5f_NoFullyHadronicDecays_13TeV-powheg_*/{..}_ext1-v1	11.7
$b \rightarrow W^- t$	/ST_tW_top_5f_NoFullyHadronicDecays_13TeV-powheg_*/{..}_ext1-v1	11.7

Simulated SUSY data sets

Table A.2.: All SUSY MC samples used in the analysis. $\{..\}$ stands for 80X_mcRun2_asymptotic_2016 in abbreviation. All samples are of the MINIAODSIM format.

signal	data set
electroweak	
TChiNG	/SMS-TChiNG_BF50N50G_*/RunIISpring16MiniAODv2-PUSpring16Fast_{..}_miniAODv2_v0-v1
GMSB model	/GMSB_GravitinoLSP_N1decays_*/RunIISummer16MiniAODv2-PUSummer16Fast_{..}_TrancheIV_v6-v1
strong production	
T5bbbbZG	/SMS-T5bbbbZg_*/RunIISummer16MiniAODv2-PUSummer16Fast_{..}_TrancheIV_v6-v2

Appendix B	
	Used trigger paths

Table B.1.: Trigger paths used in the analysis for the signal event selection.

trigger path
dielectron trigger
HLT_Ele17_Ele12_CaloIdL_TrackIdL_IsoVL_DZ_v*
HLT_Ele23_Ele12_CaloIdL_TrackIdL_IsoVL_DZ_v*
HLT_DoubleEle33_CaloIdL_GsfTrkIdVL_v*
HLT_DoubleEle33_CaloIdL_GsfTrkIdVL_MW_v*
dimuon trigger
HLT_Mu17_TrkIsoVVL_Mu8_TrkIsoVVL_v*
HLT_Mu17_TrkIsoVVL_TkMu8_TrkIsoVVL_v*
HLT_Mu17_TrkIsoVVL_Mu8_TrkIsoVVL_DZ_v*
HLT_Mu17_TrkIsoVVL_TkMu8_TrkIsoVVL_DZ_v*
HLT_TkMu17_TrkIsoVVL_TkMu8_TrkIsoVVL_DZ_v*
HLT_Mu27_TkMu8_v*
HLT_Mu30_TkMu11_v*
electron-muon trigger
HLT_Mu17_TrkIsoVVL_Ele12_CaloIdL_TrackIdL_IsoVL_v*
HLT_Mu23_TrkIsoVVL_Ele8_CaloIdL_TrackIdL_IsoVL_v*
HLT_Mu23_TrkIsoVVL_Ele8_CaloIdL_TrackIdL_IsoVL_DZ_v*
HLT_Mu23_TrkIsoVVL_Ele12_CaloIdL_TrackIdL_IsoVL_v*
HLT_Mu23_TrkIsoVVL_Ele12_CaloIdL_TrackIdL_IsoVL_DZ_v*
HLT_Mu8_TrkIsoVVL_Ele17_CaloIdL_TrackIdL_IsoVL_v*
HLT_Mu8_TrkIsoVVL_Ele23_CaloIdL_TrackIdL_IsoVL_v*
HLT_Mu8_TrkIsoVVL_Ele23_CaloIdL_TrackIdL_IsoVL_DZ_v*
HLT_Mu12_TrkIsoVVL_Ele23_CaloIdL_TrackIdL_IsoVL_v*
HLT_Mu12_TrkIsoVVL_Ele23_CaloIdL_TrackIdL_IsoVL_DZ_v*
HLT_Mu30_Ele30_CaloIdL_GsfTrkIdVL_v*
HLT_Mu33_Ele33_CaloIdL_GsfTrkIdVL_v*

Table B.2.: Trigger paths used in the analysis for the trigger efficiency measurements.

trigger path
HT trigger
HLT_PFHT200_v*
HLT_PFHT250_v*
HLT_PFHT300_v*
HLT_PFHT350_v*
HLT_PFHT400_v*
HLT_PFHT475_v*
HLT_PFHT600_v*
HLT_PFHT650_v*
HLT_PFHT800_v*
MET trigger
HLT_PFMET110_PFMHT110_IDTight_v*
HLT_PFMET120_PFMHT120_IDTight_v*
HLT_PFMET170_NoiseCleaned_v *
HLT_PFMET170_HBHECleaned_v*
HLT_PFMET170_JetIdCleaned_v*
HLT_PFMET170_NotCleaned_v*
HLT_PFMET300_v*
HLT_PFMET400_v*
HLT_PFMET500_v*
HLT_PFMET600_v*